Diploma Thesis

The Design of a Phase Fluorometer For Oxygen Sensors

Christoph Larndorfer

Institut für Analytische Chemie und Lebensmittelchemie
Technische Universität Graz

Evaluator: Ao.Univ.-Prof. Dipl.-Ing. Dr.techn. Hermann Scharfetter
Supervisor: Univ.-Prof. Dipl.-Chem. Dr.rer.nat. Ingo Klimant

Graz, June 2011

Abstract

This work describes the design of a phase fluorometer for the measurement of oxygen levels in liquids and gases in combination with a specific optic sensor. Oxygen is able to quench the luminescence in the sensor which can be measured with the phase fluorometer using LED excitation and standard photodiodes. The sensor is illuminated with modulated light and the luminescence lifetime is then determined from the phase shift of the emitted light with respect to the excitation.

A new model presented in this work describes the phase shift of the emitted light and also considers saturation effects of luminescence and limitations in quenching with oxygen in condition with high excitation light intensities. Simulation results of the new model were validated with a measurement series of different microsensors exposed to varying light intensities and an affect of both the phase and the lifetime of the luminescence was realised.

Many new concepts are integrated in the device to increase performance and usability and at the same time flaws of established designs are eliminated to a large extent. The electronic circuits are developed with standard parts and optimised to show small crosstalk, low noise levels, low power consumption and minimise the temperature dependency of the phase measurements with an additional reference LED. The photodiode and LEDs of the phase fluorometer are aligned perpendicular to each other and a dichroic mirror splits emission light from stray light to significantely suppress optic crosstalk and ambient light interference. All optic and electronic components are integrated in a miniaturised and consistent design, which makes a further integration of many of these fluorometers in a multi-channel device possible.

The performance of the phase fluorometer was verified under various ambient light and temperature conditions and the tests show that phase shifts can be measured with a resolution of $\approx {}^{1}/_{100}\,^{\circ}$ and a drift of $< {}^{1}/_{10}\,^{\circ}$ over a temperature range of 5 °C to 60 °C. The results confirm the implemented concepts and give insight for the development of new improvements.

Kurzfassung

Diese Arbeit umfasst die Entwicklung und den Aufbau eines Phasenfluorometers für die Messung des Sauerstoffgehalts von Flüssigkeiten und Gasen mittels eines speziellen optischen Sensors. Sauerstoff ist imstande die Lumineszenz des Sensors zu löschen, welche mit Hilfe des Phasenfluorometers über eine LED Anregung und Photodioden gemessen werden kann. Der Sensor wird mit moduliertem Licht beleuchtet und die Lebenszeit der Lumineszenz kann über die Phasenverschiebung zwischen emittiertem und angeregtem Licht ermittelt werden.

Ein in dieser Arbeit erstelltes Modell beschreibt die Phasenverschiebung des emittierten Lichtes, wobei auch Sättigungseffekte der Lumineszenz und Einschränkungen in der Löschung mit Sauerstoff in Bedingungen mit hohen Lichtintensitäten berücksichtigt werden. Simulationsergebnisse des neuen Modells wurden mittels einer Messreihe verschiedener Mikrosensoren bei unterschiedlichen Lichtintensitäten überprüft und Auswirkungen auf die Phasenverschiebung sowie auf die Lebenszeit konnten gezeigt werden.

Einige neue Konzepte wurden in das Gerät miteinbezogen um die Benutzerfreundlichkeit und Leistungsfähigkeit zu steigern und gleichzeitig wurden einige Schwächen von bekannten Konzepten eliminiert. Die Schaltkreise wurden mit serienmäßigen Komponenten entwickelt und auf geringes Übersprechen, Rauschen und geringe Leistungsaufnahme optimiert. Die Temperaturabhängigkeit der Phasenmessung wurde mit einer zusätzlichen Referenz-LED minimiert. Die Photodioden und LEDs des Phasenfluorometers wurden rechtwinkelig zueinander ausgerichtet und ein dichroitischer Spiegel teilt das emittierte Licht von Streulicht und unterdrückt optisches Übersprechen und Beeinträchtigungen aufgrund von Umgebungslicht erheblich. Alle optischen und elektronischen Bauteile wurden in einer miniaturisierten und durchgängigen Bauweise integriert, womit mehrerer dieser Fluorometer in ein Multikanal-Gerät kombiniert werden können.

Das Verhalten dieses Phasenfluorometers wurde unter verschiedenen Umgebungslicht- und Temperaturbedingungen überprüft und es zeigte sich, dass Phasenverschiebungen mit einer Auflösung von $\approx {}^{1}/_{100}\,^{\circ}$ gemessen werden können mit einer Abweichung von $< {}^{1}/_{10}\,^{\circ}$ in einem Temperaturbereich von 5 °C bis 60 °C. Die Messergebnisse bestätigen die entwickelten Konzepte und lassen auch Schlüsse auf mögliche weitere Verbesserungen zu.

Statutory Declaration

I declare that I have authored this thesis independently, that I have not used other than the declared sources / resources, and that I have explicitly marked all material which has been quoted either literally or by content from the used sources.

Place	Date	Signature

Acknowledgements

This thesis was written at the Institute for Analytical Chemistry and Food Chemistry at the Graz University of Technology from August 2010 until June 2011. Many thanks to my colleagues from the workgroup of Chemo- and Biosensors, who welcomed me very nicely, supported my work with much engagement and enthusiasm and made working amongst them simply fun. Special thanks must go to my supervisor and head of the institute Ingo Klimant, who always came up with excellent ideas and large expertise that pushed my work and thinking into new directions and towards better solutions. During this last year I got very nicely introduced into the field of analytical chemistry and I always enjoyed to have discussions with and get small lectures from my colleagues - from low-level chemistry to advanced photo-luminescence and even tips for cooking and life in general!

The whole design and development process during this thesis was enormously accelerated with the extraordinary open-minded and friendly help of Dr. Roland Thar, chief executive of the company Pyro Science. This made the start of my thesis much faster and interesting, as Roland shared a lot of knowledge about phase fluorometric measurement concepts with me.

I also want to thank my family, especially my parents for making my long-lasting education possible and my siblings, which always influenced me a lot when I had to take serious decisions. Without the backing from many of my friends this work may not have taken such a positive outcome and without the help of some special ones this work here may never have started. Eventually a big thank you to my girlfriend Emily Nix, who motivated me to look closer at things and allowed me to discover that an engineer can make a difference.

Graz, June 2011 Christoph Larndorfer

List of Nomenclature

$A(\lambda)$	absorbance
B	bandwidth (Hz)
E_{em}	emission light intensity (W/m^2)
E_{ex}	excitation light intensity (W/m^2)
f_s	sampling frequency (Hz)
f_c	conversion frequency (Hz)
$H(j\omega)$	transfer function of a system
h	Planck constant ($J \cdot s$)
$I(\lambda)$	light intensity (W/m^2)
I_d	dark current generated in a photodiode (A)
I_{ph}	photo-current generated in a photodiode (A)
i_n	noise current density ($A/\sqrt{Hz}$)
K_D	quenching constant for dynamic quenching (hPa^{-1})
K_{SV}	Stern-Volmer constant for static quenching (hPa^{-1})
k	Boltzmann constant ($J \cdot K^{-1}$)
k_{nr}^X	non-radiative relaxation rate from the excited state X (s^{-1})
k_r^X	radiative relaxation rate from the excited state X (s^{-1})
$[L^X]$	concentration of luminophores in the electronic state X (M)
$m(\omega)$	modulation ratio between input and output sine wave amplitudes
N	number of ADC or DAC sampling points
N_a	Avogadro constant (mol^{-1})
P_n	noise power (W)
P_s	signal power (W)
pO_2	partial pressure of oxygen (hPa)
$[Q^X]$	concentration of quenchers in the electronic state X (M)
q_e	elementary charge (C)
T	temperature (K)
$T(\lambda)$	transmittance

u_n	noise voltage density ($\mathrm{V}/\sqrt{\mathrm{Hz}}$)
$\varepsilon(\lambda)$	molar absorption coefficient ($\mathrm{l} \cdot \mathrm{M}^{-1} \cdot \mathrm{cm}^{-1}$)
λ	wavelength of light (nm)
μ_a	absorption coefficient (cm-1)
ν	light frequency (Hz)
ρ_{ex}	photon density of the excitation light ($\mathrm{s}^{-1} \cdot \mathrm{m}^{-2}$)
$\sigma(\lambda)$	absorption cross-section (m^2)
σ_{ex}	absorption cross-section of a luminophore for the excitation light (m^2)
σ_j	standard deviation of jitter (s)
σ_n	standard deviation of the noise amplitude (V)
σ_ϕ	standard deviation of the noise phase (rad)
τ	decay time of the luminescent light with quencher (s)
τ_0	decay time of the luminescent light without quencher (s)
Φ	quantum yield of the luminescence with quencher
Φ_0	quantum yield of the luminescence without quencher
$\phi(\omega)$	phase shift between input and output sine wave amplitudes (°)
ω	angular frequency (rad/s)

List of Abbreviations

AAF	anti-aliasing filter
ADC	analog to digital converter
AGC	automatic gain control
BJT	bipolar junction transistor
DAC	digital to analog converter
DFT	discrete Fourier transformation
DSP	digital signal processor
EHP	electron hole pair
ENOB	effective number of bits
ESD	electrostatic discharge
FD	frequency domain
GBW	gain bandwidth
IC	internal conversion
ISC	intersystem crossing
LED	light emitting diode
LPF	low-pass filter
LTI	linear time-invariant
MCU	microcontroller unit
MOSFET	metal-oxide-semiconductor field-effect transistor
OPA	operational amplifier
PCB	printed circuit board
PD	photodiode
PdTPTBPF	Palladium (II) (5,10,15,20)-tetra(4-fluorophenyl)tetrabenzoporphyrin
PtTPTBPF	Platinum (II) (5,10,15,20)-tetra(4-fluorophenyl)tetrabenzoporphyrin
PWM	pulse width modulation
SNR	signal to noise ratio
SINAD	signal to noise and distortion ratio
SQNR	signal to quantization noise ratio

TD	time domain
TIA	transimpedance amplifier
XT	crosstalk

Contents

1. Introduction

The detection and quantization of oxygen is of significant interest in analytical, environmental and biomedical applications. Dissolved oxygen levels in water indicate the level of quality which is important for waste-water management. Other important applications can be found in many biochemical processes, e.g. monitoring of metabolic processes which consume oxygen, in blood gas analysis for medical purposes and in biosensors where enzymatic reactions consume or release oxygen (e.g. glucose sensor). The most commonly used sensor for these applications is the Clark-type oxygen electrode, however, it has several practical drawbacks and limitations, which triggers research for other techniques for oxygen sensing.

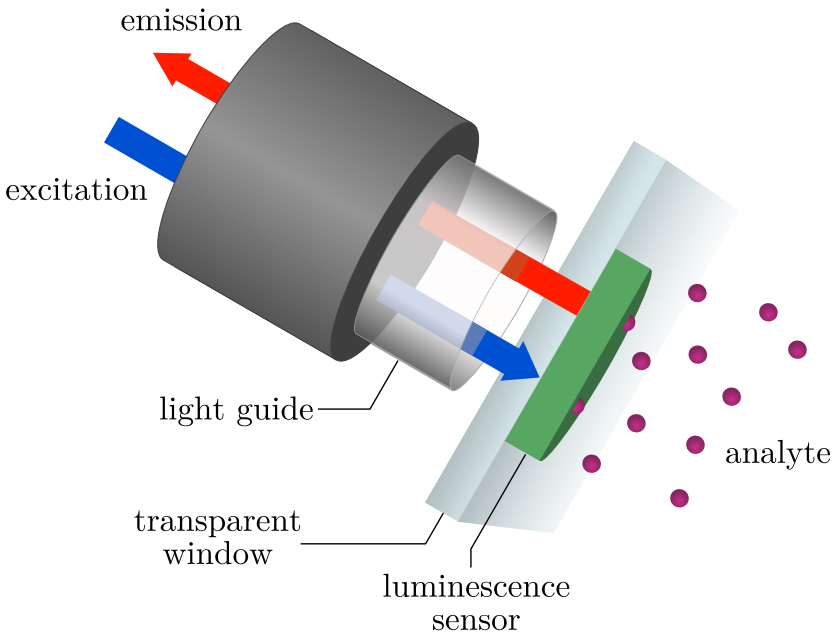

Figure 1.1.: Principle scheme of an optode with a luminescence sensor.

The field of optical sensors based on luminescence is an excitingly growing topic in research [1, p. 7]. Many electrochemical sensors, such as ion-selective, pH, CO_2 and O_2 electrodes, nowadays have an optical based sensor (for short optode) as counterpart, which measures a specific substance usually with the aid of a chemical transducer. The Clark-electrode for sensing oxygen has to compete more and more with newly developed luminescence sensors [2, 3], where oxygen has the ability to act as a dynamic luminescence quencher. The advantages of the optical oxygen sensors are that they do not consume oxygen and thus are independent of the incident flow [2]. They are not easily poisoned and have a fast response time [4]. Generally

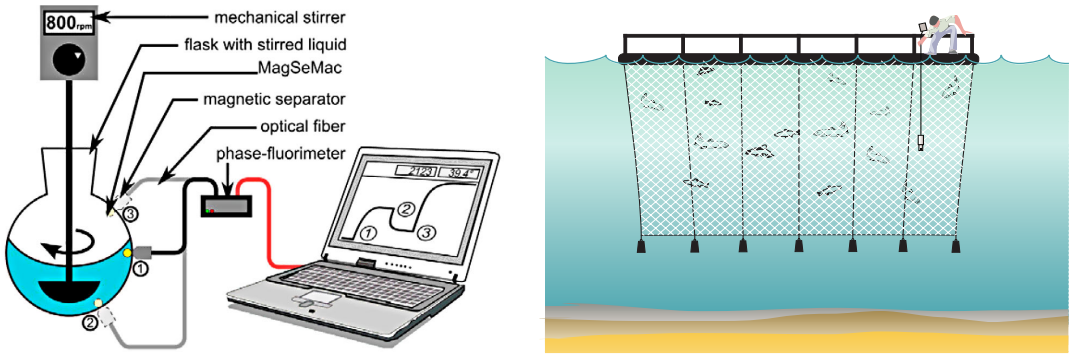

(a) (b)

Figure 1.2.: Some example applications for optodes: A magnetic sphere inside a shake flask (a) coated with luminophores is continuously analysed with a phase fluorometer [7]. Oxygen measurements under harsh conditions (b) in low depths in the sea for industrial and environmental purposes (from *Aanderaa Data Instruments*).

optodes do not need to be in direct contact with the sample and are therefore also suitable for non-invasive measurements.

The fabrication of the optical sensors is straight forward and they can be used as microsensors [5], in (nano-)particles [6] and coated on polymer films or magnetic spheres [7]. The introduction of luminophores which excitation spectrum almost perfectly matches with standard LED emission spectra [8] promotes the development of low-cost, low-power, miniaturised and highly versatile measurement devices [9, 10, 11, 12, 13] which either measure the intensity or lifetime of the luminophore. Phase fluorometers are capable of measuring lifetimes in a relatively simple manner whilst the development of small and affordable high-performance digital signal processors allowed the design of integrated devices to measure oxygen levels optically (e.g. Firesting O_2 from *Pyro Science*[1], Fibox 3 from *PreSens*[2]).

1.1. Motivation

Luminescence oxygen sensors offer the user a continuous and virtually non-invasive monitoring concept applicable in many different systems, however, the commonly used measurement devices for decoding the luminescence information are often bulky, difficult to operate and deliver results which have to be interpreted from experts to deduce the oxygen concentration at the sensor location. These devices offer experts an adjustable functionality for reading out many different luminophores with different characteristics, however, the setup and operation is not very user friendly.

This means, although a luminescence oxygen sensor outstands usual sensors (e.g. Clark-electrode) in many features it is not used in practice because of the current lack of usability.

[1] Pyro Science e.K., Hubertusstr. 35, 52064 Aachen, Germany, http://www.pyro-science.com/
[2] PreSens - Precision Sensing GmbH, Josef-Engert-Str. 11, 93053 Regensburg, Germany, http://www.presens.de/

Further research in luminescence sensors and measurement methods can lead this technology to a stage where it becomes as easy and reliable to use as an electronic thermometer or pH-probe and opens the way for many other applications.

1.2. Objective

This work focuses on the development of a transducer which decodes the luminescence information as robustly and exactly as possible by simultaneously reducing size and power consumption radically. This means that phase errors due to temperature variations, electronic coupling and the phase noise should be kept as small as possible. Furthermore the whole measurement device is fitted to one luminescence oxygen sensor, therefore the oxygen level can be calculated internally and presented in a user-friendly way (e.g. on a computer via USB). As in many applications a parallel measurement of many different oxygen levels is needed (e.g. multiple respirometric wells in a lab) this work also investigates a simple and scalable integration of several channels into one measurement device.

However, the finished device should also satisfy experts and allow them to read out less decoded information (raw data) and also change measurement settings to adjust for slightly different sensors. Thus the design was kept as flexible as possible to better be ready for future challenges in optical sensing and allow people to utilise this device for ongoing research.

1.2.1. Requirements and specifications

This transducer should be especially designed for one specific luminophore, developed at the Institute for Analytical Chemistry and Food Chemistry (ACFC) at the Graz University of Technology, which is specified as listed below:

Phosphorescent sensor specifications

- Extremely efficient excitation in the blue and red parts of the spectrum (fig. 1.3(a)). The molar absorption coefficients ε exceed $200,000\,\mathrm{l}\cdot\mathrm{M}^{-1}\cdot\mathrm{cm}^{-1}$ for the Soret band (blue excitation) and $130,000\,\mathrm{l}\cdot\mathrm{M}^{-1}\cdot\mathrm{cm}^{-1}$ for the Q-band (red excitation).
- Viable emission in the NIR (peaking at 760 nm, fig. 1.3(b)). The emission quantum yield in the absence of oxygen is estimated to be $\Phi_0 = 60\,\%$.
- The phosphorescence decay time τ_0 in the absence of oxygen of $55\,\mu$s enables optimal sensitivity in optical oxygen sensors.
- Very low temperature quenching of luminescence results in lower cross-sensitivity to temperature of the oxygen sensors.
- Excellent solubility in solvents and polymers.
- Excellent photostability.

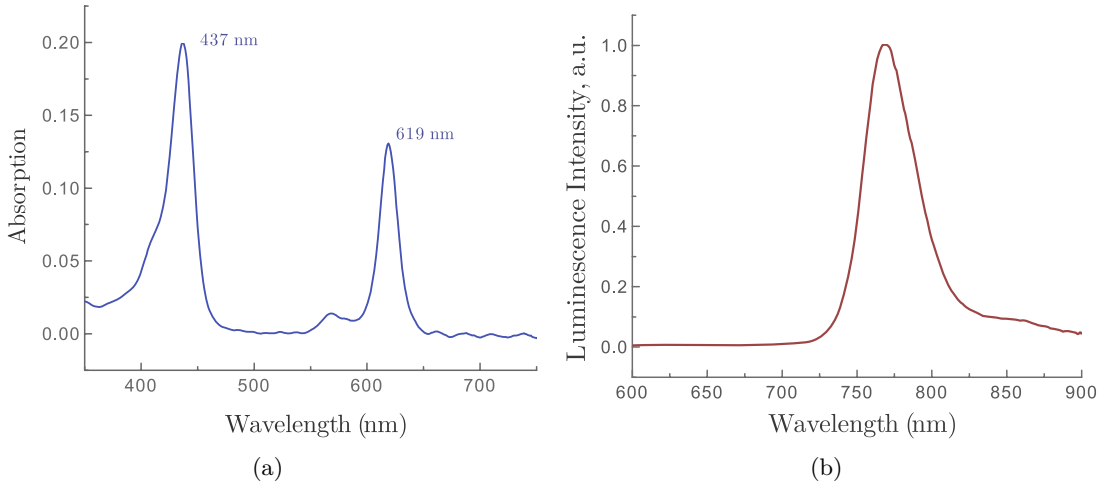

Figure 1.3.: Absorption (a) and emission (b) spectrum of the luminophore used for optical measurements of oxygen.

Phase fluorometer requirements

The completed prototype should perform best with the above described sensor, but also include the possibility to probe similar luminophores. It should be possible to flexibly adopt the device to new and different measurement methods, including the change of optical filters, numbers and location of channels and there should be still a possibility for extensions.

The prototype performance was specified to stay within the following limits:

- **Phase resolution:** $< 5/100\,°$, illuminating the sensor for 500ms
- **Phase noise:** $< 5/100\,°$, illuminating the sensor for 100ms
- **Signal background level:** $< 1\,\%$ of the emission signal amplitude
- **Sensor illumination time:** variable from 10 ms to 1s
- **Frequency range:** adjustable from 100 Hz to 5kHz
- **Power consumption:** $< 500\,\mathrm{mW}$ at $5\,\mathrm{V}$
- **Dimensions for four channels:** at max. $100 \times 100 \times 35\,\mathrm{mm}$

1.3. Thesis outline

This work therefore focuses on a better understanding of the used principles and technologies and how they act together to form a complete and reliable phase fluorometer - a measurement device for phase shifts of the sinusoid emission light from a luminophore. This includes a proper investigation of the used opto-electronic circuits / components and how they can be optimised to increase the measurement performance, reduce and better understand sources for phase errors whilst still maintaining a huge flexibility.

In 3.1 many of the used principles in a phase fluorometer are addressed and this work focuses on possible improvements for an optimised design or confirmes established concepts. Simultaneously the possible influence of crosstalk and noise on the phase is described in 3.2 in order to summarise and present formulas and theories scattered in literature. The downscale of the device outline and a reduction of power requirements was always kept in mind during the development process.

Additionally this work puts phosphorescent sensors themselves in the focus and tries to describe the resulting phase shift of the emission light, which solely depends on the decay time of the phosphorescence, in a wider model. In 3.3 this model is explained and it also shows the limitations of the usually used approach to describe the decay time of phosphorescence.

1.4. Precursor model

The development process of such a device with the above specifications started with the design of a precursor model, which should represent the state-of-the-art technology and thus was the initial point for adaptations and improvements to provide a more appropriate design for the requirements of the Institute of Analytical Chemistry and Food Chemistry. This could be achieved by closely working together with the company *Pyro Science*, which works in the field of phase fluorometric device development.

In fig 1.4 one can see a typical setup for this precursor: Multiple wells, either coated with the luminescent sensor or containing a magnetic sensor sphere, are analysed. The vessels can be easily aligned on the device and the phase shift of each channel can be transmitted to a PC via an USB-connection.

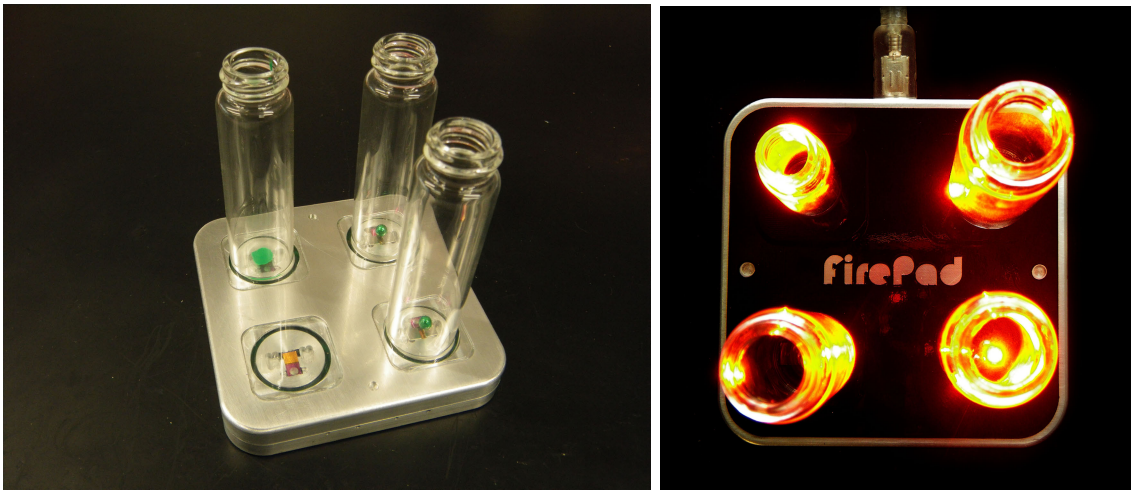

(a) (b)

Figure 1.4.: Typical setup of a phase fluorometric device in a laboratory. The vessels are coated with or contain the luminescence sensor inside. During a measurement the device is connected to a PC which receives the sampled data.

1.4.1. Design overview

The precursor model was designed with four phase fluorometric measurement channels. The signals of the four channels were amplified centrally, filtered and converted to digital signals and a central MCU was calculating the phase shifts for every channel as outlined in fig. 1.5. The digital parts for the USB-communication are on the bottom side of the PCB.

An established and easy architecture for the optics is a flat one (e.g. used in the Oxygen Sensor 4500 by $AADI^3$), thus all the opto-electronic elements are positioned at the same level. The photodiode, excitement and reference led were positioned right next to each other [4] and above these parts a small optic block is fixed (see fig. 1.6), which includes light tunnels, excitation and emission filters. The filters are long and short-pass filters and were glued into the block.

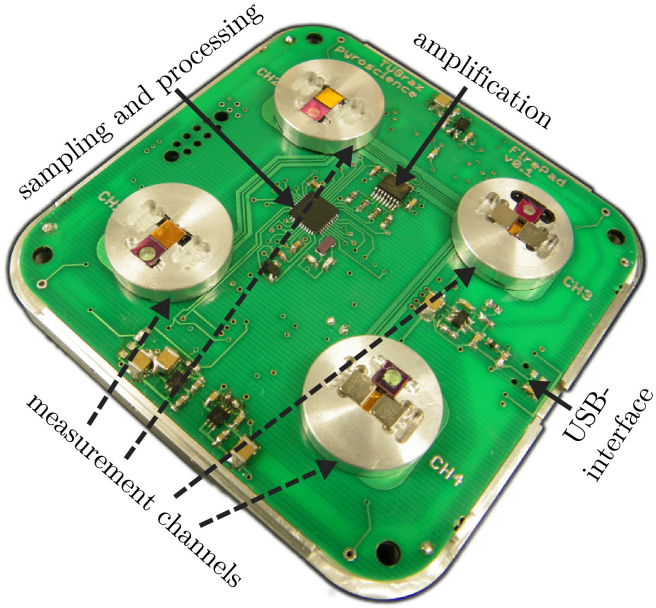

Figure 1.5.: Overview of the precursor layout.

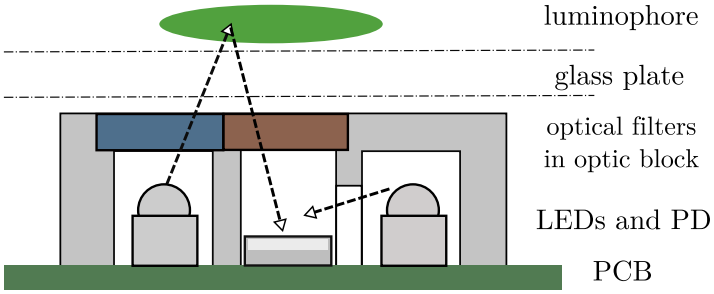

Figure 1.6.: Outline of the optic block with the light paths for main and reference LED.

[3] AADI, P.O.Box 34 Slåtthaug, N-5851 Bergen, Norway, http://www.aadi.no/

2. Background

The development of a measurement device requires the electric design engineer to understand a wide area of subjects as the physical quantity to measure - in this case the amount of oxygen - needs to be translated into an electrical signal first. Therefore requires also know-how in chemistry and optics. The sections in this chapter dealing with luminescence (2.1, 2.2) are mainly based on the books [14, 15, 16] whereas sections about electronics (2.3, 2.4) are based on [17, 18] and further citations are referenced respectively. The following introductory content is based upon the book [16].

The composition of a (bio)chemical sensor can be seen in fig. 2.1. The last stage is the electrical part, where the signal gets conditioned for further processing. The transducer converts the change of a physical or chemical property (e.g. temperature, mass, pressure, pH, luminescence) into an electrical signal (voltage, current). In (bio)chemical sensors often the analyte itself does not provide such a property, but the interaction with a receptor can lead to a change of a physical or chemical property of either the receptor, the analyte or both. If the receptor is not selective enough for the analyte or needs to be in a well specified compartment, filters are used to ensure a specific exchange with the outside. The performance of the transducer and receptor heavily affects the electrical measurement chain and has to be well specified to allow an optimal electric design.

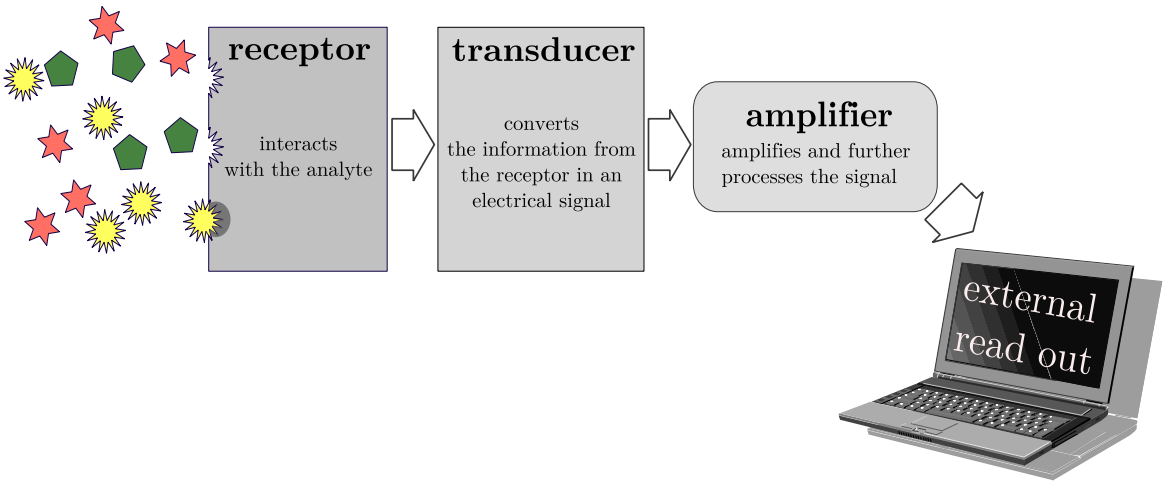

Figure 2.1.: General composition of a (bio)chemical sensor.

In this thesis the first three components of the sensor are:

- **Analyte:** Oxygen (i.e. oxygen partial pressure)
- **Receptor:** With oxygen quenchable luminophore immmobilised in a polymer matrix
- **Transducer:** Optical filters, photodetector and a light source in combination

The more insight one gathers about the transducer and receptor, the better one can estimate how design changes may increase or decrease the overall performance of the measurement chain. This is the motivation to pay attention to the following sections including the physical principles of luminescence, which in this work is the feature of interest.

2.1. Luminescence

Luminescence is the emission of light (ultraviolet, visible or infrared) from an electronically excited molecule. According to the mode of excitation, luminescence is classified in different types (see tab. 2.1). This thesis is solely concerned with photoluminescence, where the mode of excitation is absorption of photons. The electronically excited luminophore has then different possibilities for the de-excitation, which classifies the phenomenon either as fluorescence, delayed fluorescence or phosphorescence.

Table 2.1.: The various types of luminescence [14]

.

Phenomenon	**Mode of excitation**
Photoluminescence (fluorescence, phosphorescence, delayed fluorescence)	Absorption of light (photons)
Radioluminescence	Ionizing radiation (X-rays, α, β, γ)
Cathodoluminescence	Cathode rays (electron beams)
Electroluminescence	Electric field
Thermoluminescence	Heating after prior storage of energy (e.g. radioactive irradiation)
Chemiluminescence	Chemical process (e.g. oxidation)
Bioluminescence	Biochemical process
Triboluminescence	Frictional and electrostatic forces
Sonoluminescence	Ultrasounds

The next paragraph gives the reader a short introduction on how light in general can interact with matter and absorption is one of the possibilities. In special cases the photon energy is converted into light again, which is then called photoluminescence, but in most molecules the photon energy is converted into other forms (e.g. heat).

2.1.1. Light matter interactions

Light, which can be seen as either an electro-magnetic wave or a stream of photons with the photon energy $E = h\nu$, can interact with matter in many ways. Fig. 2.2 outlines possible interactions between light and matter.

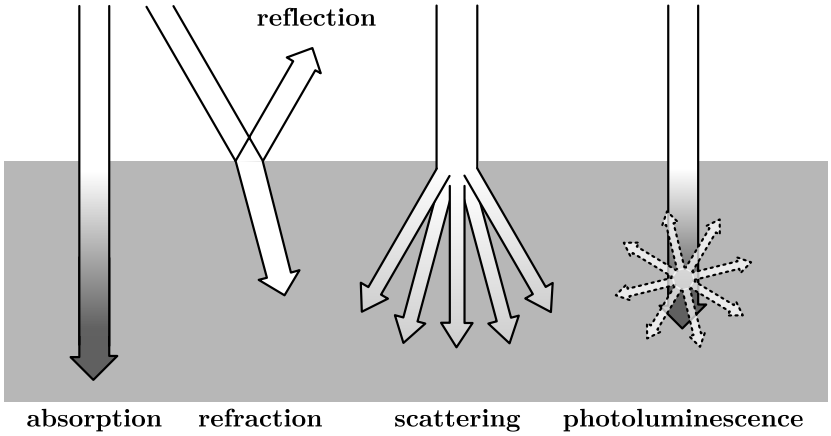

Figure 2.2.: Possible interactions of light with matter: Absorption, reflection and refraction, scattering and photoluminescence

Absorption

Photons can interact with either *molecules* (vibrational and rotational transitions), *atoms* or *electrons* - (electronic transitions) by transferring their energy to them. Therefore, the absorption (and emission) of photons changes the energy level of a molecule / atom and only specific energies can promote a transition from a so called *ground state* to excited states.

Reflection & refraction

Reflection and refraction are elastic interactions and can be explained by one of the most important properties of classical wave optics - the *refractive index*: $\eta = c/v$. It is defined as a fraction of the phase velocity of light in vacuum and in matter. The refractive index is a function of the frequency of light $\eta = \eta(\nu)$ and this effect is called *dispersion* and is important for light guides (e.g. fibres).

When two materials with a difference in refractive index form a boundary layer and light passes through it, one can see *reflection* and *refraction*. The ratio of light which is reflected and transmitted is determined by Fresnel's coefficients.

Scattering

Scattering incorporates all processes which in some way deflect photons from their original trajectory. On the one hand in elastic scattering (e.g. Rayleigh and Mie scattering) the photon

energy is preserved and it can be defined as the deflection of photons from their trajectory due to microscopic variations of the refractive index. On the other hand in inelastic scattering (e.g. Raman and Compton scattering) the photon energy changes in addition to the deflection. Contrary to photoluminescence the scattered light wavelength greatly depends on the incident light wavelength.

Photoluminescence

After photon absorption the excited molecule returns to the ground state by releasing the absorbed energy either in non-radiative processes (e.g. generation of heat) or radiative processes, which can be fluorescence and phosphorescence. The resulting photons have a different energy and trajectory compared to the incident light.

2.1.2. Absorption of UV and visible light

It is very important to understand the principles of UV and visible light absorption, as in this case this method is used to get luminophores into the excited state. A photon of appropriate energy promotes an electron of a molecule into a molecular orbital of higher energy (electronic transition). Photons in the UV and visible light region most likely promote an electron in a molecular π orbital to perform a transition to an antibonding orbital denoted π^* ($\pi \rightarrow \pi^*$ transition), as these orbitals have a rather low energy difference. Of course, other transitions, such as $n \rightarrow \pi^*$ (non-bonding electron to antibonding transition), with smaller or bigger energy differences are also possible. In fig. 2.3 possible transitions and their energy differences are shown.

Such a promotion in principle does not change the spin of the electron, thus the total spin quantum number ($S = \sum_i s_i$) remains zero and the multiplicity ($M = 2S + 1$) is one (singlet state) for both the excited and the ground states. Radicals (molecules or atoms with unpaired

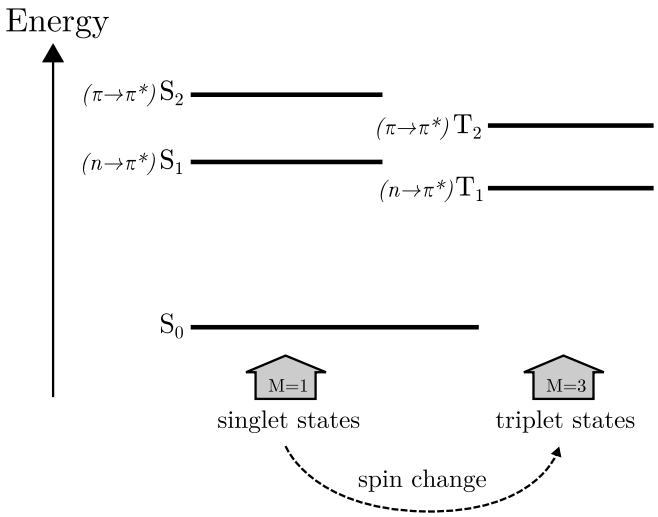

Figure 2.3.: An example of energy levels with singlet and triplet states

electrons) are not considered here. As described later, a molecule can also have electrons with the same spin number in the excited state, thus the multiplicity is three and the molecule is in a triplet state (fig. 2.3).

Selection rules: Transitions are most likely to occur between states of same multiplicity (singlet-singlet or triplet-triplet), however, there is a very small probability of a singlet-triplet transition and vice-versa. Singlet-triplet transitions can be actively promoted due to spin-orbit coupling, which is then called *intersystem-crossing* and favoured by the presence of a heavy atom.

Beer-Lambert Law

This law explains the reduction of light intensity (irradiance) due to absorption in a medium,

$$I_\lambda = I_\lambda^0 10^{-\varepsilon(\lambda)cl} \tag{2.1}$$

where I_λ^0 and I_λ are the light intensities of the beams entering and leaving the absorbing medium, ε is the *molar (decadic) absorption coefficient*, l is the thickness of the medium and c is the concentration of the absorbing molecules. The absorption coefficient depends greatly on the wavelength of the incident light and is molecule specific. Experimentally, the absorbance $A(\lambda)$ or transmittance $T(\lambda)$ can be easily calculated as they are defined as:

$$A(\lambda) = -\log(T(\lambda)) = \log \frac{I_\lambda^0}{I_\lambda} \tag{2.2}$$

In many cases, the absorbance of a sample follows the *Beer-Lambert Law* (eqn. 2.1). This law can be derived by looking at the medium at a molecular scale where then the efficiency with which a molecule captures a photon is expressed with the absorption cross section $\sigma(\lambda)$ (see fig. 2.4). The expected efficiency $\mathrm{E}(\eta_{abs})$ to absorb photons with the wavelength λ in a thin slab can then be expressed as the absorption cross-section multiplied by the number

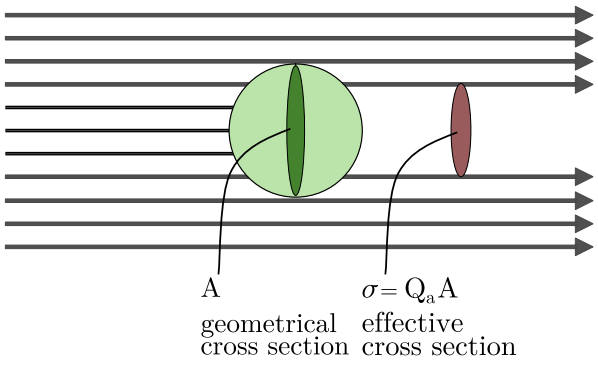

Figure 2.4.: Definition of the absorption cross-section and the probability of photon absorption

of molecules per area. The expected efficiency $\mathrm{E}(\eta_{ex})$ of photons exciting a molecule can be expressed similarly:

$$\mathrm{E}(\eta_{abs}) = \sigma(\lambda) \underbrace{N_a c dl}_{\mathrm{molecules/m^2}} = -\frac{dI_\lambda}{I_\lambda} \tag{2.3}$$

$$\mathrm{E}(\eta_{ex}) = \sigma(\lambda) \underbrace{\frac{I_\lambda}{h\nu} dt}_{\mathrm{photons/m^2}} \tag{2.4}$$

If the concentration of molecules is assumed to be constant over the thickness of the medium l, the integration of eqn. 2.3 yields,

$$\ln \frac{I_\lambda^0}{I_\lambda} = N_a \sigma(\lambda) c l \quad \text{or} \quad \log \frac{I_\lambda^0}{I} = \frac{1}{2.303} N_a \sigma c l$$

which is formally identical to the Beer-Lambert law in eqn. 2.1 with $\varepsilon = N_a\sigma/2.303$. Eqn. 2.4 shows that the expected number of absorption events is directly proportional to the absorption coefficient, the layer thickness l and the concentration c.

Franck-Condon principle

The Franck-Condon principle is based on the observation that motions of electrons are much faster than those of the nuclei, therefore if an electronic transition occurs (e.g. $\pi \rightarrow \pi^*$) the nuclear configuration stays unchanged, however, after excitation the nuclei begin to vibrate at an energy corresponding to the intersection (see fig.2.5). Additionally to this favoured *vertical transition*, vibronic transitions to other vibrational levels are also possible and cause the broadening of the absorption spectrum.

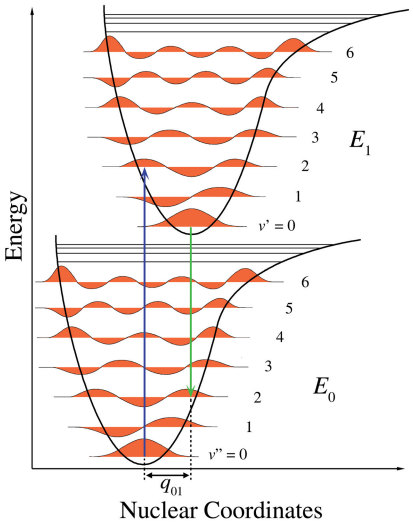

Figure 2.5.: A potential energy diagram of a molecule configuration with excited state, ground state and the vertical transition (Franck-Condon principle). The potential wells are shown favoring transitions between vibrational state 0 and 2.

2.1.3. Intramolecular deactivation processes

The intramolecular deactivation processes and the preceding absorption can be best visualised by using a Jablonski-Diagram (see fig. 2.6). Absorption takes places according to the Franck-Condon principle from the lowest vibrational energy level of S_0 to excited states $S_1, S_2, \ldots$, because due to the Boltzmann-distribution very few molecules are at higher vibrational levels at room temperature. Once excited several intramolecular de-excitation pathways are possible for the molecule to return to the ground state, which are examined in the following sections.

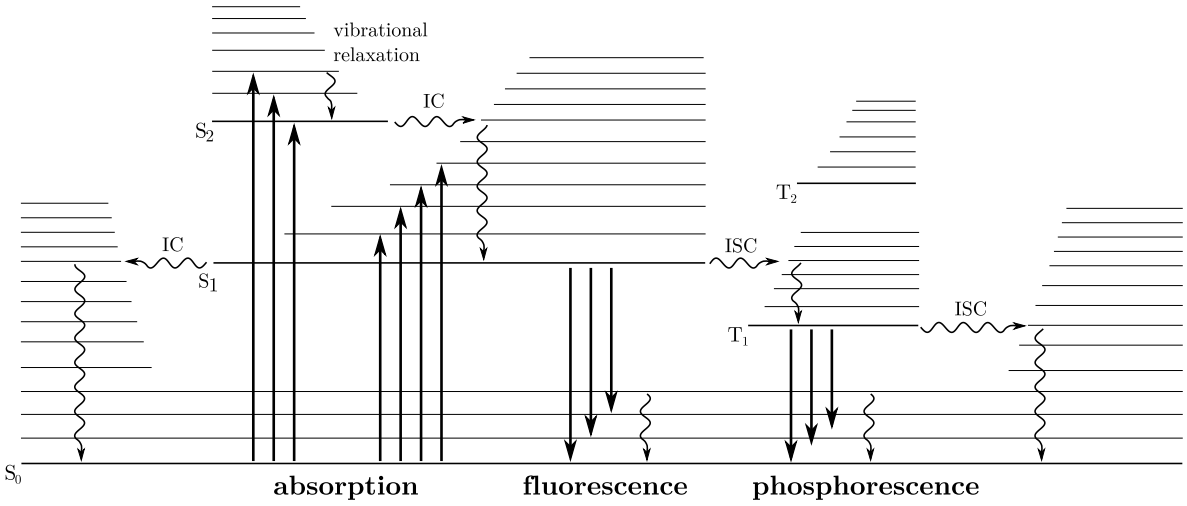

Figure 2.6.: Jablonski diagram of the different de-excitation pathways of a molecule. Thick lines represent electronic energy levels, thin ones vibrational energy levels. Non-labelled arrows represent vibrational relaxations.

Internal conversion

Internal conversion (IC) is a non-radiative transition from an electronic excited state to a lower one with same multiplicity. The conversion time is in the range of $10^{-11} - 10^{-9}$ s and gets less efficient with higher energy gaps between the states. Before this transition can happen the molecule has to get to the lowest vibrational energy level of the excited state through vibrational relaxation.

Fluorescence

Fluorescence is the emission of photons from $S_1 \rightarrow S_0$ and the characteristic times are in the range of $10^{-10} - 10^{-7}$ s and this process competes with internal conversion. Again the emission follows the Franck-Condon principle and therefore the emission spectrum looks like a mirrored version of the absorption spectrum (as the vibrational energy levels of S_0 and S_1 are similar) and are always shifted to a higher wavelength (Stoke's shift).

Intersystem crossing

Another pathway to leave the energy state S_1 is via intersystem crossing (ISC), which describes the normally forbidden transition from one excited state to another excited state with different multiplicity. This can happen and actively exploited due to spin-orbit coupling and gets more efficient with the presence of heavy atoms (such as Pt or Pd). As normally the conversion times are of much higher order than IC or fluorescence ISC does not occur, but some molecule configurations can have conversion times that compete with fluorescence and IC, thus the following processes such as phosphorescence and delayed fluorescence become possible.

Phosphorescence

In many substances phosphorescence - the radiative transition $T_1 \rightarrow S_0$ - cannot be observed as the non-radiative process is much more likely, again thanks to spin-orbit coupling. However in some cases it can be observed and the lifetime of this transition can reach the order of minutes. This emission is almost always a spontaneous process, however under certain conditions (population inversion) stimulated emission can be dominant (e.g. LASER). The wavelength of the emitted light is even longer than that of fluorescent light, because the T_1 state has a lower energy than the S_1 state.

Delayed fluorescence

Delayed fluorescence can happen because of thermal activation of the molecule with ISC or by a collision of two molecules in the T_1 state. Of course, the former is much more likely at higher temperatures and when the energy for T_1 is close to S_1 and the latter occurs only in very concentrated solutions. From S_1 again fluorescent light can be emitted but now with a far longer decay time.

2.1.4. Lifetime and quantum yields

Contrary to many books the quantum yield and lifetime of phosphorescence and *not* fluorescence is examined here. To describe the process deactivation rates are introduced which can be calculated as the inverse of the associate lifetime (compare fig. 2.6):

$$
\left.
\begin{array}{ll}
k_r^S & \text{rate constant for radiative deactivation from } S_1 \rightarrow S_0 \\
k_{ic}^S & \text{rate constant for internal conversion from } S_1 \rightarrow S_0 \\
k_{isc} & \text{rate constant for intersystem-crossing from } S_1 \rightarrow T_1 \\
k_r^T & \text{rate constant for radiative deactivation from } T_1 \rightarrow S_0 \\
k_{nr}^T & \text{rate constant for non-radiative deactivation from } T_1 \rightarrow S_0
\end{array}
\right\} \quad k_{nr}^S = k_{ic}^S + k_{isc}
$$

Lifetime of phosphorescence

If a sufficiently populated T_1 state can be assumed (e.g. by a preceding short light pulse) the kinetics of the deactivation process can be described as,

$$-\frac{d[L^{T1}]}{dt} = (k_r^T + k_{nr}^T)[L^{T1}] \tag{2.5}$$

where k_r^T is the radiative deactivation from $T_1 \rightarrow S_0$ and k_{nr}^T describes the non-radiative deactivation rate of $T_1 \rightarrow S_0$. $[L^{T1}]$ is the concentration of luminophores in the excited triplet state. If the *initial concentration* of luminophores was $[L^{T1}]_0$ the solution of this equation is:

$$[L^{T1}] = [L^{T1}]_0 \, \mathrm{e}^{-t/\tau_0} \tag{2.6}$$

where τ_0 is the lifetime of the T_1 state:

$$\tau_0 = \frac{1}{k_r^T + k_{nr}^T} \tag{2.7}$$

The number of emitted phosphorescence photons per second $i_P(t)$ is proportional to k_r^T and can be written as,

$$i_P(t) = N_a k_r^T [L^{T1}]_0 \, \mathrm{e}^{-t/\tau_0} \tag{2.8}$$

which can be interpreted as the δ-impulse response of the phosphorescent light. The time when the light intensity is reduced to $1/\mathrm{e}$ of the initial intensity is defined as *decay time* which here is the same as the lifetime of the excited state. Of course, in practical applications only a fraction of the luminescence light can be captured, but if the captured light is strictly proportional to the emitted light, the transient characteristic does not change.

Quantum yield of phosphorescence

The phosphorescence quantum yield Φ_P is defined as the fraction of emitted phosphorescence photons to absorbed photons and can be written in terms of the intersystem-crossing quantum yield as:

$$\Phi_P = \frac{k_r^T}{k_r^T + k_{nr}^T} \Phi_{isc} \tag{2.9}$$

$$\Phi_{isc} = \frac{k_{isc}}{k_r^S + k_{nr}^S} \tag{2.10}$$

The steady state phosphorescence light intensity I_P is proportional to the quantum yield, where αI_0 represents the amount of absorbed photons, I_0 represents the incident *constant* light and eqn. 2.2 specifies α to be $1 - T(\lambda)$:

$$I_P = \Phi_P \alpha I_0 \tag{2.11}$$

Phosphorescence in a system-oriented approach

If this system of a luminophore with incident light as input and phosphorescent light as output signal can be assumed to be linear and time-invariant (LTI), the transfer function of this system can be written as,

$$H_P(j\omega) = \frac{I_P(j\omega)}{\alpha I_0(j\omega)} \tag{2.12}$$

with $I_0(j\omega)$ and $I_P(j\omega)$ denoting the Fourier-transformed input and output signals and $\omega = 2\pi f$ as the angular frequency in rad/s. The transfer function of this system can then be derived by the Fourier-transform of the impulse-response from eqn. 2.8:

$$\mathcal{F}\{i_P(t)\} = N_a k_r^T [L^{T1}]_0 \frac{\tau_0}{1 + j\omega\tau_0} = \Phi_P \frac{1}{1 + j\omega\tau_0} \tag{2.13}$$

This transfer function is formally known as a first order low-pass filter with a cut-off frequency of $f_c = 1/2\pi\tau_0$ and only a fraction of the incident light is absorbed (α) and excites the luminophore. The whole process of light absorption and phosphorescence can then be depicted systematically as in fig. 2.7.

2.1.5. Intermolecular deactivation processes

Other species can deactivate the excited luminophore by either collision, electron transfer, excimer or exciplex formation, proton transfer or energy transfer, but only if the lifetime of the process is in the range of the lifetime of the excited state. Compared to fluorescence a lot more processes can quench phosphorescence, because of the much longer lifetime of the triplet state.

Quenching refers to any process which can decrease the amount of luminescent light, which extends the possibilities by processes such as ground-state complex formation (static quenching).

Only dynamic quenching - also known as collisional quenching - is explained later on as a deactivation process, however, other ones such as resonance energy transfer (RET) or photoreactions can play a big role in photoluminescence but are not part of the focus of this work.

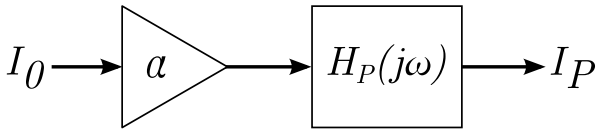

Figure 2.7.: The signal chain of light absorption and phosphorescence when the luminophore is described as a LTI system.

Static quenching

In this process the quencher actually does not deactivate the luminophore, however, it reduces the amount of luminescent light by forming complex with the luminophore, resulting in either a different excitation or emission spectrum of the complex. Both variants would change the amount of emitted light at a specific wavelength as a function of the quencher concentration and reduces the quantum yield as shown in fig. 2.8(b).

$$\frac{\Phi_0}{\Phi} = 1 + K_{SV}[Q] \tag{2.14}$$

This process only reduces the actual amount of luminophores but it does not change anything about the lifetime of the excited states of the luminophore and therefore the transient response still stays the same, which means that the decay time of the luminescence light will be constant.

$$\tau([Q]) = \tau_0 \tag{2.15}$$

The formation of the complex will get more unlikely if thermal energy rises, thus by increasing the temperature the quenching constant (K_{SV}) will decrease. These last two features can help to distinguish between static and dynamic quenching.

Dynamic quenching

In dynamic quenching an excited luminophore is deactivated as it collides with another species which gets excited in this process. The collision has to happen while the luminophore is in its excited state, therefore the root-mean square distance $\sqrt{\Delta x^2}$ over which a quencher can diffuse during this lifetime affects the probability of a collision. Of course, given a certain concentration the higher the temperature the better diffusion works and the more likely a collision will happen, which explains why dynamic quenching normally increases with temperature. Oxygen is one of the best known quenchers working like this and is also used in this work to modify phosphorescence.

The rate of collisions can be described as the multiplication of the diffusion-controlled bimolecular rate constant k_0 with the quencher concentration $[Q]$. By multiplying k_0 with the efficiency f_Q of a collision to deactivate the luminophore the quenching constant $k_q = f_Q k_0$ is obtained. Thus a new deactivation rate can be introduced in the reaction kinetics for the triplet state (see eqn. 2.5):

$$-\frac{d[L^{T1}]}{dt} = (k_r^T + k_{nr}^T + k_q[Q])[L^{T1}] \tag{2.16}$$

The triplet state now has a shorter lifetime, compared to the lifetime without quencher:

$$\tau = (k_r^T + k_{nr}^T + k_q[Q])^{-1} \quad \text{v.s.} \quad \tau_0 = (k_r^T + k_{nr}^T)^{-1}$$

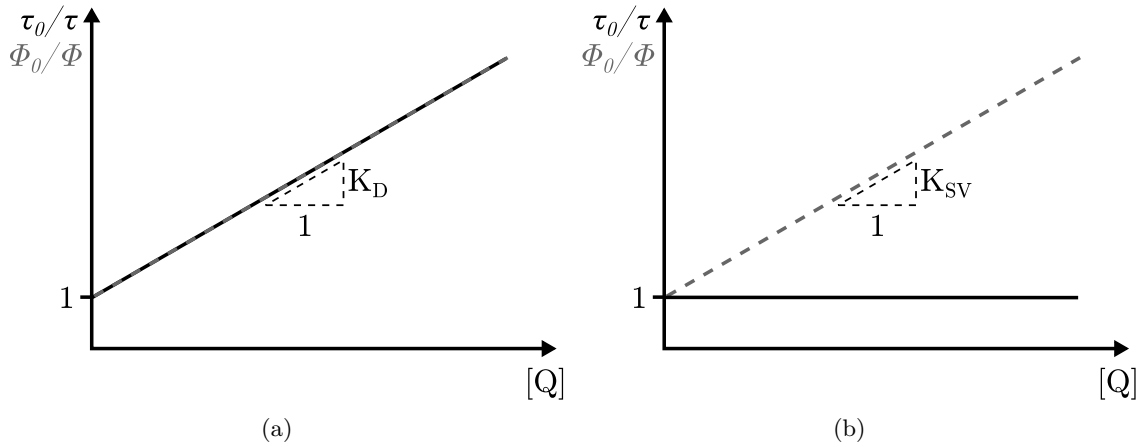

(a) (b)

Figure 2.8.: The relation between Φ_0/Φ and τ_0/τ as a function of $[Q]$ for dynamic quenching (a) and static quenching (b).

The additional deactivation rate also decreases the quantum yield compared to the quantum yield without quencher.

$$\Phi = \frac{k_r^T}{k_r^T + k_{nr}^T + k_q[Q]}\Phi_{isc} \quad \text{v.s.} \quad \Phi_0 = \frac{k_r^T}{k_r^T + k_{nr}^T}\Phi_{isc}$$

These effects can be summarised by the Stern-Volmer equation for dynamic quenching (see also fig. 2.8(a)):

$$\frac{\Phi_0}{\Phi} = \frac{\tau_0}{\tau} = 1 + \underbrace{k_q\tau_0}_{\equiv K_D}[Q] \tag{2.17}$$

The last equation is an idealised imagination of this collision process, however, there are many factors which can disturb this linear relationship, such as:

- The quenching constant is a function of time, which is more relevant in very viscous media and with shorter lifetimes of the luminophore. Then the transient luminescence decay wouldn't be a single exponential any more.
- Simultaneous dynamic and static quenching by the same quencher results in much more loss of intensity at higher concentrations, the decay time does not change however.
- Inhomogeneous media with different quenching constants distributed over the volume (two site model) results in a superposition of two Stern-Volmer equations.

Thus in many cases the actual behaviour of the luminophore deviates from the simple Stern-Volmer equation (see fig. 2.9) and must be determined empirically. A modified (or extended) Stern-Volmer equation can then be used to describe the deviations and provides a better fit to the measurements. A commonly used modification to describe a less efficient dynamic quenching with higher quencher concentrations (down-ward curved plot in fig. 2.9) is the two-site model [19]:

$$\frac{\tau_0}{\tau} = \left(\frac{f}{1 + K_{D1}[Q]} + \frac{1-f}{1 + K_{D2}[Q]}\right)^{-1} \tag{2.18}$$

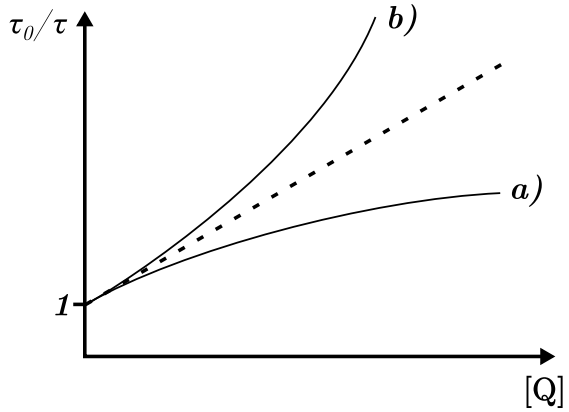

Figure 2.9.: Different possible deviations from the linear Stern-Volmer equation for τ_0/τ. Curve a) represents less efficient quenching for higher concentrations (e.g. inhomogeneous media) and curve b) represents better quenching with higher concentrations (e.g. simultaneous static and dynamic quenching).

By choosing the right values for f and K_{D1}, K_{D2} a good fit to down-warded deviations can be achieved. Physically the model can be thought to describe the behaviour of two differently quenched fractions of the same luminophore.

2.2. Luminescence decay time measurements

The decay time is an easy accessible and intrinsic referenced parameter of luminophores, which means that it is mostly independent of external parameters such as incident light intensity and luminophore concentration. Other parameters (e.g. luminescent light intensity) are heavily affected by external parameters and need to be measured against a reference luminophore [20]. If the behaviour of the luminophore under standard conditions is known, the actual decay time can provide information about quenching concentration, temperature, etc.

In principle there are two ways to determine the decay time, namely in the time domain (TD) or in the frequency domain (FD). In both cases excitation light signal is applied to the luminophore, the emitted light signal is recorded and by assuming a model for the luminophore the decay time as a free parameter can be determined. Other parameters which influence the decay time can then be derived from it. Very often the model is described by a simple mono-exponential decay (eqn. 2.5), i.e. a first-order low-pass filter (eqn. 2.13) is assumed.

2.2.1. Time domain

This method excites the luminophore with a single and as short as possible light pulse in order to populate the T_1-state. Following the excitation pulse the time dependent intensity of the emission light is recorded and according to the used model a curve can be fitted into the measurement points. In many cases a mono-exponential decay is assumed and would result in

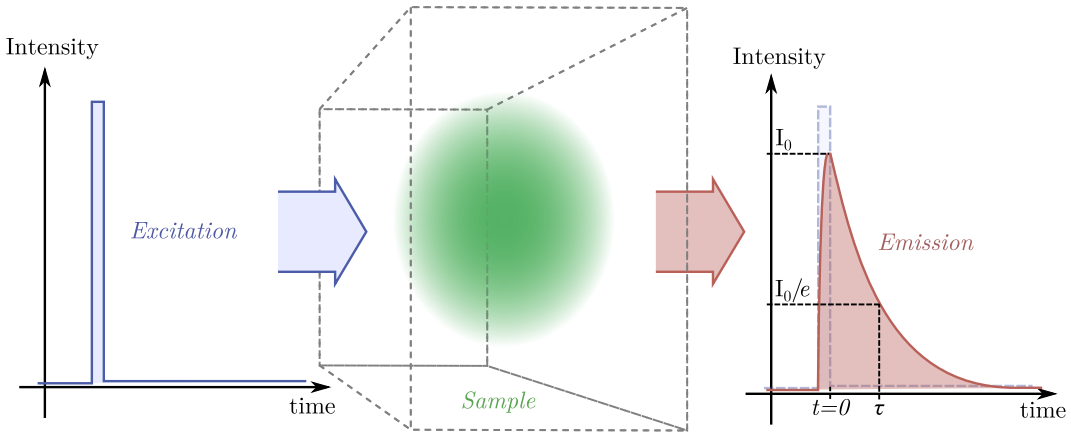

Figure 2.10.: Principle setup of a time domain lifetime measurement system.

a linear slope if the log of the emitted light is plotted against the time. The characteristic decay time can then be easily calculated from the slope of the plot (see fig. 2.10).

In real systems many effects have to be considered to get good measurement results, such as the convolution of the emission light with the device (lamp) function and also every delay and distortion in the instrumentation circuit will influence the measured curve. Although very powerful devices have evolved which overcome most of these problems - e.g. time-correlated single-photon counting (TCSPC) - the instrumentation effort is really high. Another way to eliminate those problems is to utilise a powerful digital signal processor and deconvolute the signal in real-time and calculate the decay time with a fitting algorithm. All these expenses offer the big advantage of more or less directly measuring the impulse response of the luminophore.

2.2.2. Frequency domain

This method uses a sinusoidal modulated light source instead of a short pulsed light peak to excite the sample (as shown in fig. 2.11). During the excitation also the emission light is recorded - a sinusoid with the same frequency again - and the phase shift in between the excitation light and emission light can be used to derive the lifetime of the luminophore. The derivation on how the lifetime is connected with the phase shift is given in [15], however, it might be useful to also look at it in a system-oriented approach , which will yield the same result.

It already was explained how the luminophore can be seen as an LTI-system in eqn. 2.13 and in many cases it behaves like a first order low-pass filter. The output of such a system can then be easily calculated by using the transfer function $H_P(\mathrm{j}\omega)$ of it, which represents the eigenvalue for input signals of the form $x(\omega) = A\,\mathrm{e}^{\mathrm{j}\omega t}$ (eigensignals for LTI-systems) [21]. Thus the output of such a system can be written as:

$$y(\omega) = H_P(\mathrm{j}\omega) \cdot A\,\mathrm{e}^{\mathrm{j}\omega t} = A \cdot |H_P(\mathrm{j}\omega)| \cdot \mathrm{e}^{\mathrm{j}\omega t + \angle H_P(\mathrm{j}\omega)} \tag{2.19}$$

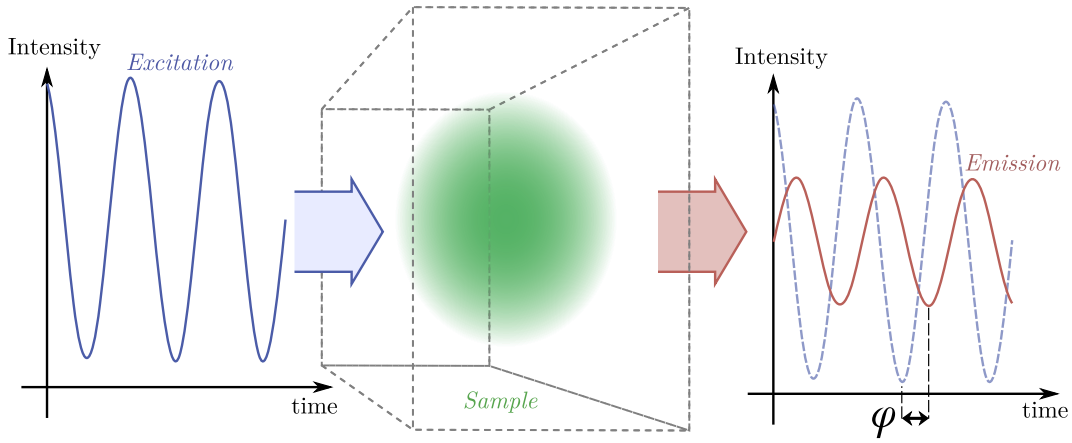

Figure 2.11.: Principle setup of a frequency domain lifetime measurement system.

This shows that the output signal is again an eigensignal with the amplitude being the amplitude of the input multiplied by the absolute value of transfer function and the phase being shifted by the argument of the transfer function. As a sine and cosine can be represented as a sum of eigensignals the same rules apply to them. Therefore the modulation $m(\omega) = |y(\omega)|/|x(\omega)|$ and phase shift caused by the system can be calculated just by looking at the transfer function:

$$m(\omega) = |H_P(\mathrm{j}\omega)| \tag{2.20}$$

$$\phi(\omega) = \angle H_P(\mathrm{j}\omega) \tag{2.21}$$

Putting in the derived transfer function of a phosphorescent luminophore from eqn. 2.13 with accounting for quenching in τ and Φ from 2.1.5 the modulation and phase shift can be simply written as:

$$m(\omega) = \left|\Phi \frac{1}{1+j\omega\tau}\right| = \Phi \frac{1}{\sqrt{1+\omega^2\tau^2}} \tag{2.22}$$

$$\phi(\omega) = -\angle\left(\Phi \frac{1}{1+j\omega\tau}\right) = \arctan(\omega\tau) \tag{2.23}$$

$$\tau = \frac{\tan\phi(\omega)}{\omega} \tag{2.24}$$

Describing the luminophore like this makes it really easy to solve complex systems, as long as they stay linear, time-invariant and their transfer function can be derived. This scheme can also be used for different input signals when they can be Fourier-transformed (i.e. described as sums of sine- and cosine waves). It also shows when measuring the sample with many different modulation frequencies that actually the transfer function is evaluated at many points which can give more insight into the system, e.g. if it performs like a first-order low-pass filter or if there are two ore more systems with different lifetimes in the sample.

2.2.3. Phase resolution

In frequency domain measurements the phase carries the information of the captured luminescence light and the excitation modulation frequency is the main parameter to tune the phase

resolution. As the connection between phase angle and oxygen partial pressure is described by eqn. 2.17 and eqn. 2.24 an optimal frequency can be derived, where the phase resolution according to a change in oxygen partial pressure is a maximum.

Optimisation of the absolute phase change

The first approach is to look for the absolute phase change in a partial oxygen pressure range of interest. By calculating the phase change for this range (between partial pressure $pO_{2,1}$ and $pO_{2,2}$ a frequency can be selected to maximise it.

$$\phi_1 = \arctan(\omega\tau_1) \quad \text{and} \quad \phi_2 = \arctan(\omega\tau_2) \qquad \text{with} \quad \tau(pO_{2,1}) = \tau_1, \quad \tau(pO_{2,2}) = \tau_2$$

Eqn. 2.25 shows the optimal frequency when maximizing $\Delta\phi(\omega) = \phi_2 - \phi_1$ with respect to the frequency to be the geometrical mean of the inverse of the decay time constants:

$$\omega_{opt} = \arg\max_{\omega} \Delta\phi(\omega) \Rightarrow \frac{d\Delta\phi}{d\omega} = 0 = \frac{\tau_2}{1 + (\omega_{opt}\tau_2)^2} - \frac{\tau_1}{1 + (\omega_{opt}\tau_1)^2}$$

$$\omega_{opt} = \sqrt{\frac{1}{\tau_1\tau_2}} \tag{2.25}$$

This formula should be considered if a sensor should have a good performance over a range of partial oxygen pressures. However, over this range the phase resolution is not constant and decreases with higher partial oxygen pressures (also see fig. 2.12).

Optimisation of the relative phase change

If the sensor should perform best at a particular partial oxygen pressure the relative phase change ($\frac{\delta\phi}{\delta pO_2}$) has to be maximised with respect to the frequency..

$$\frac{\delta\phi}{\delta pO_2} = \frac{\omega\tau}{1 + (\omega\tau)^2} \cdot (-K_D)\frac{\tau}{\tau_0} \qquad \text{where} \quad \tau = f(pO_2) \tag{2.26}$$

$$\omega_{opt} = \arg\max_{\omega} \frac{\delta\phi}{\delta pO_2} \Rightarrow \frac{\delta^2\phi}{\delta pO_2\delta\omega} = 0$$

$$\omega_{opt} = \frac{1}{\tau} \tag{2.27}$$

If this frequency is used to stimulate the luminophore it will result in a phase shift of 45 degrees and the best phase resolution for the selected partial oxygen pressure [22]. The optimal frequency for a many particular partial oxygen pressures is shown in fig. 2.13 as a blue line and the *constant* frequency to optimise the whole range is emphasised with a blue circle.

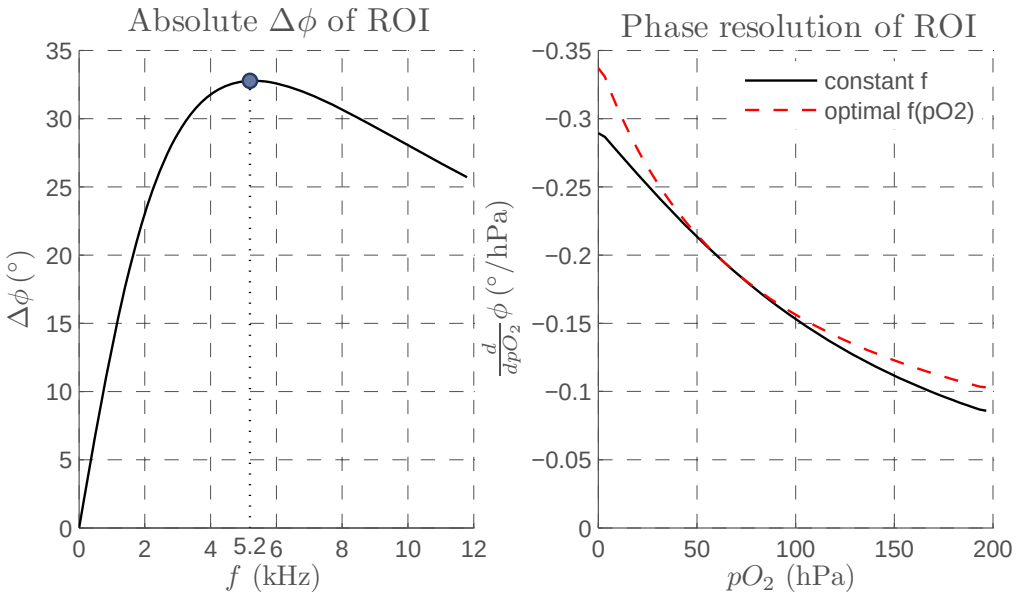

Figure 2.12.: On the left-hand side the absolute phase shift over a pO_2-range of interest [0-200]hPa is shown with the best frequency around 5kHz for a luminophore with 55 μs decay time and $K_D = 0.012\,\mathrm{hPa}^{-1}$. On the right-hand side the varying phase resolution over this pO2-range with a constant frequency optimal for this range of interest is shown. Also the optimum phase resolution which could be achieved with a varying frequency is plotted.

Optimal phase resolution

The achieved phase resolution with the frequency derived in eqn. 2.27 can be calculated if this frequency is put in eqn. 2.26. This derivation is just a small extension to the one presented in [22]:

$$\left.\frac{d\phi}{dpO_2}\right|_{\omega=1/\tau} = -\frac{1}{2}\frac{\tau}{\tau_0}K_D \tag{2.28}$$

So note can be taken that the phase resolution in the best case (perfect matched ω) linearly depends on K_D and $\tau = f(pO_2)$. The phase resolution degrades in high oxygen concentration (where $\tau \ll \tau_0$). This formula is especially interesting for low oxygen concentration where $\tau/\tau_0 \approx 1$. Then the only option for a good resolution is to design a sensor with a high K_D.

The phase resolution described in eqn. 2.28 is a best case scenario, thus for most applications where ω is a fixed frequency this resolution will be decreased according to fig. 2.12. Of course, a system could be designed to tune the excitation modulation frequency until the phase shift of the output signal is exactly 45 °. The resulting frequency would correspond to the partial oxygen pressure ($\omega = 1/\tau = (1 + K_D pO_2)/\tau_0$) and the sensor would perform with the best phase resolution in the whole range of interest, but the advantage does not pay off.

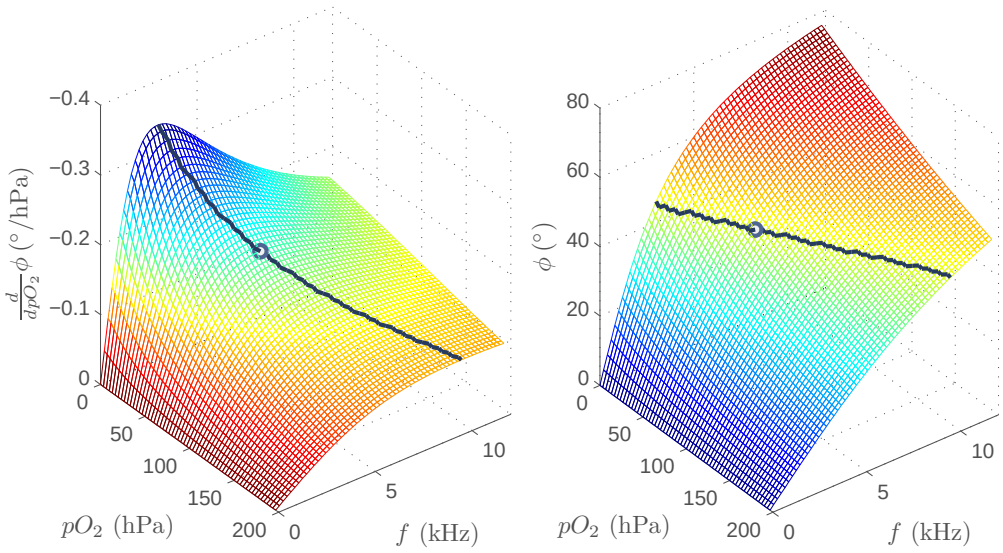

Figure 2.13.: On the left the phase resolution for every possible pO_2 and frequency is shown for a luminophore with $\tau_0 = 55\,\mu s$ and $K_D = 0.012\,\text{hPa}^{-1}$. The right diagram shows that this frequency yields in a phase shift of 45 degrees.

2.3. Components and circuits

In order to measure the decay time of a luminophore in the frequency domain a sinusoidal modulated light intensity with the right wavelength is needed. LEDs can be used as light source for luminophores with a good fit to the emission spectrum of LEDs [23]. In order to measure the emitted light photodiodes very often provide the best compromise between size, power consumption and sensitivity to detect this signal. To separate excitation light from emission light optical filters are used. The driving and instrumentation circuits for these opto-electronic components are described in this section, as well as their characteristics.

2.3.1. Noise in components and circuits

As noise is a random process only statistical quantities can be used to describe it, such as the voltage noise density:

$$|u_n(f)|^2 = \frac{du_{neff}^2}{df} \tag{2.29}$$

By integration over the frequency one can determine the effective noise voltage, which can be used to describe how much noise power a resistor would generate ($P_n = u_{neff}^2/R$). However, this does not say anything about the actual value of the noise signal amplitude [24].

$$u_{neff} = \sqrt{\int_0^\infty |u_n(f)|^2 df} \tag{2.30}$$

Component noise

Thermal noise A resistor shows thermal noise, where the noise power is just dependent on the temperature and equally distributed over the frequency band. The noise voltage density therefore is:

$$|u_{R,n}|^2 = 4kTR \quad \Rightarrow \quad |u_{R,n}| \approx 0.13\,{}^{nV}/\sqrt{\text{Hz}} \cdot \sqrt{R/\Omega} \quad \text{at } 300\,\text{K} \tag{2.31}$$

PN-junction noise A *pn*-junction generates shot-noise due to the unsteady flow of charges because of recombination processes and it appears in every diode. It is caused by a statistical distribution of the transit times of the generated charges across the diode and is a so-called *white* noise, i.e. equally distributed over the frequency band.

$$|i_{D,n}|^2 = 2q_e I_D \tag{2.32}$$

Input referred noise In many electronic components such as transistors and OPAs all different internal noise sources are referred to the input of the device, which simplifies noise calculations (see fig. 2.14). In general these noise sources are not *white* and are most often higher in lower frequencies. It is often called *pink* noise and refers to the spectrum of visible light.

Noise in circuits

Noise in circuits follows similar rules as signals do, however, the statistical property of the signal must be kept in mind. The noise signal at the output node of a system can be calculated from the noise signal at the input node with the transfer function of the system.

$$|u_{no}(f)|^2 = |H(j2\pi f)|^2 |u_{ni}(f)|^2 \tag{2.33}$$

Different noise sources can be added up geometrically $|u_n|^2 = |u_{n1}|^2 + |u_{n2}|^2 + \ldots$ if they are not correlated, which in most cases is approximately true. Noise sources would have to be treated differentially if their cross-correlation is not equal to zero:

$$r_{xy}(\tau) = \lim_{T\to\infty} \frac{1}{T} \int_{-T/2}^{T/2} x(t)y(t-\tau)dt \tag{2.34}$$

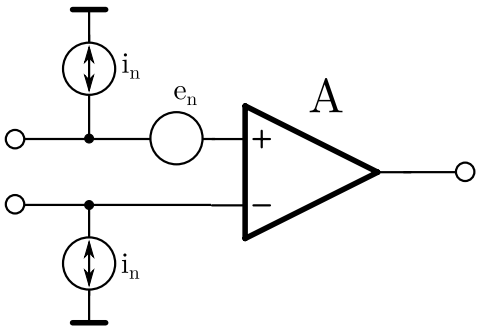

Figure 2.14.: Input referred noise sources of an OPA.

For a good performance every noise component has to be considered and the impact on the output of the circuit has to be determined. As the sources do not add up linearly but squared the output noise can be heavily determined just be one major noise component and a reduction of smaller noise components in the circuit won't significantly decrease the noise power.

2.3.2. Optical components

Different kinds of filters and light fibres can be used to specifically guide or block light dependent on its wavelength.

Glass and interference filters

Glass filters are often available in a short- or long-pass configuration and simply used for blocking light. Some important parameters for filters are:

Transmittance $\tau(\lambda)$ The ratio of transmitted to incident light intensity

Internal transmittance $\tau_i(\lambda)$ The ratio of transmitted light intensity to the amount of light that enters the filter, i.e. the transmittance without considering the losses of reflection.

Cut-off wavelength λ_c The wavelength where the internal transmittance is half of the transmittance in the pass-band region of the filter.

Interference filters transmit or reflect light depending on the wavelength by destructive interference. On side of a carrier is coated with several thin layers with different refractive indices and interference leads to annihilation or transmission of the incident light. These filters can be used to split beams depending on their wavelength. Care should be taken which side of the filter is coated.

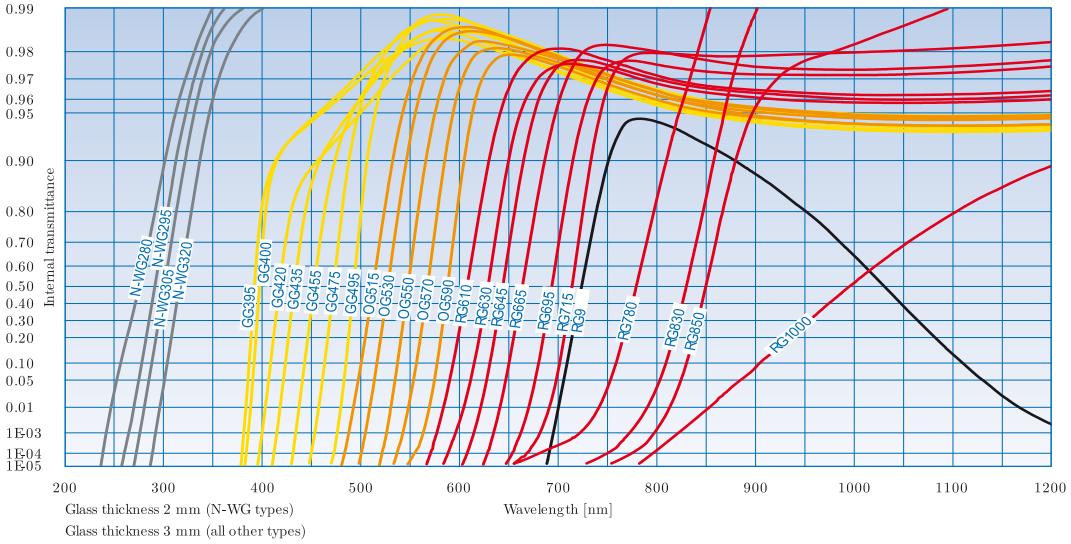

Figure 2.15.: Internal transmittance vs. wavelength of several different long-pass glass filters (also including the RG-9 filter, black line) from Schott AG.

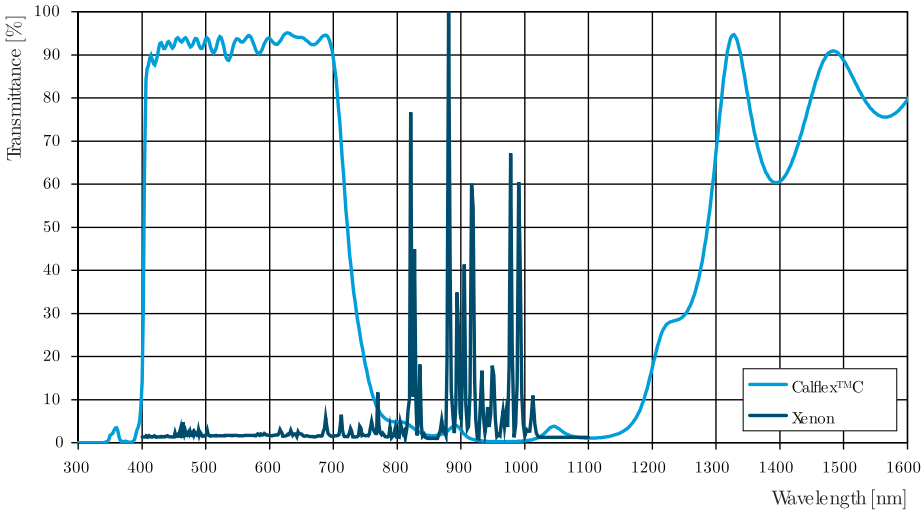

Figure 2.16.: Transmittance spectrum of a NIR-blocking interference filter (CalFlex) from Optics Balzer AG referred to a Xenon-lamp spectrum

Typical filter transmittance spectra can be seen in fig. 2.15 and fig. 2.16, e.g. long-pass filters from Schott AG[1] and an interference-filter from Optics Balzer AG[2].

Light fibres

Light fibres (see fig. 2.17) can guide light inside the fibre. The difference in refraction indices between cladding and core lead to total internal reflection and also determine the angle of acceptance. This angle should be as high as possible to efficiently capture light from a diffuse light source. Depending on the used material light fibres have different attenuation coefficients (absorption per unit length) for different wavelengths, thus they must be matched to the excitation and emission wavelength as well.

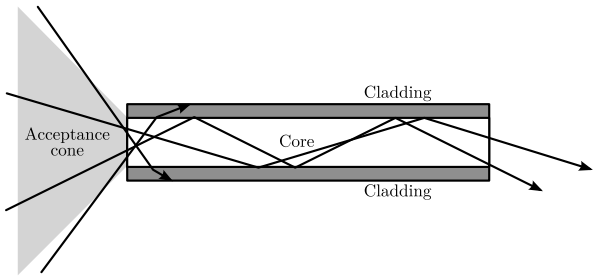

Figure 2.17.: Demonstration of light guiding with an optical fibre.

[1]SCHOTT AG, Hattenbergstrasse 10, 55122 Mainz, Germany, http://www.schott.com/
[2]Optics Balzers Jena GmbH, Carl-Zeiss-Promenade 10, 07745 Jena, Deutschland, http://www.opticsbalzers.com/

2.3.3. Opto-electronic components

The performance of the opto-electronic parts (LEDs and photodiodes) used for a phase fluorometer determine the achievable accuracy and efficiency of the measurements and have to be selected according to the used luminescence sensor.

LED characteristics

A light emitting diode is basically a pn-junction diode, in which the electron hole pair recombination results in the emission of a photon (electro-luminescence). The photon energy is approximately equal to the bandgap energy of the semiconductor ($E_g = h\nu$) and thus depends on the used semiconductor material. If a forward bias voltage is applied to the LED the built-in potential barrier V_0 is reduced and allows electrons from the n^+ side of the diode to diffuse to the p side and also holes to be injected vice-versa, however this part is much smaller. The recombination of electrons with holes then results in spontaneous emission of photons (see fig. 2.18).

The typical characteristics of InGaAlP-LEDs can be seen in fig. 2.19. The wavelength at peak intensity and the linewidth of the spectrum are related to the distribution of electrons and holes in the conductance and valence band. In general the electro-luminescence described here works similar to the photo-luminescence described in section 2.1.

The *turn-on voltage* of a LED depends also on the bandgap energy and is the point where the current increases sharply with the voltage. Typically for a blue LED this voltage is about 3.5 V and can go down to about 1 V for infrared LEDs.

Forward current and light intensity should be very linear as every electron-hole recombination excites a photon, however, at high current levels a strong injection of minority carriers can lead

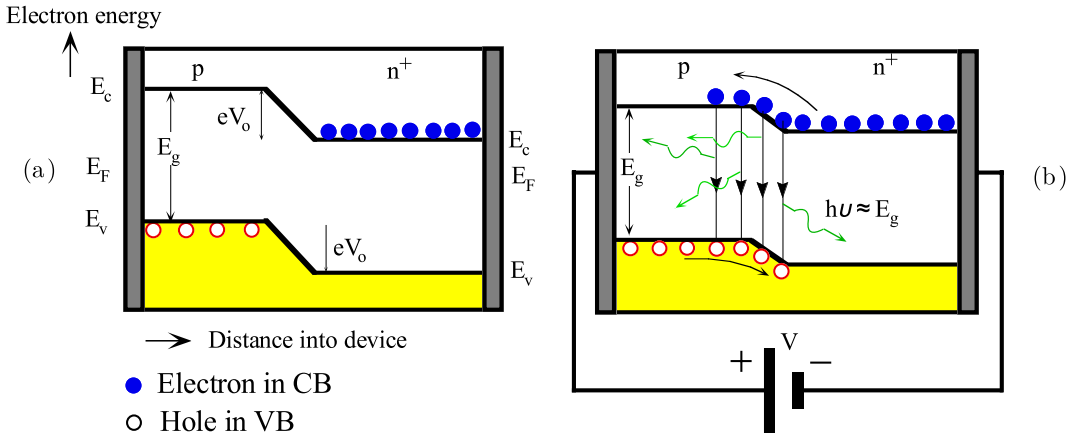

Figure 2.18.: (a) The energy band diagram of a p - n^+ (heavily n-type doped) junction without any bias. Built-in potential V_0 prevents electrons from diffusing from n^+ to p side. (b) The applied bias reduces V_0 and thereby allows electrons to diffuse, be injected, into the p-side. Recombination around the junction and within the diffusion length of the electrons in the p-side leads to photon emission. [17]

to a current dependent recombination time (diffusion length) and this leads to a non-linear recombination rate, which can be seen in a reduced slope of the light intensity for higher currents. Additionally the junction temperature also affects the light output as thermal non-radiative recombination will more and more compete with radiative recombination.

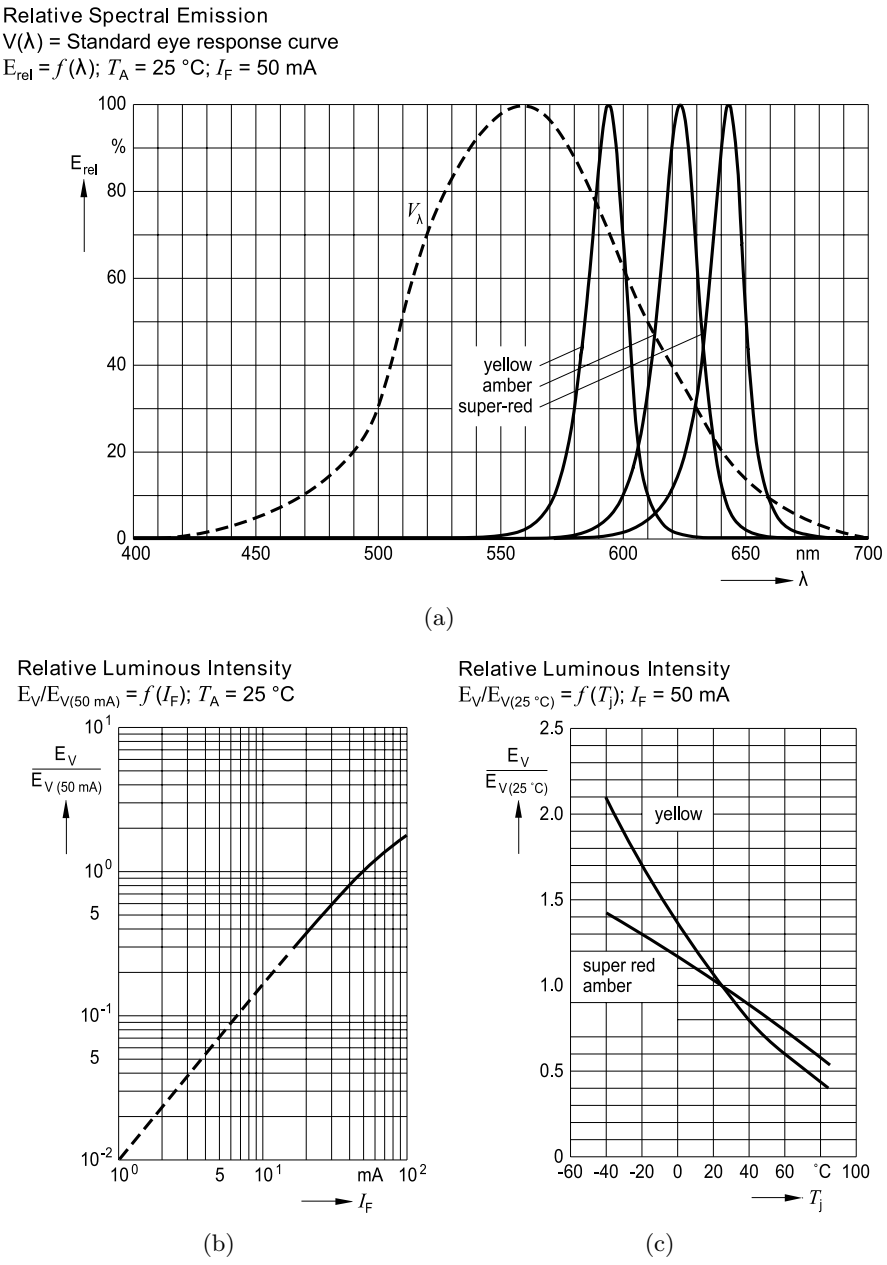

Figure 2.19.: (a) Relative spectral emission spectrum with the standard luminosity function from InGaAlP-LEDs. (b) The relative luminous intensity with respect to the forward current is very linear for a specific temperature. (c) The temperature influences many parameters - including the efficiency - of a LED.

Photodiode characteristics

Photodiodes - as many photodetectors - utilise the fact that a photon can induce an electronic transition by absorption. In a semiconductor a free electron hole pair (EHP) is generated only if the absorbed photon energy is higher or equal to the bandgap energy between valence and conduction band. The *upper cut-off wavelength* can be expressed in terms of the bandgap energy:

$$\lambda_g = \frac{hc}{E_g} \tag{2.35}$$

The photon absorption has similar properties as explained earlier in section 2.1.2. Most of the photons (63 %) will be absorbed over a distance of $1/\mu_a$ called *penetration depth* δ, where $\mu_a(\lambda) = \varepsilon(\lambda) \cdot c$ is the absorption coefficient for the used semiconductor material. The depletion region of the photo-diode should ideally cover most of the penetration depth, which is nowadays ensured by using PIN-photodiodes.

If such an EHP is generated in the depletion region of a photodiode the electron and hole get separated driven by the intrinsic electrostatic field and drift to the neutral regions of the semiconductor, where they can recombine (see fig. 2.20). The recombination leads to a flow of current I_{ph} in an external circuit and depends on the number of EHPs generated and their drift velocities in the semiconductor. EHPs generated outside the depletion layer can also contribute to the photo-current as the electron (or hole) can diffuse to the depletion region, where the intrinsic field then will accelerate the electron to drift to the neutral region of the n side.

The quantum efficiency - similarly to the quantum yield in luminescence - describes how many EHPs are generated and converted into a photo-current I_{ph} per incident photon (which is the incident optical power P_0 divided by the energy of a photon):

$$\eta = \frac{I_{ph}/q_e}{P_0/(h\nu)} \tag{2.36}$$

The responsivity R is found in many datasheets and relates the photo-current to the incident optical power. Eqn. 2.37 also explains why R increases linearly with λ in an ideal photodiode (see fig. 2.22(a)) until λ_g.

$$R = \frac{I_{ph}}{P_0} = \eta \frac{q_e \lambda}{hc} \tag{2.37}$$

The electrical equivalent model of a photodiode consists of a current source in parallel with an ideal diode (fig. 2.21(a)). Additionally there is a junction capacitance C_j (caused by charge distribution in the depletion region) and a shunt resistance R_{sh} in parallel and a series bulk resistance of the semiconductor material and electrodes R_s in this model.

The I-V characteristics of the photodiode is similar to a normal diode, however, a photo-current depending on the incident light power and the responsitivity has to be added as in fig. 2.21(b) to the curve. An ideal diode can be described by:

$$I_D = I_S \left(\mathrm{e}^{q_e U/kT} - 1 \right) \tag{2.38}$$

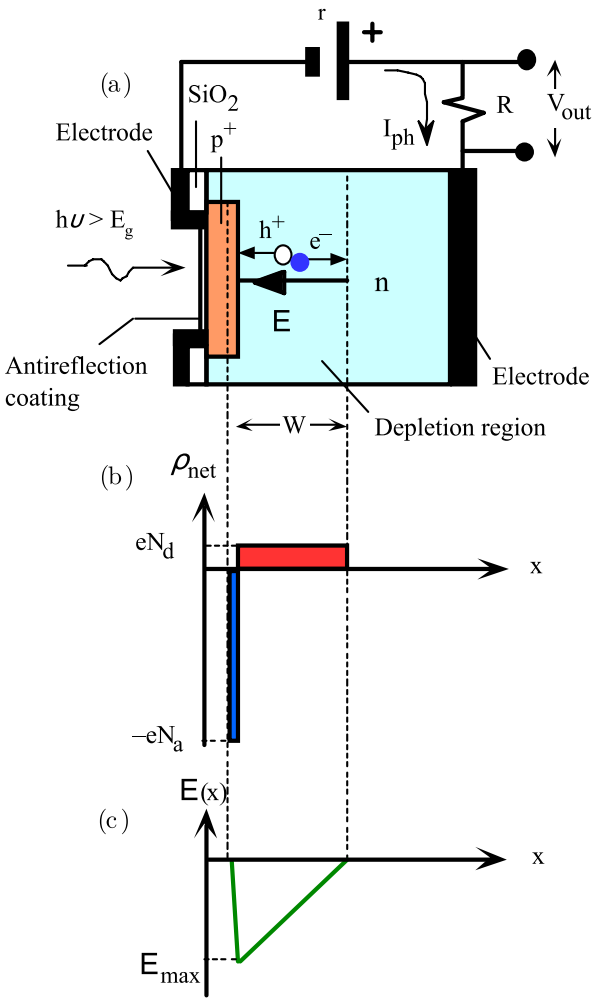

Figure 2.20.: (a) A schematic diagram of a reverse biased *pn* junction photodiode. (b) Net space charge density across the diode in the depletion region. N_d and N_a are the donor and acceptor concentrations in the n and p sides. (c) The field in the depletion region. [17]

The shunt resistance describes the resistance of the photodiode at $U = 0\,\mathrm{V}$ and adds a thermal noise to the photodiode performance:

$$i_{th}^2 = \frac{4kTB}{R_{sh}} \tag{2.39}$$

If a pn-junction or PIN photodiode is reverse biased and not illuminated a current I_S due to the thermal generation of EHPs in the depletion layer continues to flow. In photodiodes this is called dark current I_d. Together with the photo-current they produce noise, i.e. fluctuations about $I_d + I_{ph}$ - see *shot-noise* in 2.3.1. The total noise current referred to the photo-detector bandwidth B can be calculated as:

$$i_n^2 = i_{n,d}^2 + i_{n,ph}^2 + i_{th}^2 = 2q_e(I_d + I_{ph})B + \frac{4kTB}{R_{sh}} \tag{2.40}$$

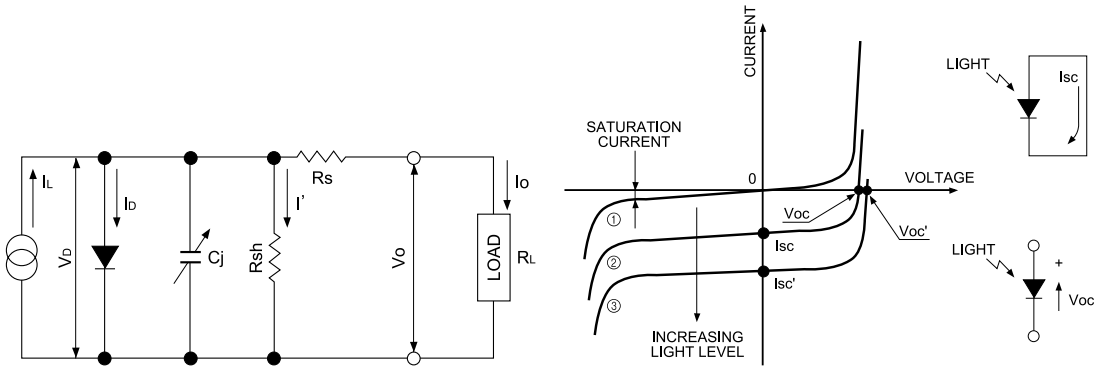

(a) (b)

Figure 2.21.: (a) Equivalent circuit diagram of a photodiode. (b) Characteristic I-V curve of a photodiode in forward and reverse bias mode for increasing light levels. [25]

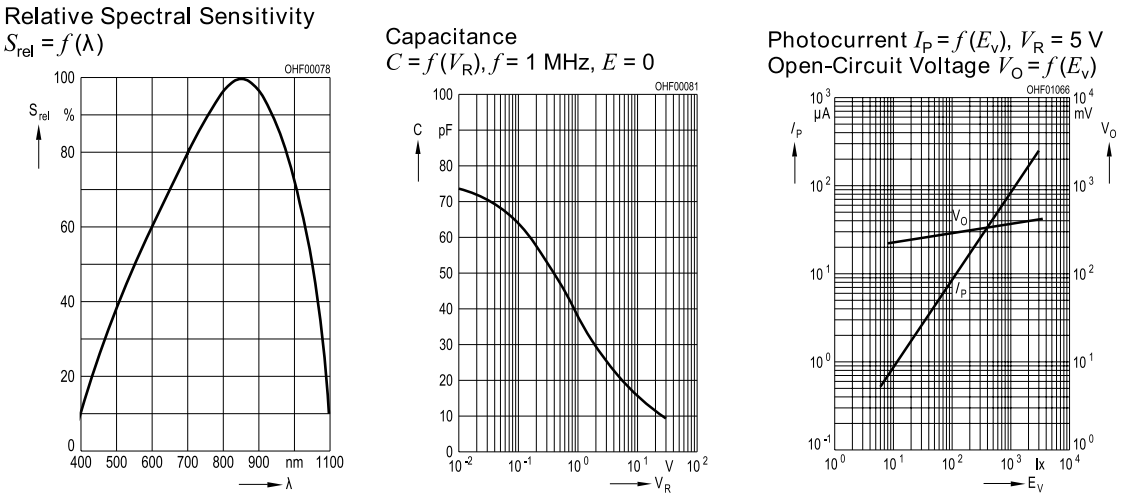

(a) (b) (c)

Figure 2.22.: (a) The responsitivity of a standard silicon PIN photodiode vs. the wavelength normalised to the maximum responsitivity at 850nm, which shows a typical cut-off wavelength λ_g of about 1.11 μm for Si-diodes. (b) The junction capacitance varies with the applied reverse bias voltage and limits the detector bandwidth. (c) The relation between light and current is extremely linear in a photodiode.

The rise and fall times of a photodiode are defined as a 10 % to 90 % signal change and are dependent of three different factors:

- The drift time of EHPs generated in the depletion layer.
- The diffusion time of EHPs generated outside the depletion layer
- The RC rise / fall time constant of the diode circuit

All three times can be added up to a total rise / fall time which also roughly determines the 3dB bandwidth of the photodiode:

$$t_R = \sqrt{t_{drift}^2 + t_{diffusion}^2 + t_{RC}^2} \approx \frac{0.35}{f_{3db}} \tag{2.41}$$

The junction capacitance is one limiting factor for the achievable bandwidth of the detection system and depends on many parameters (diffused area, depletion width, etc.). It can be decreased with the applied reverse bias voltage (see fig. 2.22(b)) in order to increase the signal bandwidth.

2.3.4. Amplification of LED and photodiode currents

Both LED and photodiode posses a very linear relationship between current and light intensity (fig. 2.19(b) and fig. 2.22(c)). Another linear relationship - namely Ohms law $U = I \cdot R$ is utilised in order to convert voltages to currents and vice-versa which makes conversion with DACs / sampling with ADCs possible.

LED amplification

Fig. 2.23(a) shows how an operational amplifier can be used in conjunction with a transistor to effectively control the current through a sense resistor. According to Kirchhoff's Law all elements in series with this resistor will have the same current, including the emitter current of the transistor. As $I_c = {}^{\beta}/_{(\beta+1)}\, I_e$ the LED current is also defined.

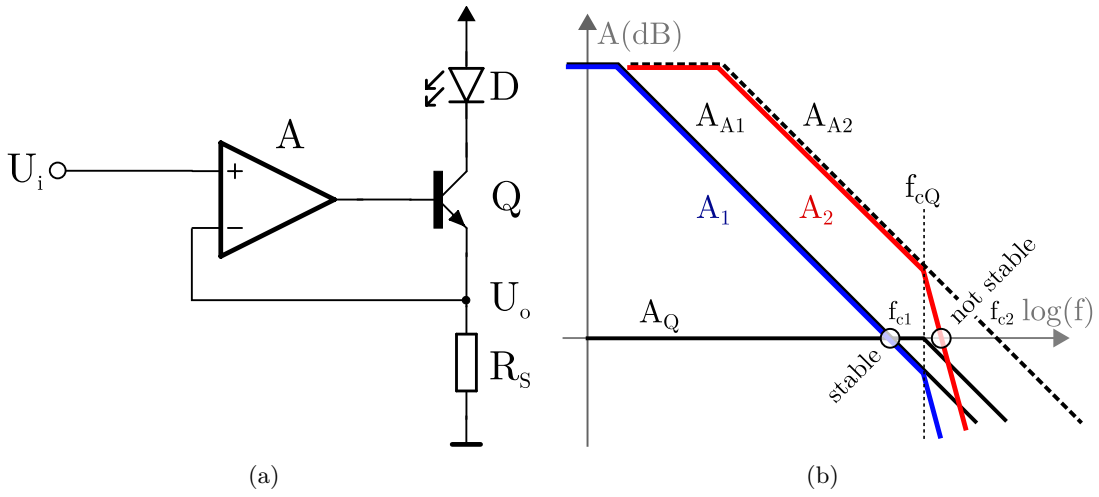

Figure 2.23.: (a) A simple voltage controlled current source with an additional power transistor. (b) The Bode plot of this circuit with two OPAs with different bandwidths (A_{A1} and A_{A2}). In one case the common transfer function with the transistor A_Q fulfils the stability criterion, in the other case a phase shift of 180 degrees occurs at the intersection point with the 0 dB line.

The transistor acts similarly as the last power stage of the OPA and establishes a high power output while reducing the output requirements of the OPA. As the transistor is also a part of the feedback loop of the amplifier the stability criterion has to be ensured. Both parts - OPA and transistor - will shift the phase with higher frequencies, therefore instabilities can occur if a phase shift of 180 degrees occurs while the open-loop gain still is higher than 1 (see fig. 2.23(b)). The design is stable as long as the second power stage (i.e. transistor) has a higher bandwidth than the first stage [26].

Photodiode amplification

The re-transformation of the photo-current into a voltage signal for sampling is done by a so called transimpedance amplifier (TIA). In most cases this is realised with an OPA (see fig. 2.24). The output voltage of this circuit can be deduced as (not considering the bandwidth limit of the amplifier):

$$V_o = I_{ph} R_f \frac{1}{1 + 1j\omega R_f C_f} \tag{2.42}$$

The reciprocal of the feedback-factor $\beta = Z1/(Z2 + Z1)$ approximately defines the closed-loop (voltage) gain of the circuit [27], with A representing the amplifier gain:

$$A_{CL} = \frac{A}{1 + \beta A} \approx \frac{1}{\beta} \quad \text{for } A \gg 1/\beta \tag{2.43}$$

Instability occurs when when $\beta A = -1$, i.e. $|A| = |1/\beta|$ with a 180 degree phase shift between A and β at the point of intercept (see fig. 2.24(b)). Without the use of the feedback capacitor C_f the factor $1/\beta$ would be $1 + j\omega C_j R_f$ (shunt resistance and input capacitance of the amplifier neglected) and this would result in a phase shift of $\approx 90\,^\circ$ at the intercept point, where in

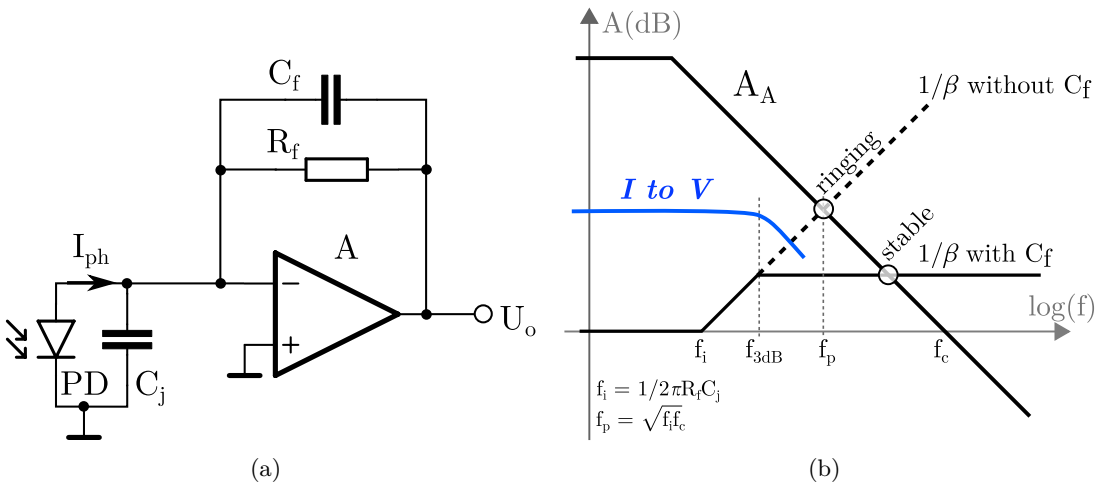

Figure 2.24.: (a) Photo-current amplification realised with a TIA. The photodiode (the junction capacitance is drawn explicitly) is part of the feedback network of the OPA. (b) The Bode plot of this TIA with and without the feedback capacitor.

most cases the amplifier gain A shows a phase shift of $\approx -90\,^\circ$ and thus this configuration would oscillate. In order to maintain a phase margin of $\approx 45\,^\circ$ a feedback capacitor can be selected according to the equation $C_f = 1/2\pi R_f f_p$ with $f_p = \sqrt{f_i f_c}$ [27].

Additionally this feedback capacitor also levels off noise voltage from the input referred voltage noise of the OPA and thus should be chosen as high as possible while still meeting the bandwidth requirements [28]. For a given 3dB bandwidth f_{3dB} the $C_f = 1/2\pi R_f f_{3dB}$. This leads to the following selection criteria for C_f:

$$\frac{1}{2\pi f_p} \leq R_f C_f \leq \frac{1}{2\pi f_{3dB}} \tag{2.44}$$

A detailed noise investigation of the TIA-circuit can be found in 3.1.6

2.4. Mixed signal processing

A big part of the processing of the luminophore emission signal and also the generation of the excitation signal is done by a digital signal processor (DSP). Key parts in the signal chain are therefore the *DAC* and *ADC* which both provide the connection from analog to digital signals. More and more signal processing can be done in the digital domain due to high performance low power consuming MCUs, ADCs and DACs, hereby making small-scale devices possible.

2.4.1. Discrete Fourier Transform

The discrete Fourier transform (DFT) is a digital processing algorithm, which is needed to explain some of the characteristics of sampling systems and is also used to determine the phase shift of the emission signal in this thesis. The DFT is the digital representation of the Fourier-transform, thus works with sampled data sets $x[n] = x(n \cdot T_s)$ where the input signal is represented as a series of uniformly (interval time T_s) sampled values.

$$X(k) = \frac{1}{N} \sum_{n=0}^{N-1} x[n] \mathrm{e}^{-\mathrm{j}\frac{2\pi k}{N} n} \tag{2.45}$$

$X(k)$ is a complex number and represents the amplitude $|X(K)|$ and phase $\angle X(K)$ of the input series at the discrete frequency bin k, which corresponds to the frequency $f = \frac{k}{N} f_s$. N represents the number of samples and thus determines the number of discrete frequency bins k and therefore the frequency resolution.

Frequencies in the input series which do not perfectly match a discrete frequency k can be expected to appear strongest in the spectrum in the nearest frequency bin. This can be seen in fig. 2.25 where the frequency response for one bin of the algorithm in eqn. 2.45 is plotted over the Nyquist-band ($0 \leq f < f_s/2$). The dashed lines represent other frequency bins and one can see that frequencies which do not fall into a specific bin appear in other bins as well, however, most determined in the closest frequency bin.

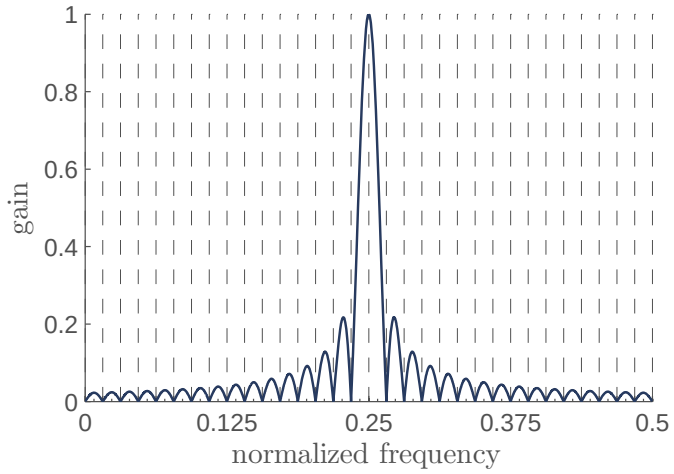

Figure 2.25.: The frequency response for a $N = 64$ points DFT algorithm evaluated at $k = 16$. Dashed lines correspond to other frequency bins in the DFT.

2.4.2. Sampled data systems

A block diagram of a sampled data system can be seen in fig. 2.26. Low-pass (or band-pass) filters at the input and output of the sampled data system prevent aliasing and remove unwanted signal components outside the band of interest. Sampling and quantization takes place with a rate f_s and a resolution of 2^N steps. To prevent aliasing the Nyquist criteria $f_a < f_s/2$ has to be ensured.

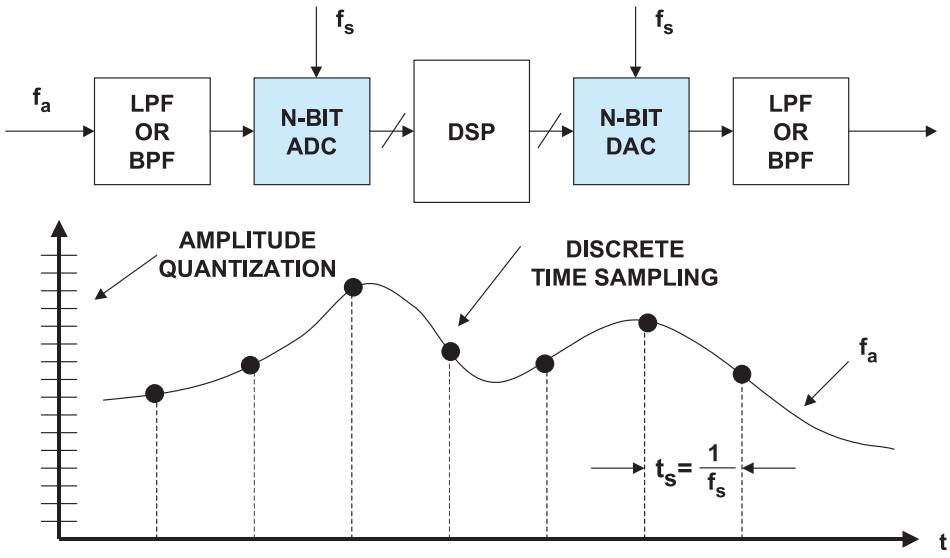

Figure 2.26.: An analog signal is continuously sampled, quantified and processed with a digital signal processor (DSP). The latter also provides the values which should be converted and generate an analog signal again. If the system should perform in real-time, every processing step has to be done in one sampling period. Picture from [18].

The performance of such mixed-signal processing systems can be characterised by a number of parameters, whereas the most obvious ones are the *resolution* of the sampling process, i.e. the number of bits (NOB), and the *sampling* or *conversion frequency* (f_s or f_c). In general resolution and sampling frequency increase the power consumption of the device.

Static parameters

Sampling systems (DACs and ADCs) can be characterised with static parameters describing their transfer function from analog to digital or vice-versa. These parameters include gain and offset error as well as integral and differential non-linearity (INL and DNL). Former are systematic linear errors which can be easily corrected and do not influence the dynamic performance of the system. DNL and INL introduce intermodulation distortions to the spectrum of the signal, depend on the signal amplitude and position and cannot be easily corrected.

2.4.3. Quantization noise

Any quantization will introduce errors to the signal, which means that the accurate analog value cannot be expressed indefinitely accurate in digital values. These errors - for an ideal N-bit converter - should not exceed $\pm 1/2\,\mathrm{LSB}$ (least significant bit). If the analog signal amplitude changes at least over a few LSBs the quantization can be expressed as noise, equally distributed over 1LSB with a variance $\sigma_q = \mathrm{LSB}^2/12$. For a sinewave and a perfect ADC the Signal-to-Quantization-Noise (SQNR) over the full Nyquist-band can be calculated as:

$$\mathrm{SQNR} = 6.02 \cdot N + 1.76\mathrm{dB} \tag{2.46}$$

If the bandwidth B is decreased (e.g. by DFT-analysis or digital filters) eqn. 2.46 changes to:

$$\mathrm{SQNR} = 6.02 \cdot N + 1.76\mathrm{dB} + 10\log\left(\frac{f_s}{2B}\right) \tag{2.47}$$

Note can be taken that the above model of quantization noise is *only* valid if there is no correlation between the quantization and the input signal, i.e. the quantization errors have to be equally distributed over $\pm 1/2\,\mathrm{LSB}$.

2.4.4. DAC dynamic performance

Regardless of the DAC converter architecture the converted analog value is most often shifted to a zero-order hold at the output, which keeps the value for one conversion time $T_c = 1/f_c$ while the DAC processes the next value. The transition speed of the DAC is limited and the time delay from a one value to a new stable value is called *settling time*. For a good performance a value independent *settling time* and low signal overshoot in between transitions is needed. This overshoot can cause *glitches* in the output, which will increase the harmonic distortion of the DAC, i.e. the spurious-free-dynamic-range (SFDR) will be decreased.

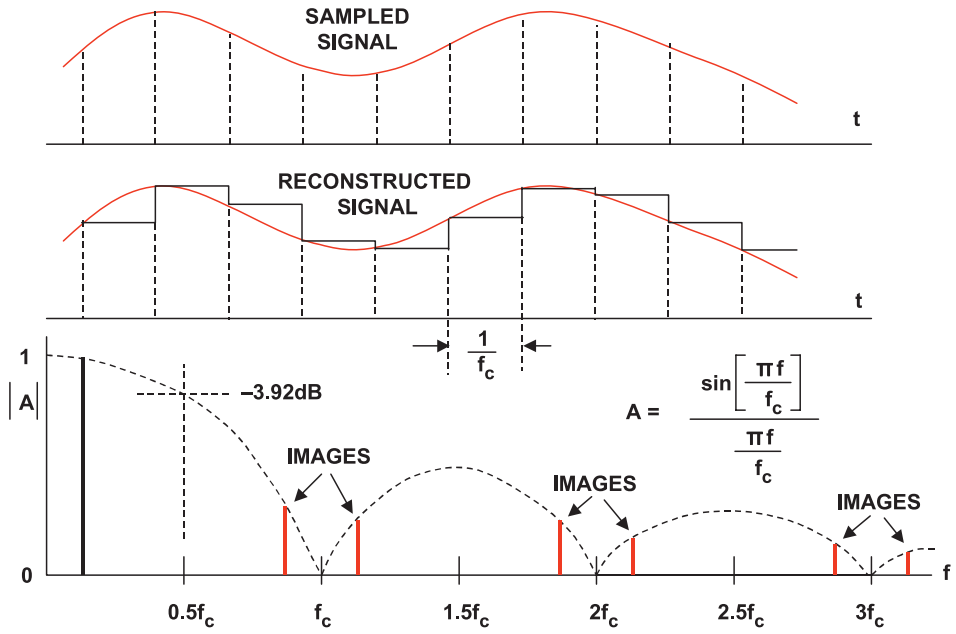

Figure 2.27.: The zero-order hold will induce aliased images of the signal into the output spectrum. Picture from [18].

The zero-order hold is not the optimal reconstruction filter for a DAC, but a very simple one. It distorts the signal and generates aliased components with a sinc $(\pi f/f_c)$ roll-off (see fig. 2.27). A low pass filter can improve the suppression of the higher frequency distortions and a higher oversampling makes the distortions smaller as they appear closer to the roll-off zeros.

The DAC introduces quantization errors as well and therefore these will also appear in the output spectrum. Dependent on the signal and if there is a correlation with quantization errors the spectrum will show harmonic distortions or an almost white noise spectrum.

2.4.5. ADC dynamic performance

The dynamic performance of ADCs is specified with parameters such as signal-to-noise ratio (SNR), signal-to-noise-and-distortion ratio (SINAD) or the effective-number-of-bits (ENOB). The SNR is specified as the ratio between the signal to the noise power, however, as sampling systems can also generate distortions in the output spectrum a better parameter to quantify the ADC performance is the SINAD which also accounts for distortions and harmonics. According to the *IEEE Std. 1241-2000* [29] the SINAD is:

$$\text{SINAD} = 10 \log \left(\frac{P_{in}}{P_{nd}} \right) \tag{2.48}$$

P_{in} represents the input signal power in the DFT bins at f_{in} and $f_s - f_{in}$. P_{nd} is the power of the residual spectrum of the DFT after the bins at $f_m = 0$ (dc) and the input frequency f_{in} and $f_s - f_{in}$ have been set to zero.

As a real ADC will generate distortions the SINAD will always be smaller then the SQNR deduced in eqn. 2.46 and one can easily see that the number-of-bits (NOB) of an ADC does not really describe its dynamic performance. The ENOB, however, accounts for the dynamic performance as it is connected with the SINAD as following:

$$\mathrm{ENOB} = \frac{\mathrm{SINAD} - 1.76\,\mathrm{dB}}{6.02} \tag{2.49}$$

The ENOB and SINAD are not static parameters of the ADC, but depend on the input signal range and frequency and will start to degrade before the input signal frequency will reach the 3 dB bandwidth of the ADC.

However the SNR of an ADC will also start to decrease with input frequency because of aperture jitter. Fig. 2.28 shows the effect of jitter of an ADC clock on the sampling result. These newly introduced errors will also decrease the ENOB. The performance will continue to suffer with higher input frequencies as the slope of the signal steepens, increasing the error introduced by the aperture jitter. The timing distribution of the jitter most often is specified with a standard deviation (e.g. σ_j or Δt_{rms}). The decrease in SNR of an ADC is also shown in eqn. 2.50 and is *independent* of the signal amplitude.

$$\mathrm{SNR} = 20\log\left(\frac{1}{2\pi f_{in}\sigma_j}\right) \tag{2.50}$$

Aperture delay, does not adversely affect the dynamic performance of the ADC, but introduces time-shifts, i.e. the sampled data looks like a time-shifted version of the input signal.

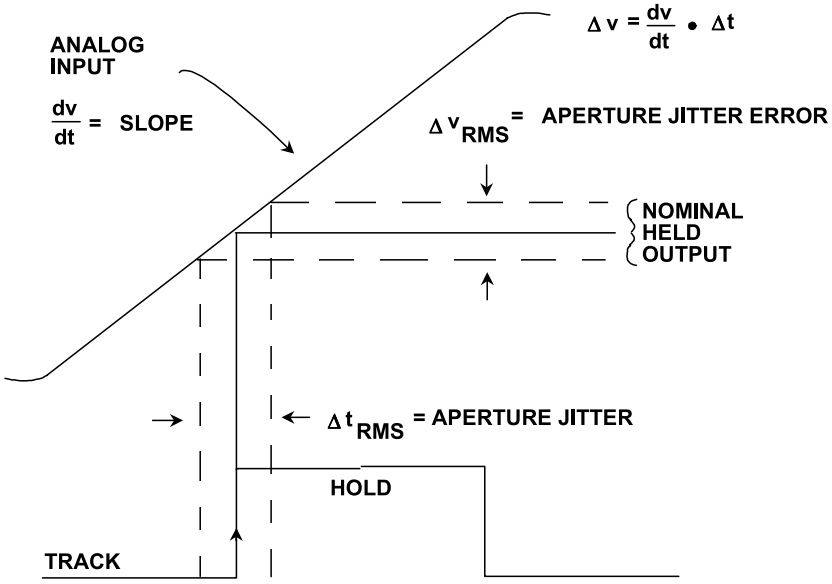

Figure 2.28.: Aperture jitter in the process of sampling. Picture from [18].

2.4.6. Coherent sampling

Signal processing systems can only work with a finite sampled data set, i.e. the number of sampling points (N) involved in processing is limited and therefore information is missing. Especially the DFT algorithm can show *leakage effects*, which can be prevented when the sampled signal period perfectly fits into the recording window. This is also true if an integral number of signal period cycles (N_C) are sampled, which exactly is done in *coherent* sampling. The condition for coherent sampling can be written down as:

$$\frac{f_{in}}{f_s} = \frac{N_C}{N} \tag{2.51}$$

Fig. 2.29 shows how the DFT algorithm would add periodic extensions to the signal if this condition of coherent sampling is not met. As a result a single frequency input signal would be smeared across the whole spectrum as shown in fig. 2.25. Therefore window functions should be used to minimise leakage and different windows will show different performances, however, leakage not only influences the amplitude, but also the phase.

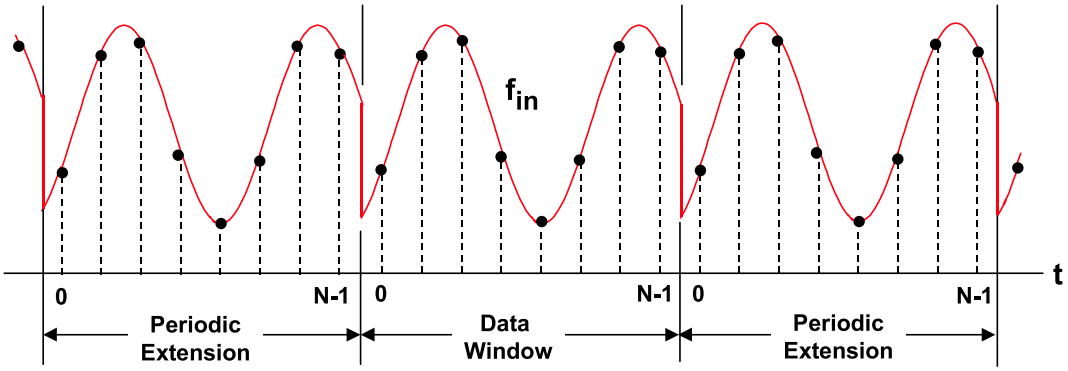

Figure 2.29.: The signal input frequency does not fit into the sampling interval and the periodic extension therefore will create artefacts in the spectrum, called leakage. Picture from [18]

3. Methods

3.1. Phase fluorometer concepts

The excitation signal a phase fluorometer generates has to undergo many different *systems* before it can be used to calculate the lifetime of a luminophore with the eqn. 2.24 derived in 2.2.2. Fig. 3.1 presents a simplified outline of the most important systems that are involved to measure the phase shift of a luminophore, which is consequently also represented as a system.

Each signal transformation step is resumed to one system, which transmits and converts the signal. The signal is converted from digital to analog by a DAC, then the excitation circuit amplifies and converts the voltage to a current, the LEDs emit light proportional to the current and further on the light is captured with a photodiode and converted back to an amplified voltage with the instrumentation circuit, where it is sampled with an ADC, which closes the loop. Each system can then be described by a transfer function (in the linear and time-invariant case) that describes the modulation of the amplitude and phase shift of the output signal with respect to the input signal. The following content in this section will describe these systems in detail.

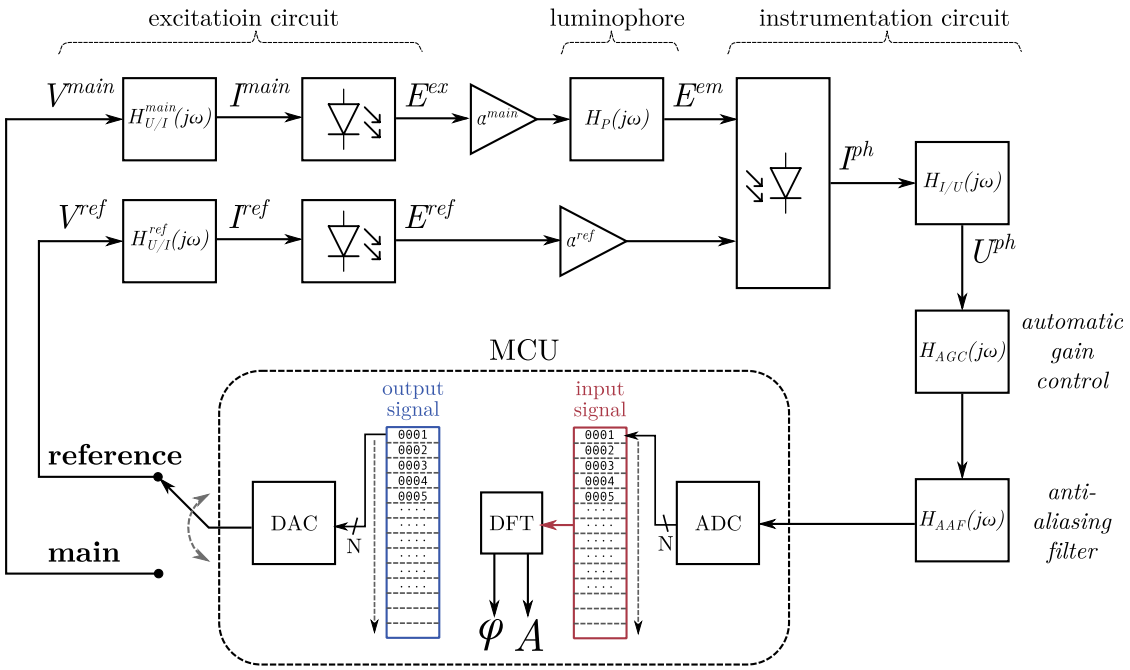

Figure 3.1.: Simplified block diagram of a phase fluorometer.

In this outline also the purpose of the reference channel used in many fluorometers nowadays [9, 4] is clearly visible. The same signal will undergo the accumulated changes of every system except for the luminophore, therefore the properties of it can be determined by the comparison of the main signal with the reference signal. In the case of sinusoids a simple subtraction of the phase shifts of both signals reveals the phase shift of the luminophore alone.

The search for improvements in each of these elements was the most time intense part of this thesis. This quest spanned from component level to system level affecting the whole device. Every part, circuit and design was newly evaluated.

3.1.1. Modular and scalable structure

In the design and especially in the layout of the precursor model several drawbacks were recognised:

- The circuit didn't allow any extensions as every part was selected and optimised for exactly four channels.
- It would be very hard to realise four identically performing channels because of the different layout for each channel.
- Any change in the placement of the channels would involve a complete layout redesign, which could badly affect the performance due to newly introduced layout flaws.

A requirement was to offer more flexibility in the amount and location of channels, therefore a new concept had to be developed to satisfy this need. It was time to think about a decentralised structure, where every channel would generate, amplify and sample the signals on its own and represent the results digitally.

All transducer components (optics, PD, LED, amplification) and a signal processor (MCU) could be efficiently integrated inside a small measurement cell (outlined in fig. 3.2(a)) which would represent one channel. Many of such cells connected to supply lines and a common data exchange bus as it is outlined in fig. 3.2(b) embody a multi-channel phase fluorometer.

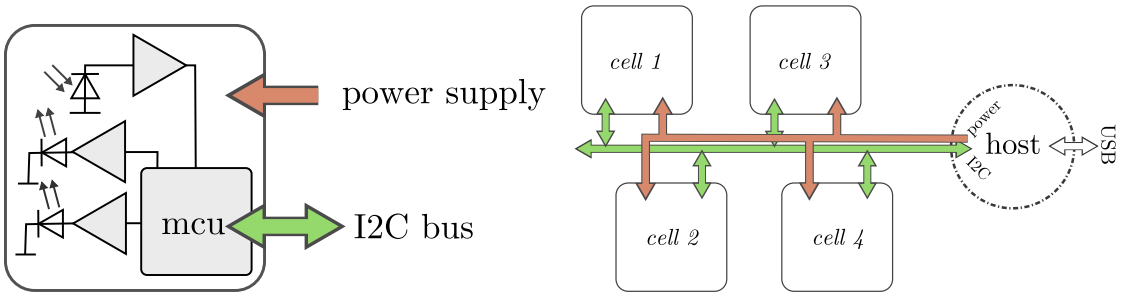

(a) (b)

Figure 3.2.: The concept of a one channel measurement cell is shown in (a) which provides the results on a I2C-bus and gets powered externally. This concept allows a scalable structure (b), thus the cells can be integrated very flexible in a complete (multi-channel) measurement device.

Hence, the expected behaviour of all channels should be quite identical and independent of the configuration or placement.

3.1.2. Optical system

Components setup

Tests with the precursor model showed that the optical alignment outlined in fig. 1.6 was not optimal to avoid stray light and crosstalk (see fig. 4.6(b) in 4.3). Furthermore the fitting of the filters in the block was very tedious and a big source for errors. In order to brightly illuminate the sensor directly above the PD a diffuse emitting LED was used, however, much light was wasted, which illuminated the sensor off-centre with respect to the PD.

The optical system was redesigned with a perpendicular alignment of the excitation and detection system and a dichroic mirror sitting in between to divide the emission and excitation light (see fig. 3.3). The alignment of emission and excitation light paths on the same optical axis should reduce light losses and improve the efficiency of the transducer. The assembly was simplified as the filters can be tucked into slits on one side of the block. In order to harness most of the emitted light (the results in 4.1 show the importance of keeping excitation light intensities low) the mirror reflects it to the PD while the LED light has to pass through it, causing $\approx 10\,\%$ light losses. The long-pass filter in front of the PD could be coated with optical oil to increase the transmittance. A thick-core light fibre (approx. 3 mm in diameter) is inserted above the mirror with a $45\,^\circ$ polished tip and glued to the mirror. This fibre guides the light and additionally focuses the emitted light onto the photodiode.

The reference LED was optically connected with a small channel and placed closer to the PD. It should be the same colour as the main LED to better compensate for temperature effects, but a much smaller LED package was selected. The identical colours made it necessary to bypass the long-pass filter, which completely covered the detector. Thus a smaller PD was placed in parallel to the main detector and exactly in front of the channel opening of the reference LED. This perpendicular design with the same colour LEDs differs from designs mentioned in literature [4].

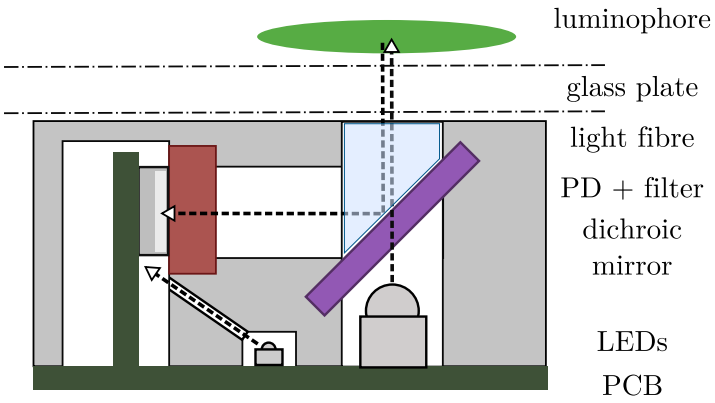

Figure 3.3.: Improvement concept for the optic system.

Component selection

In order to efficiently excite the luminophore and capture the emission light all above components have to be selected according to the luminophore spectra shown in fig. 1.3.

Main LED An amber coloured LED, which features an emission spectrum that almost perfectly matches the excitation spectrum of the luminophore and also a very high brightness (see fig. 2.19 for some typical characteristics).

Reference LED A very small amber LED which uses the same semiconductor materials.

Photodiode A standard large-area PIN photodiode. It has a good relative spectral sensitivity at the emission wavelength of the luminophore shown in fig. 2.22 was selected as detector. Additionally a small-area photodiode was used to read the reference LED.

Dichroic-mirror A 1.1 mm thick interference filter - also known as NIR-blocker - was used from *Optics Balzer AG* to reflect the emission light from the luminophore and transmit the excitation light from the LED. In fig. 2.16 the transmittance is plotted against the wavelength.

Long-pass filter A standard 3 mm thick RG9 long-pass filter was used, which effectively filtered the excitation light (see fig. 2.15) and has a very low auto-fluorescence.

Optic block The block itself was produced using a 3D-printer from *Campus02*[1] and coloured black with a graphite spray.

3.1.3. Excitation circuit

As already explained in 2.3.4 the voltage from the DAC needs to be converted to an amplified current signal. A two stage design with an OPA and an additional output buffer transistor allows to stick to standard parts and to stay flexible whilst providing a high current output. Fig. 3.4 shows the circuit in detail, which was also simulated using LTSpice® from Linear Technologies[2]. The circuit design was straightforward, however, in order to select the right parts simulation was absolutely necessary.

The specifications require to prefer OPAs with a low power consumption, a small offset voltage and low amplifier noise. Additionally an enable input for each OPA was required to select the active LED, which narrowed down the chip-select.

Care should be taken for the buffer transistors (Q1, Q2), as they are placed in the feedback loop of the OPAs (U1, U2). Many BJTs provide a high gain-bandwidth (GBW), which avoids gain-peaks as described in 2.3.4, however, most standard MOSFETs are too slow and therefore could not be used. The transfer function of the circuit with MOSFETs compared to BJTs in fig. 3.5 clearly shows the difference. Additionally the phase shifts at the modulation frequency (around 5kHz) were smaller and the BJT buffer better compensates for differences in LEDs such as diode capacitance, bulk resistance and forward voltage. In the best case the two different LED packages should make no difference in the transfer function.

[1] CAMPUS 02 Fachhochschule der Wirtschaft GmbH, A-8021 Graz, Körblergasse 126, http://www.campus02.at/

[2] Linear Technology, 1630 McCarthy Blvd. Milpitas, CA 95035-7417, http://www.linear.com/

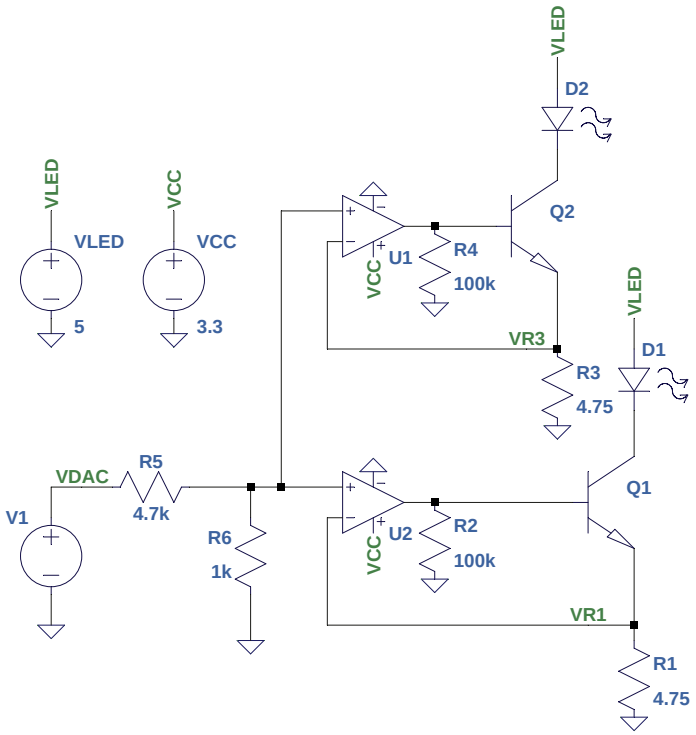

Figure 3.4.: The implemented excitation circuit for both reference and main LED.

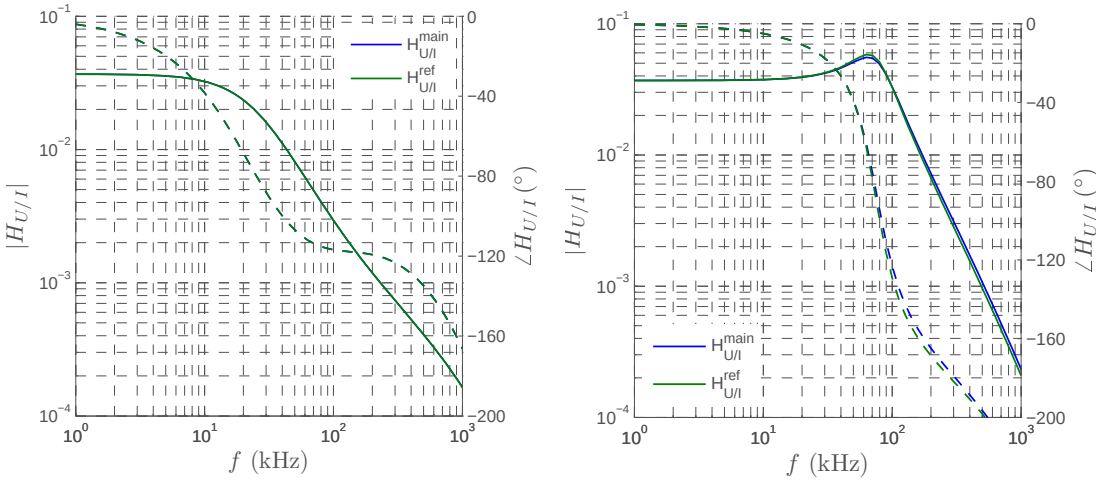

Figure 3.5.: Transfer functions of the excitation circuit for two different buffer transistors. Shown in (a) is the implemented design, whereas (b) is a mismatched design with a too slow buffer transistor.

This buffer made it possible to use a higher voltage to drive the LEDs, therefore even blue LEDs ($U_f \approx 3.2\,\mathrm{V}$) could be used, which would cause problems when using a 3.3 V supply.

3.1.4. Instrumentation circuit

The central element for the instrumentation circuit in fig. 3.6 is a standard TIA (see 2.3.4). The optimal modulation frequencies for the luminophore are rather low, so it is not needed to reverse-bias the diode, which yields a better SNR. In order to adopt to changing light situation an automatic-gain correction (AGC) was implemented able to increase the signal amplitude in low background light situations.

A second amplifier (U2) was introduced to handle the automatic gain with a variable feedback resistor (R3). This design - compared to a one stage design with AGC realised in the precursor - shows very little influence on the phase ($\leq 0.3\,°$) for different gain settings at a modulation frequency of $\approx 5\,\mathrm{kHz}$ (see fig. 3.7). Of course, a two stage design adds more noise to the system (see 3.1.6), but it relaxes the requirements for the used amplifiers, such as GBW and slew rate. This allows to use low-power OPAs with a small GBW ($< 1\,\mathrm{MHz}$), very low bias currents and small voltage and current noise.

An ambient light reduction (based on [30]) was included by using a PWM-channel of the MCU (VPWM) in combination with a low-pass filter and a high value resistor (R1) to realise a simple digital controllable current source. This correction current is subtracted from the photodiode current and can be used to cancel out ambient light, while a high amplification of the emission light is maintained. The control system for this can be implemented digitally in

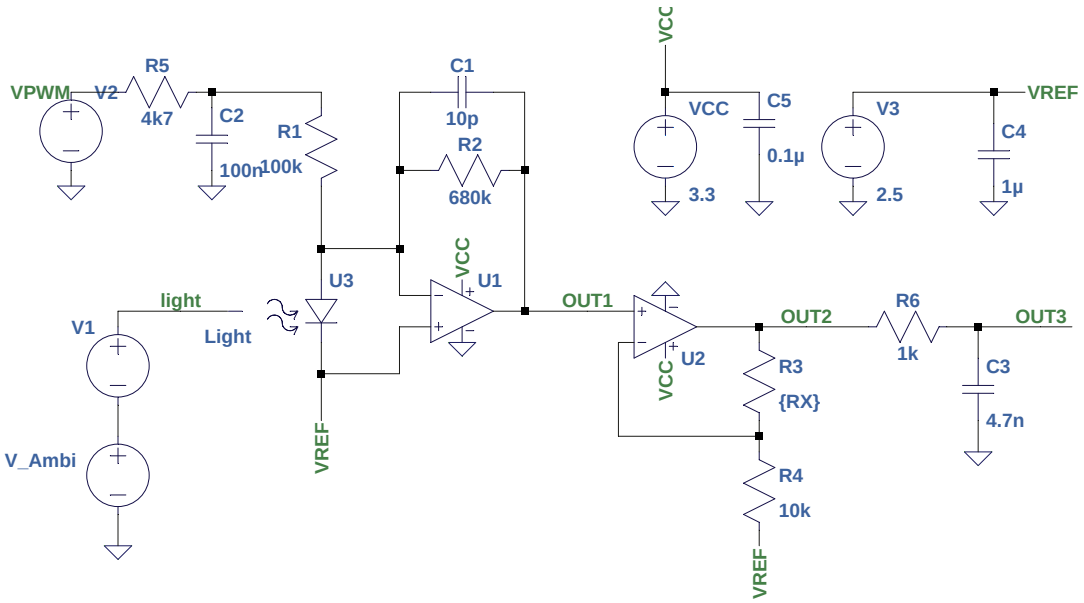

Figure 3.6.: The implemented instrumentation circuit. One can see the basic photo-diode amplification circuit added with an automatic-gain control and an ambient-light suppression feedback. The light source is modelled as a voltage source.

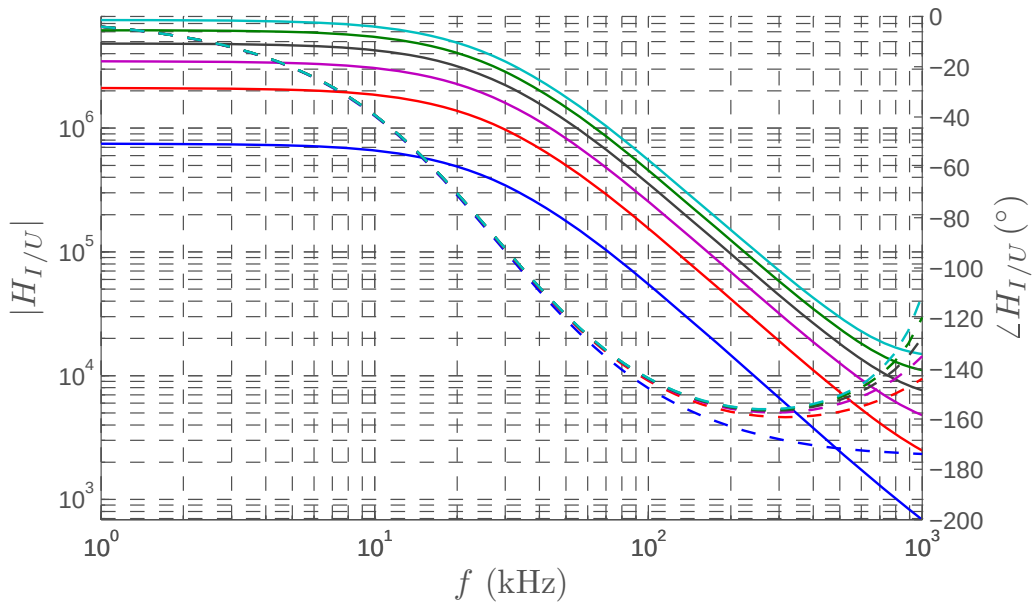

Figure 3.7.: The overall transfer function with regard to the diode current for a wide frequency range.

the MCU. However, this circuit adds more noise to the system (voltage noise of R1), therefore it can be simply left disconnected if this feature is not needed.

One can see that this analog design was optimised for small size and little phase changes at the cost of slightly more noise.

3.1.5. Signal generation and processing

The signal processing concept of many phase fluorometers is based on a lock-in amplifier, which amplifies only signals coherent to a reference signal and greatly suppresses signal components which deviate from the reference signal frequency. Many of these amplifiers solve this processing task in the analog domain and output a voltage proportional to cross-correlation of the reference with the input signal as in eqn. 3.1 [4]. If once the reference signal is selected as $v_{ref} = \sin(2\pi f_{ref} t)$ and then changed to $v_{ref} = \cos(2\pi f_{ref} t)$ the amplitude and phase of the input signal component coherent to the frequency f_{ref} can be easily calculated.

$$V_{out} \propto \int_0^{T_{per}} v_{in}(t) v_{ref}(t) dt \tag{3.1}$$

The best excitation signal frequencies for most phosphorescence lifetimes (see 2.2.3) are in the range of kHz and the ADC performance nowadays is able to sample the sensor signal with high speeds in a good resolution, therefore in this thesis the processing task can be solved digitally. The signal is generated, sampled and processed with a MCU integrated in one cell, which largely contributes to the downscale of the cell dimensions.

Digital signal generation

A DAC will output a sine wave with a fixed number of 64 points per period, thus the sampling frequency changes respectively to the excitation frequency. As seen in fig. 2.27 the DAC generates higher frequency images whereas the first component will be attenuated by the zero-order hold to $\approx 36\,\mathrm{dBc}$. Exactly this component will get aliased to the excitation frequency and therefore an additional damping of this component has to be ensured by an anti-aliasing filter.

Digital signal processing

Eqn. 3.1 implemented in the digital domain with a sine and a cosine as reference signals corresponds to the DFT algorithm and can be written as,

$$X[k] = \sum_{n=0}^{N-1} x[n] \mathrm{e}^{-\mathrm{j}\omega_k n} \quad \text{with } \omega_k = \frac{2\pi}{N} k \tag{3.2}$$

with $x[n] = v_{in}(t_n = n/f_s)$ as the sampled version of the input signal and N being the total number of points sampled with the sampling frequency f_s.

By using coherent sampling (see 2.4.6) with a signal frequency of $f_k = \omega_k/2\pi$ the $|X(k)|$ will be the amplitude and $\angle X(k)$ will be the phase of the input signal component coherent to f_k. The DFT algorithm behaves exactly as a lock-in amplifier and thus provides the same advantages: A large suppression of other frequency components and incoherent signals (e.g. noise) as more and more signal periods are sampled (known as processing gain described in 2.4).

The longer the recording time $T_s = N/f_s$, the more sampling points N of the signal have to be processed and many repeating multiplications have to be performed to get $X(k)$. This processing can be optimised to keep CPU demands low. As more full cycles N_C of the frequency period are sampled the reference signal $\mathrm{e}^{-\mathrm{j}\omega_k n}$ will periodically repeat itself after every cycle and the amount of multiplications can be significantly reduced if the calculation is reshaped as described in eqn. 3.3.

$$\begin{aligned} X(k) = \sum_{l=0}^{N_C-1} \sum_{n=0}^{M-1} x[n+lM] \mathrm{e}^{-\mathrm{j}\omega_k n} &= \sum_{n=0}^{M-1} \sum_{l=0}^{N_C-1} x[n+lM] \mathrm{e}^{-\mathrm{j}\omega_k n} \\ &= \sum_{n=0}^{M-1} \mathrm{e}^{-\mathrm{j}\omega_k n} \underbrace{\sum_{l=0}^{N_C-1} x[n+lM]}_{\hat{x}[n]} \end{aligned} \tag{3.3}$$

$\hat{x}[n]$ can be calculated by just summing up the sampled input vector $x_k[n]$ from period to period l. With this optimised method the amount of multiplications is reduced from $M \cdot N_C$ to the amount of samples per period M.

3.1.6. Noise validation

The biggest change in the new design affecting noise is the introduction of a second stage in the instrumentation circuit as AGC. The precursor model integrated this feature already in the first stage and the noise level was low enough to easily fulfil the noise specifications for different amplification settings of the AGC. Therefore it must be shown that a two stage design is able to fulfil this specifications as well.

The instrumentation circuit consists of the PD, the two amplifiers as TIA and AGC, anti-aliasing filter (AAF) and after all the ADC. Each of these parts will add noise and contribute more or less to the overall noise level.

Fig. 3.8 shows the output-referred noise with respect to the frequency of all noise sources after the amplification with the TIA. The value of the photo-current I_{ph} was assumed to produce a 0.5 V output amplitude and all other values were taken from the device datasheets. The considered noise sources are listed below, whereas other sources (such as thermal noise of the photodiode shunt resistor) could be neglected.

1. Photodiode shot-noise (see 2.3.3) $i_{np} = \sqrt{2q_e(I_d + I_{ph})}$
2. Amplifier current noise i_{na} and voltage noise e_{na}
3. Feedback resistor voltage noise $v_{nr} = \sqrt{4kTR_f}$

The output-referred noise of the TIA was calculated for each source and then geometrically added as root of the squared sums. The transfer function $H_x = 1/(1 + sC_fR_f)$ represents the low-pass filter in the feedback loop.

$$v_{np}^I = i_{np}R_fH_x \tag{3.4}$$
$$v_{na}^I = i_{na}R_fH_x + e_{na}(1 + sC_jR_fH_x) \tag{3.5}$$
$$v_{nr}^I = \sqrt{4kTR_f}H_x \tag{3.6}$$
$$v_n^I = \sqrt{{v_{np}^I}^2 + {v_{na}^I}^2 + {v_{nr}^I}^2} \tag{3.7}$$

Fig. 3.8 shows that most noise (and also the signal) rolls off because of the LPF (H_x), however, the voltage noise of the TIA first increases due to the large PD capacitance and only levels off. This means C_f limits the voltage noise and avoids large ringing (as described in 2.3.4). Without the voltage noise of the TIA a small bandwidth SNR would stay almost constant over a huge frequency range, therefore a low voltage noise is absolutely important. Note should be taken to the fact, that the current noise from the PD is current-dependent, therefore with lower signals this noise will decrease while all other sources will remain the same.

In fig. 3.9 the noise after the AAF (with unity gain of the AGC) is compared to a white quantization noise of the 12 bit ADC with ENOB = 10.5 bit and $f_s = 320$ kHz. Analog noise with frequencies $f > f_s/2$ will get aliased and increase the noise level in the Nyquist band, however the AAF greatly reduces high frequency noise power.

It can be seen that the quantization noise is the most significant noise source with a huge margin to the analog noise. An increase of the analog noise to the same level would reduce the SNR just by at maximum 3 dB. The second amplifier representing the AGC amplifies

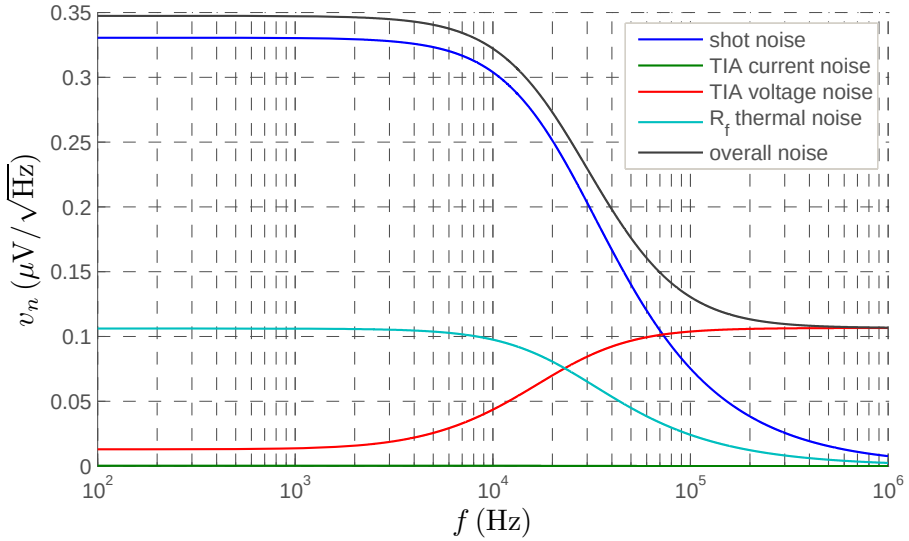

Figure 3.8.: The output-referred noise voltage densities of the TIA.

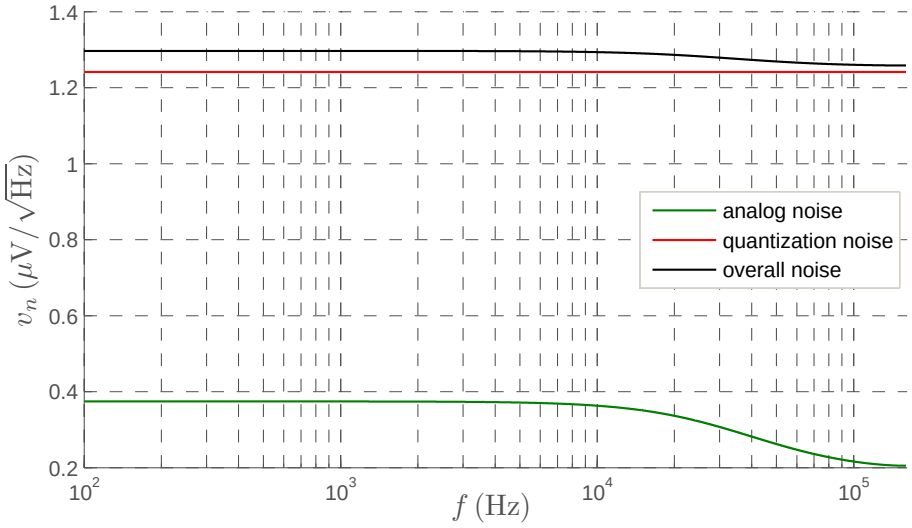

Figure 3.9.: The total analog noise voltage density after the anti-aliasing filter compared to the quantization noise modelled as white noise spread over the whole Nyquist band.

signal and noise, however, as there is a margin to the quantization noise - which will get even bigger with lower photo-currents - the amplification of the signal would outweigh the increase of noise and the SNR would become higher as if no amplification was used. So to say, the second amplifier won't improve the SNR of the analog signal, but the SQNR.

In digital processing basically a DFT algorithm is applied to the signal to determine amplitude and phase (as explained in 3.1.5). The SNR as shown in fig. 3.10 is calculated as the signal

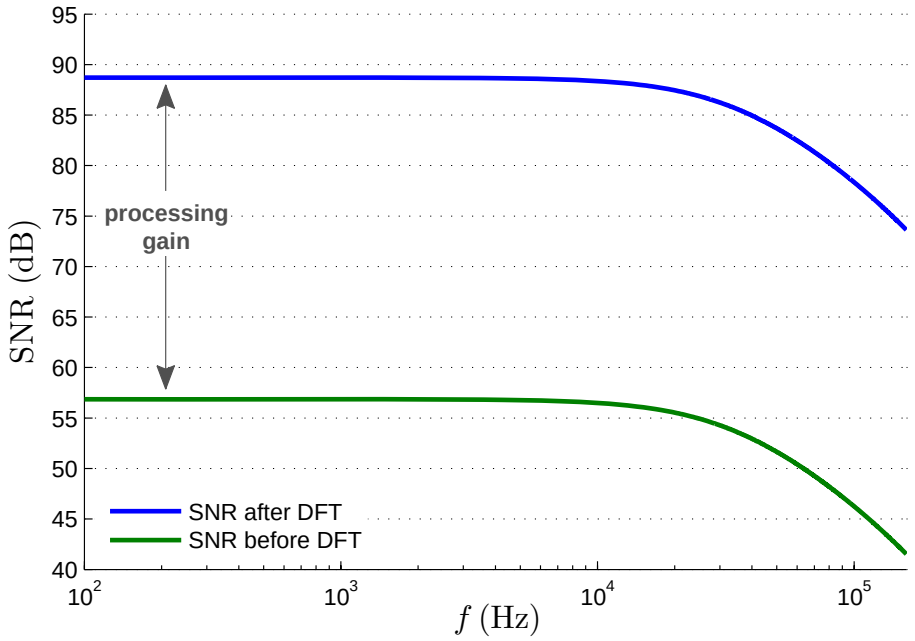

Figure 3.10.: SNR with $M = f_s T_s = 3200$ (i.e. 10 ms recording time and 320 kHz sampling frequency). The ideal processing gain would be approx. 32 dB.

power and the noise power within one frequency bin of the DFT with M being the number of bins. As coherent sampling is used half of the signal power can be found in exactly one bin, however, noise spreads over the whole Nyquist band and in the case of white noise is just $1/M$ of the noise power.

$$SNR = 10 \log \left(\frac{P_s/2}{P_n/M} \right) = 10 \log \frac{P_s}{P_n} + \underbrace{10 \log \frac{M}{2}}_{\text{processing gain}} \tag{3.8}$$

The DFT algorithm achieves better processing gain and a better SNR with longer sampling times, however, just by $\log \frac{M}{2}$ therefore a 2 times longer sampling improves the SNR just by 3 dB.

In order to validate the performance of this two stage design with AGC it was compared to the one stage design with and without AGC (see fig. 3.11). The SNR was calculated for decreasing photo-current values, where in the cases with AGC the gain was chosen to maintain a signal amplitude at the ADC of 0.5 V. The figure clearly shows the advantages of AGC and that in this case the two stage design is able to keep the SNR high as well.

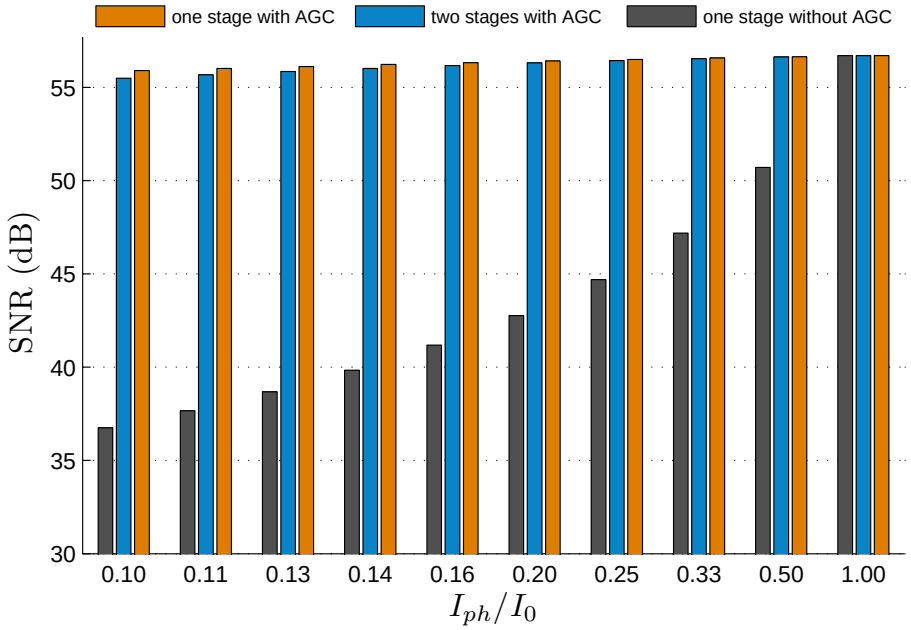

Figure 3.11.: SNR comparison of different amplification designs: A one stage TIA design with AGC and two stage design with AGC compared to a TIA without AGC.

3.2. Assessment of phase errors

Crosstalk (XT), noise and temperature affect amplitude and phase of the measured signal in different ways. This section focuses on the description of how the phase of a signal can be changed by different jamming sources.

3.2.1. Effects of Crosstalk

Crosstalk occurs optically, where excitation light hits the photodiode, and electrically from the excitation to the instrumentation circuit either capacitively, resistively or inductively. Optical crosstalk cannot affect the reference measurements where the excitation light is the signal to measure. It is crucial to keep crosstalk as small as possible, as it will affect the amplitude and the phase angle.

By representing sinusoidal signals as a vector in the complex plane as in fig. 3.12 it can be easily understood how crosstalk can alter the phase. Depending on the relative phase shift between crosstalk and the original signal the phase will be more or less affected, which can be calculated as [31]:

$$\tan(\Delta\phi_m) = \frac{v_{XT}^{\perp}}{v_s + v_{XT}^{\parallel}} \tag{3.9}$$

The symbols $\perp$ and $\parallel$ comply with perpendicular and parallel components with respect to the emission signal. When $v_{\vec{XT}}$ is perpendicular to the measured signal $v_{\vec{m}}$ the change in phase

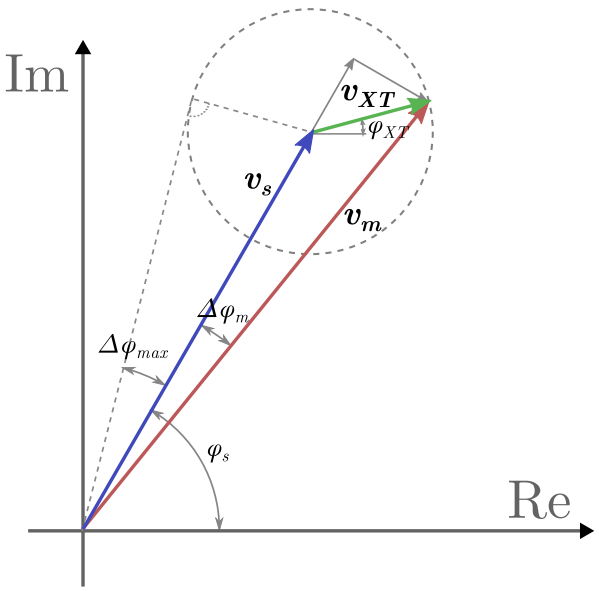

Figure 3.12.: The clean signal $\vec{v_s}$ and the crosstalk $v_{\vec{XT}}$ add up vectorial to the measured signal $\vec{v_m}$. Depending on the relative phase shift of crosstalk with respect to the signal the measured signal phase angle more or less deviates from the original signal.

is a maximum. By introducing a crosstalk factor $k_{XT} = v_{XT}/v_s$ and assuming small phase shifts ($\tan(\Delta\phi_m) \approx \Delta\phi_m$) the above equation can be simplified to:

$$\Delta\phi_m \approx \frac{k_{XT}\sin(\phi_s - \phi_{XT})}{1 + k_{XT}\cos(\phi_s - \phi_{XT})} \approx k_{XT}\sin(\phi_s - \phi_{XT}) \tag{3.10}$$

This means a crosstalk of 1 % can change the phase in the worst case by approximately 0.57 °.

3.2.2. Phase noise

Similarly noise can be seen as a vector with a Gaussian distributed amplitude with a variance σ_n^2, composed of a parallel and perpendicular component with respect to the original signal. It then can be shown that noise effectively disturbs the phase and the phase variance can be expressed as in eqn. 3.11 [32] when a rather high SNR can be assumed:

$$\sigma_\phi^2 \approx \frac{\sigma_n^2}{2v_s^2} \quad \Rightarrow \quad \sigma_\phi \approx \frac{1}{\sqrt{2}}\,10^{-\mathrm{SNR}/20} \tag{3.11}$$

This results in $\approx 0.04\,^\circ$ standard deviation of phase noise if an SNR of 60 dB is assumed. If $\sigma_\phi \leq 1/100\,^\circ$ is required the SNR has to be kept higher than 73 dB. As described in 3.1.6 the processing gain of the DFT algorithm can reduce noise power.

If coherent sampling is used, however, quantization errors do not add up to a white-noise spectrum but introduce harmonic distortions [18, p. 2.17]. Quantization of a clean sinusoid and coherent input signal does not result in any phase noise and does not affect the SNR of

this frequency bin at all. Overlaying this signal with noise will reduce the correlation with the sampling and is known as *dithering*. With enough dithering quantization can be modelled similarly to fig. 3.12 as white noise and will cause phase noise σ_ϕ being inversely proportional to the signal amplitude [33].

Aperture jitter also affects amplitude *and* phase noise. The phase noise term for jitter is independent of the signal amplitude [34] and can be estimated as,

$$\sigma_\phi^2 \approx \frac{(2\pi f_{in})^2 \sigma_j^2}{N} \tag{3.12}$$

where σ_j^2 represents the variance of the timing jitter and N is the number of samples used for the DFT.

To study the effects of sampling on the phase the sinusoidal input signal with overlaid white noise from the instrumentation circuit was modelled to be sampled by an ADC with ENOB = 10, which introduces quantization errors and aperture jitter. The spectrum of this simulation can be seen in fig. 3.13 and confirms that the assumption of an almost white quantization noise is not valid for coherent sampled signals. Although the input signal gets *dithered* quantization still generates harmonic distortions (one can see the 3$^{\text{rd}}$ and 7$^{\text{th}}$ harmonic).

The resulting phase noise distribution of this simulation can be seen in fig. 3.14. The amplification keeps the input signal at $\approx 0.5\,\text{V}$ while light intensity is reduced. A six times higher light intensity (at A=1) just slightly improves the phase noise due to the always constant aperture jitter combined with quantization errors. The simulation shows that the standard deviation of the phase due to quantization of the ADC is much lower as it would be expected from eqn. 3.11 for white quantization noise.

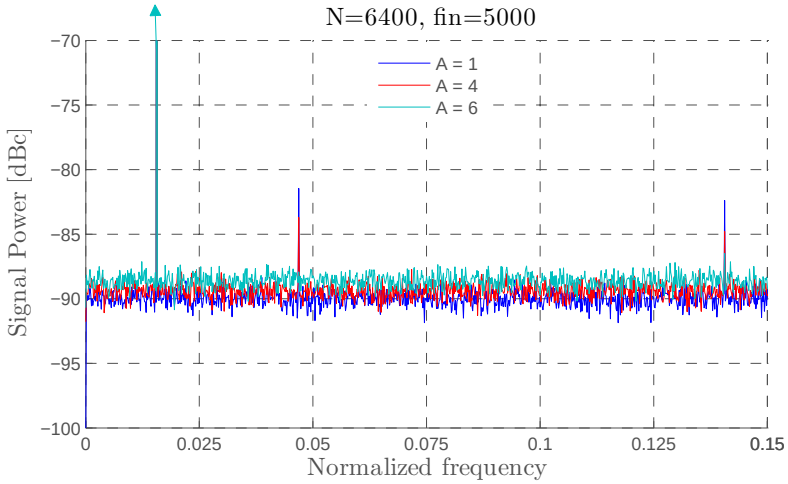

Figure 3.13.: The spectrum of a coherent sampled sinusoid with $f_s = 320\,\text{kHz}$ and $ENOB \approx 10$ and different amplification settings (A) of the last stage. An aperture jitter with $\sigma_j = 1/32\,\mu\text{s}$ was assumed.

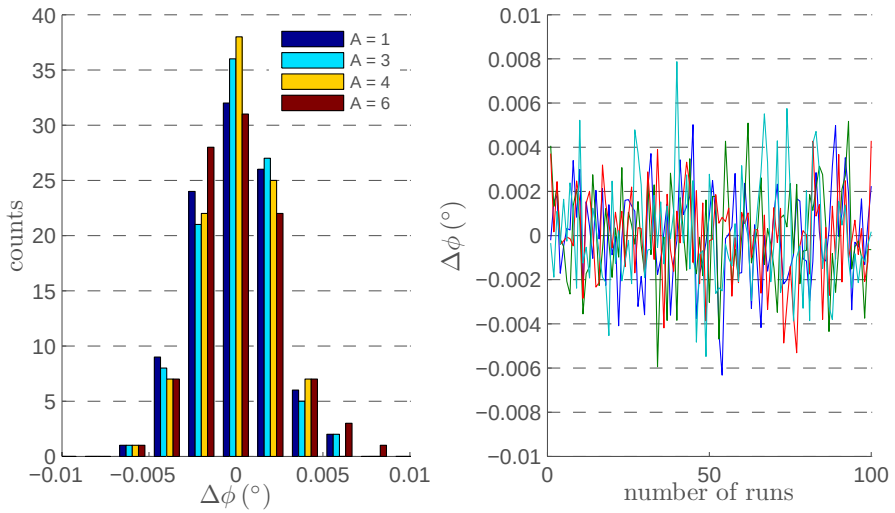

Figure 3.14.: The simulation results for the phase noise distribution with different amplification settings after 100 measurement runs.

3.2.3. The influence of varying temperature

Although a reference is used which eliminates almost all electronic phase shifts, there are still degrees of freedom: The two different LEDs could cause problems and different amplification setting. Therefore, the excitation circuit was optimised for stability (as described in 3.1.3) and LEDs with the same material were used. Attention was paid to use parts with a small temperature coefficient in the crucial phase shifting components of the instrumentation circuit. The two stage design with almost no phase changes when switching the amplification (see fig. 3.7) can also help to reduce the temperature impact. As the maximum phase change over the whole amplification range at the measurement frequency is expected to be within 0.3 ° and the absolute phase is around $\phi_{abs} = 20\,°$ a maximum phase error can be estimated, if the whole instrumentation circuit is simplified to a low-pass consisting of one lumped temperature dependent resistor R_l and capacitor C_l,

$$R_l C_l = \frac{\tan \phi_{abs}}{2\pi f} \tag{3.13}$$

The temperature induced phase change can then be calculated as:

$$\Delta\phi(\phi_{abs}, \Delta T) = \phi_{abs} - \arctan(2\pi f R_l(\Delta T) C_l(\Delta T))) \tag{3.14}$$

Assuming arbitrary temperature coefficients of 25 ppm and 30 ppm for $R_l(\Delta T)$ and $C_l(\Delta T)$ the phase error $\Delta\phi(20\,°, 60\,\mathrm{K}) - \Delta\phi(20.3\,°, 60\,\mathrm{K})$ for different amplifications due to a temperature change of 60 K would be roughly 1/1000 °. The precursor model (compare with the results in fig. 4.9(b)) shows very different phases for various amplification settings, e.g. 53 ° and 68 °: This would result in −25/1000 ° phase error due to the same change in temperature.

3.3. Modelling luminescence

The model used for luminescence in the previous chapter 2.1 is straight forward and abstracts the behaviour of the luminophore to be strictly linear. However, during tests of sensors often phase shifts with increasing excitation light intensity could be noticed. It was worth taking a closer look onto the luminophore to investigate its behaviour including high light intensity conditions.

3.3.1. State diagram and equations

In this model the luminophore can be in 3 different states: The ground state (S_0), the excited state (S_1) and the triplet state (T_1). The transitions from one state to the other take place with the corresponding reaction rates (see Fig. 3.15). If there is a quencher present in the system it can induce a transition from T_1 to S_0 of the luminophore by transferring energy to the quencher, which gets promoted to the excited state. As in all our experiments the quencher is oxygen, the label for the lowest energy state of the quencher is T_1 and the excited state is labelled S_1.

The reaction rates for transitions from a higher to a lower energy state are assumed to be only material dependent. Radiative transitions from S_1 to S_0 are neglected as well as further excitation transitions from any higher energy levels when populated (e.g. triplet-triplet excitations starting at T_1). Also stimulated emission is neglected, as the population of S_1 is very low so the probability for it is very small. The probability for the transition from S_0 to S_1 is, dependent on the light intensity and the properties of the sensor.

In a very thin slice of the sensor material perpendicular to the incident light the light intensity can be considered as constant and also every luminophore can be considered to have the same expected value $E(\eta_{ex})$ to get excited by photons as there are no luminophores overlapping each other as outlined in fig. 3.16. The efficiency with which molecules in the ground state getting excited by a photon was derived with the Beer-Lambert law in eqn. 2.4 and it increases

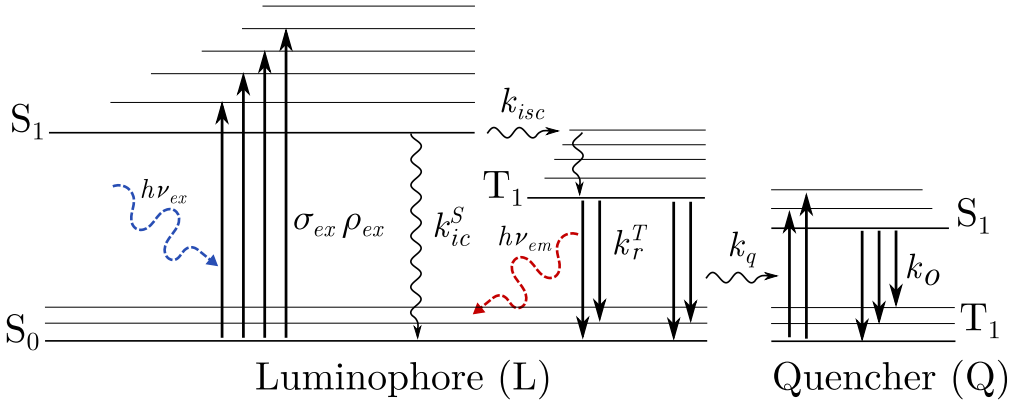

Figure 3.15.: Simplified Jablonski-diagram of a luminophore with phosphorescence as signal parameter and oxygen as quencher. Fluorescence as well as non-radiative decay from the T_1-state was neglected.

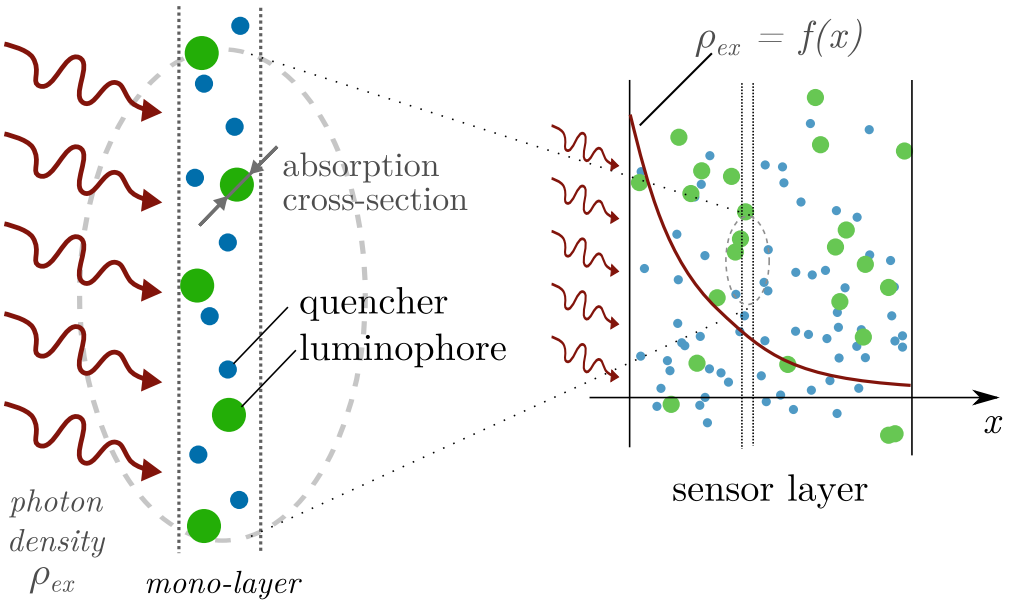

Figure 3.16.: Excitation of the luminophore in a mono-layer matrix.

with time. Thus the rate of transitions from S_0 to S_1 in one mono-layer can be described as this number over time. In the following equations ρ_{ex} is the photon density over time of the excitation light and σ_{ex} is the absorption cross-section at the excitation wavelength.

A real sensor consists of many mono-layers with different light intensities, and each mono-layer absorbs photons consecutively. This is very complex to model and additionally there is a lack of certainty in parameters, e.g. which layer couples how much light back into the optical system, thus the model only accounts for the first mono-layer with the highest light intensity. The concentration of molecules in every state can then be calculated with differential state equations with L as state variables for the concentration of luminophores and Q for quenchers. These equations do not consider any boundary conditions (e.g. diffusion) for the before mentioned reasons.

$$\frac{dL_{S1}}{dt} = \sigma_{ex}\rho_{ex}L_{S0} - (k_{isc} + k_{ic}^{S})L_{S1} \tag{3.15}$$

$$\frac{dL_{T1}}{dt} = k_{isc}L_{S1} - (k_r^T + k_q Q_{T1})L_{T1} \tag{3.16}$$

$$\frac{dQ_{S1}}{dt} = k_q Q_{T1} L_{T1} - k_o Q_{S1} \tag{3.17}$$

Of course all those processes cannot change the overall amount (or concentration) of molecules, so a dependency between these state variables has to be introduced, where L_0 and Q_0 represent the overall concentration:

$$L_0 = L_{S0} + L_{S1} + L_{T1} \tag{3.18}$$

$$Q_0 = Q_{T1} + Q_{S1} \tag{3.19}$$

These conditions mutually relate the above state equations and an analytical solution could not be found, esp. for arbitrary input functions (light intensity). However, the kinetics of the state variables can be discussed and approximated numerically with simulations.

3.3.2. System behaviour

The steady states of the system variables could be derived rather easily, however, the system kinetics could only be solved with many simplifications. Furthermore the limits for the usage of the simple linear model from 2.1 are shown.

S1-state of the luminophores

All reaction rate constants (k_{isc} and k_{ic}^{S}) for the S_1-state (eqn. 3.15) are by decades higher than others, thus the equilibrium point of the S_1-state is reached very fast and for the numerical solution of the above state equations no difference could be noticed if the kinetics of this state variable were neglected. The steady-state value for L_{S1} for a time-constant light intensity can be seen in eqn. 3.20:

$$\overline{L_{S1}} = \frac{\sigma_{ex}\rho_{ex}}{k_{ISC} + k_{ic} + \sigma_{ex}\rho_{ex}}(L_0 - L_{T1}) \tag{3.20}$$

Kinetics for the T1-state of the luminophore

The state equation for the T_1-state (eqn. 3.16) was solved taking many assumptions in order to simplify the system.

- light intensity is constant over time
- L_{S1} is in the steady state
- $Q_{T1} \equiv Q_0$, thus no cross-dependency of L_{T1}
- $L_{T1}(t = 0) = 0$

$$\begin{aligned} \frac{dL_{T1}}{dt} &= k_{ISC}\overline{L_{S1}} - (k_r^T + k_q Q_0)L_{T1} \\ \Rightarrow \quad \overline{L_{T1}} &= \frac{1}{1 + \underbrace{\frac{k_{isc} + k_{ic} + \sigma_{ex}\rho_{ex}}{k_{isc}}}_{\approx 1/\Phi_0} \frac{kqQ_0 + k_r^T}{\sigma_{ex}\rho_{ex}}} L_0 \qquad (3.21) \\ \Rightarrow \quad L_{T1}(t) &= \overline{L_{T1}}\left(1 - \mathrm{e}^{-(\Phi_0\sigma_{ex}\rho_{ex} + k_q Q_0 + k_r^T)t}\right) \qquad (3.22) \end{aligned}$$

In the last equation the light intensity is part of the time constant. Thus, when working with high light intensities the time constant can be significantly shorter (see fig.3.17). The dependency of the rising edge on light intensity can be clearly seen, whereas the falling edge is

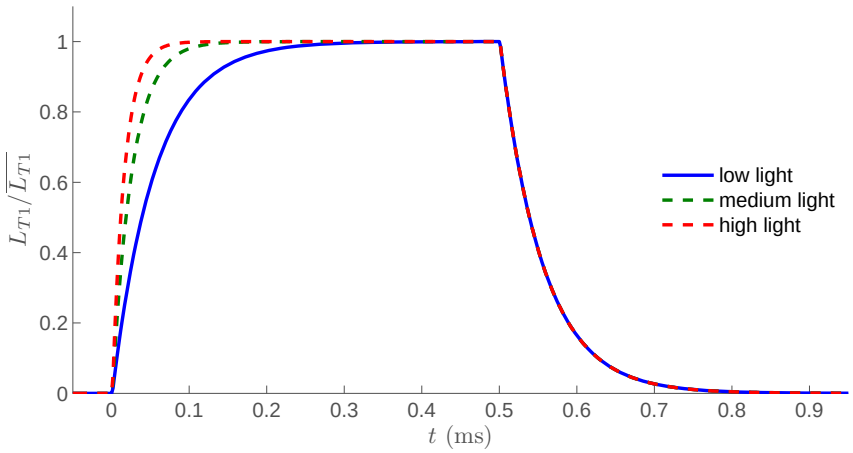

Figure 3.17.: The kinetics of luminophores in the T_1-state when hit by a square light impulse with different intensities and no quenching.

always only dependent on the luminophore itself. The amount of luminophores in the excited state in fractions of the overall amount is listed in the graph. In order to avoid this effect the light intensity must be kept small enough.

$$\rho_{ex} \lll \frac{1}{\sigma_{ex}} \frac{1}{\Phi_0} (k_q Q_0 + k_r^T) \tag{3.23}$$

If this condition is fulfilled then also the steady state value of L_{T1} is very small and only linearly dependent on the light intensity.

Kinetics for the S1-state of the quencher

Similarly the state equation for the quencher (eqn. 3.17) can be solved by taking assumptions to greatly simplify the system.

- light intensity is constant over time
- L_{T1} is in a steady state and marked as $\overline{L_{T1}}$
- $Q_{S1}(t=0) = 0$

$$\begin{aligned} \frac{dQ_{S1}}{dt} &= k_q \overline{L_{T1}} Q_0 - (k_o + k_q \overline{L_{T1}}) Q_{S1} \\ \Rightarrow \quad \overline{Q_{S1}} &= \frac{k_q \overline{L_{T1}}}{k_q \overline{L_{T1}} + k_o} Q_0 \qquad (3.24) \\ \Rightarrow \quad Q_{S1}(t) &= \overline{Q_{S1}} \left(1 - \mathrm{e}^{-(k_q \overline{L_{T1}} + k_o)t}\right) \qquad (3.25) \end{aligned}$$

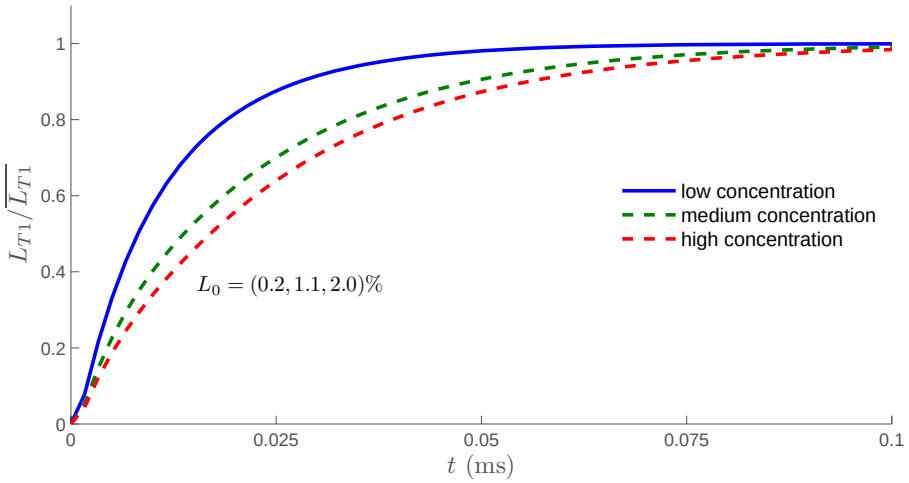

(a)

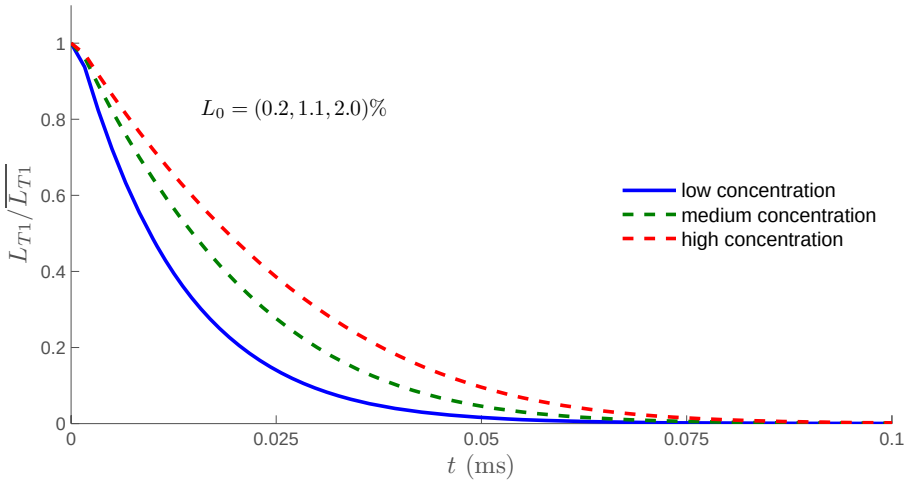

(b)

Figure 3.18.: The kinetics of the luminophores in the T_1-state affect by the quencher. The graph in (a) shows the rising and (b) the falling edge when hitting the mono-layer with a square light pulse.

The concentration of luminophores in the T_1-state modifies the quencher kinetics (see fig. 3.18). Higher luminophore concentrations excite more quencher, less quenchers are available in the ground state and therefore the rise time gets longer with higher luminophore concentrations. Similarly the decay time is affected by this process. If the concentration of L_{T1} is small enough the steady-state concentration of quencher is $\lll Q_0$ and depends linearly on L_{T1}.

$$\overline{L_{T1}} \lll \frac{k_o}{k_q} \tag{3.26}$$

3.3.3. Phase affects

The kinetics show that in certain conditions the system is very non-linear and therefore the simple model (see eqn. 2.13) is not valid any more. If the luminophore gets excited with a sinusoidal wave, the emission light - which is just a fraction of the luminophore concentration in the T_1-state - would be a distorted sine due to this non-linearities (see fig. 3.19). One can take note, that the depopulation of the luminophore induces negative phase shifts, whereas depopulation of the quenchers induces positive phase shits.

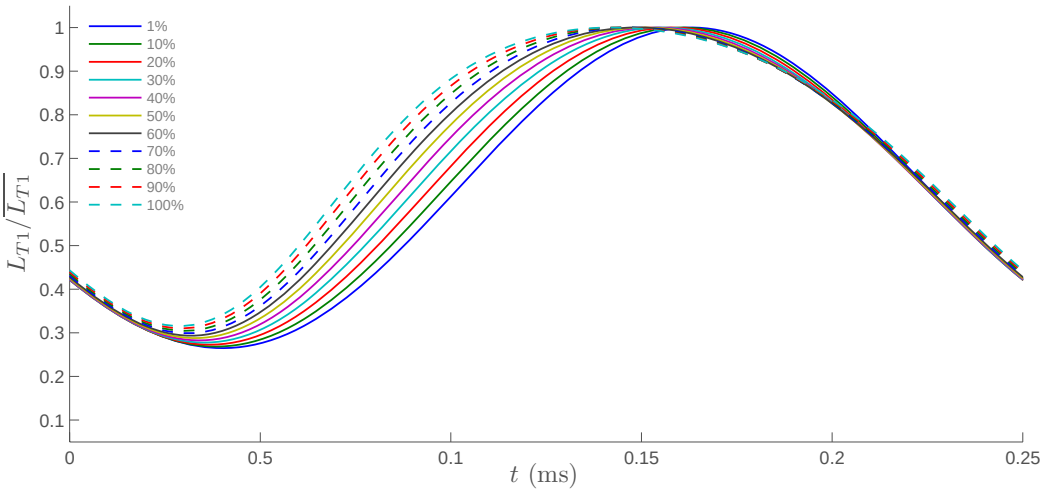

(a)

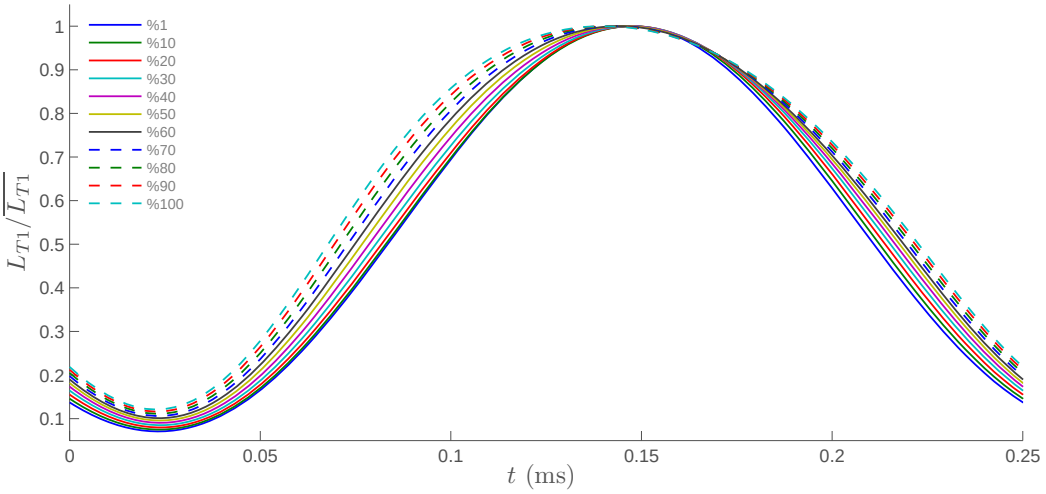

(b)

Figure 3.19.: (a) Distortion of the emission light of the luminophore when excited with a sinusoidal light just because of increasing light intensities. (b) The emission light of the same luminophore with taking also quenching into account.

3.4. Construction of the phase measurement cell

The mentioned concepts in 3.1 were implemented in the design of a small-scaled one-channel phase fluorometer, which can be seen in fig. 3.20. The overall size this measurement cell is $25 \times 25 \times 15\,\text{mm}$, which includes all optical and electronic components for a complete phase fluorometer, just a stable supply voltage has to be provided externally.

Fig. 3.20(a) shows the perpendicular alignment of the photodiodes with respect to the excitation and reference LED. The MCU sits on the bottom of the PCB, manages the whole measurement process and communicates via an I2C-bus. The connector contains all supply, communication and programming pins for the measurement cell.

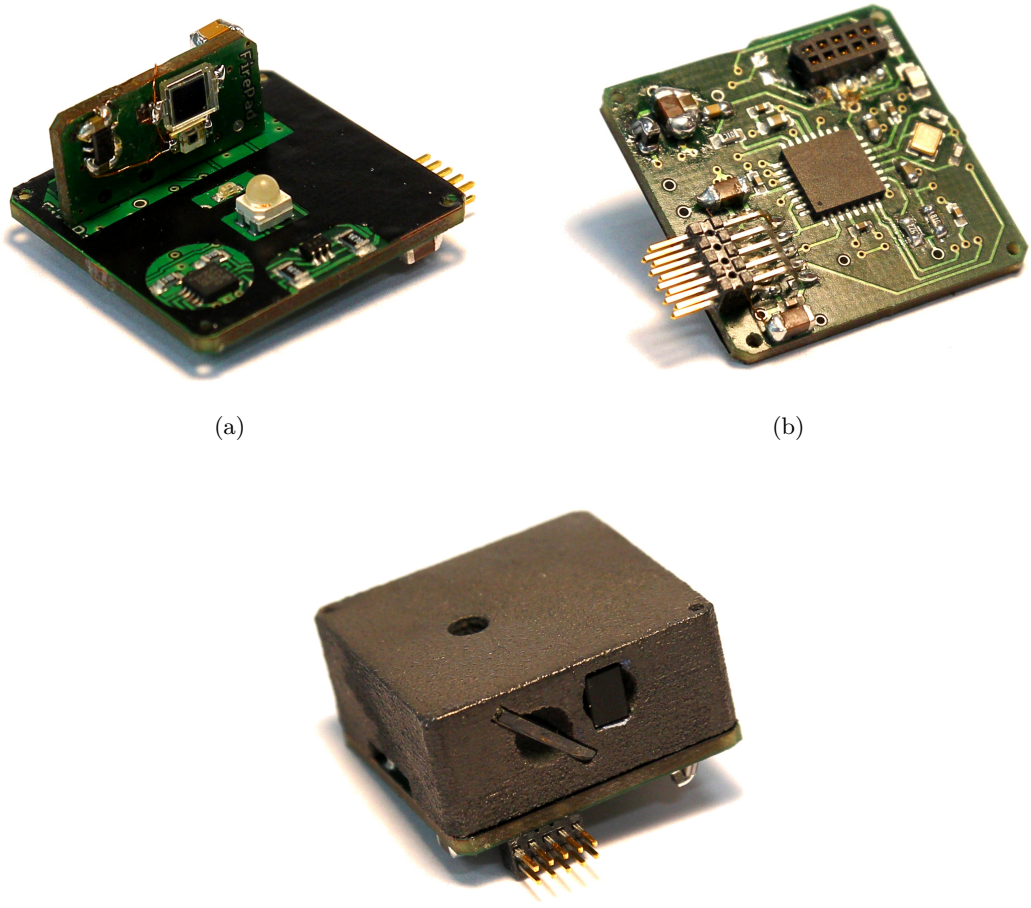

(a) (b)

(c)

Figure 3.20.: A top (a) and bottom (b) view of the final prototype design for a one channel measurement cell which is able to determine phase shifts of luminescence emission light with a high resolution. In (c) a complete phase measurement cell with the optic block including a dichroic mirror and a long-pass filter is shown.

The phase fluorometer is completed with the dichroic mirror and a long-pass filter placed in a optic block (see fig. 3.20(c)), which was coloured black to ensure low auto-fluorescence and a good suppression of unwanted stray light. A black foil was fixed on the top side of the PCB to further absorb stray light. The hole on top contains a light fibre and marks the read-out spot for sensors, where the excitation light exits the cell and also the emission light is captured.

3.4.1. Schematic and Layout

The principles of the circuits are explained in detail in 3.1.3 and 3.1.4. The photodiodes with the TIA are placed on an own PCB, which is joined and kept in place with a connector perpendicular to the rest of the layout. The TIA was placed as close to the photodiodes as possible to avoid leakage currents, which could couple into the high-ohmic trace connecting the photodiodes with the amplifier. Additionally the photodiodes were shielded with the cathode potential.

Care was taken to keep the excitation circuit separated from the instrumentation circuit and also to keep digital parts away from the photodiode (e.g. MCU, digital resistor, etc.). The excitation circuit was placed on the top side of the PCB keeping the traces which conduct high LED currents as short as possible.

The chosen MCU, placed on the bottom side of the PCB is one of the most energy-saving MCUs on the market and could exactly provide the computational power needed for conversion, sampling and processing of the signals. In order to achieve accurate sampling an external 32MHz crystal was selected as clock source, which should be much more precise than the internal RC-clock of the MCU. A simple first order low-pass filter (cut-off at about 2kHz) decouples analog and digital supply lines. Furthermore the supply lines for the LEDs were routed completely separated from other supplies to avoid ohmic offset voltages generated by high currents in the analog power supply.

All PCBs were routed on 4-layer PCBs, sticking to design guidelines from [18, p 10.15]. The inside layers (2,3) were explicitly used as grounding and power supply planes to firstly provide every signal current a short return path and secondly effectively shield bottom traces from top traces to prevent coupling. A common ground for digital and analog supply was used to prevent routing of traces over gaps and reduce coupling of digital ground noise into the analog ground of the MCU. However, extra care has then be taken to locally separate digital parts from analog ones.

One simple connector can be used to run and program the measurement cell. The default communication pathway is an I2C-bus, however, the cell could be configured to directly communicate to another UART-device. A major advantage of this modular concept is that the layout can be optimised for a single cell and a multi-channel phase fluorometer can be assembled with many of these cells. This makes it almost impossible to introduce new layout mistakes when a device with a different number or orientation of channels should be designed.

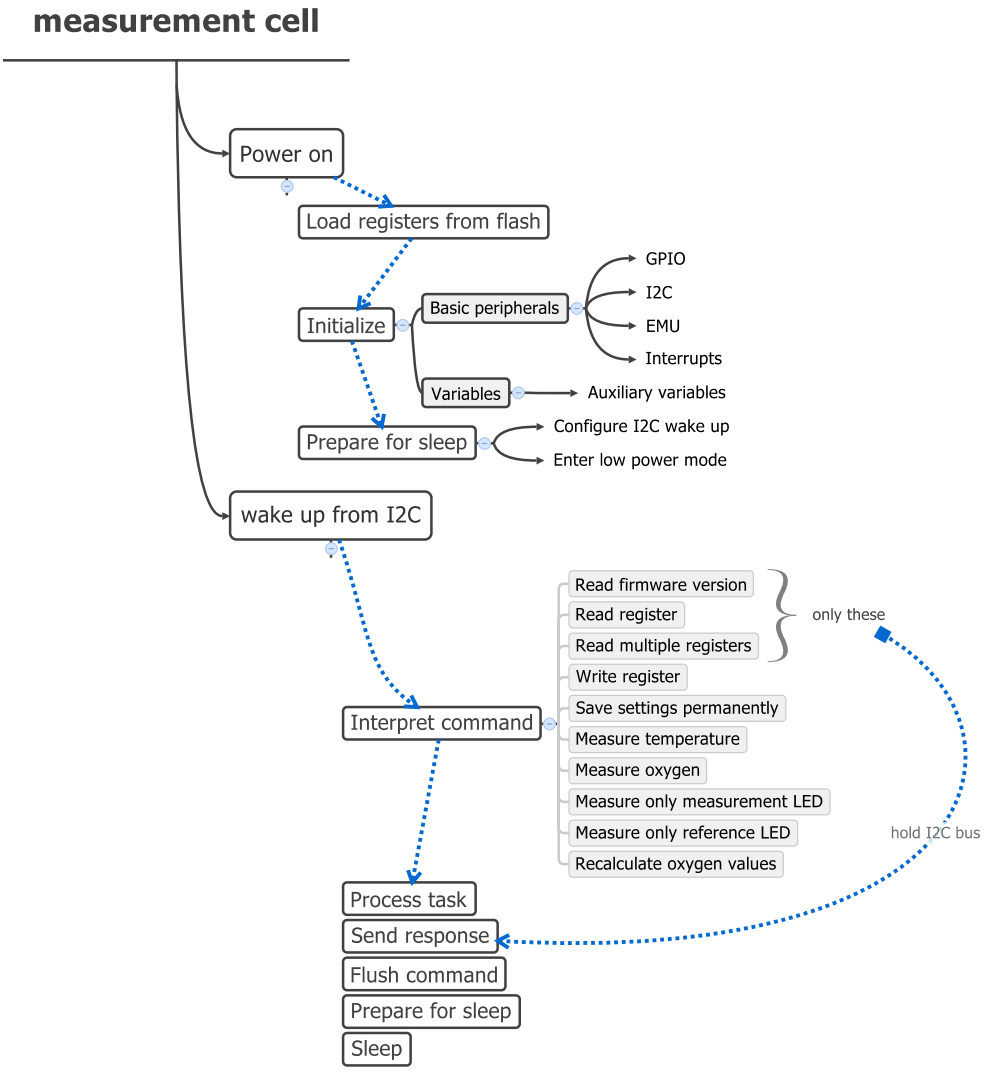

Figure 3.21.: Simplified outline of the code execution in the measurement cell. After powering up the cell it waits for commands in a very low power state. I2C commands addressed to the cell will wake it up and lead to the execution of the command, before going to a low power mode again.

3.4.2. Software

The software for the MCU was written in C using the Student Edition of the IAR Embedded Workbench® for ARM from *IAR Systems*[3]. A heavily simplified outline of the code execution can be seen in fig. 3.21.

The software is not discussed in detail in this work, however, some design concepts were already presented in 3.1.5. Coherent sampling was used, therefore the phase is derived by calculating the DFT of the input signal. The two-site model described by eqn. 2.18 in 2.1.5 was used to determine the oxygen partial pressure. After calibration at zero and air-saturated oxygen

[3]IAR Systems AB, Strandbodgatan 1, Uppsala, Sweden, http://www.iar.com/

pressure the software derives the necessary quenching constant K_D and stores it permanently in the MCU. Many parameters and all measurement results can be accessed via the computer, thus not only the oxygen concentration is provided, but also many raw values can be retrieved. This allows professionals to use the device for many other similar luminophores in order to determine their performance. The whole code for one cell uses 21,396 bytes of code memory and 3,648 bytes of data memory, leaving plenty of space for possible extensions.

3.5. Communication and power control

Fig. 3.22 shows the mainboard for the prototype, which is able to operate up to 64 measurement cells. The mainboard is powered by the USB-interface and provides the power supply and programming interface for the measurement cells. The MCU on the mainboard manages the communication between the computer and particular cells and controls the cells via an I2C-bus. It is connected to signalling LEDs and additional freely configurable in/out pins. The mainboard was designed to nicely fit under the measurement cells (almost no parts are placed on top) and has an overall size of $70 \times 30 \times 9$ mm.

Cells can either connect directly to it or via an auxiliary connection grid, which is a simple PCB just distributing all necessary traces to the cells and determines their alignment with

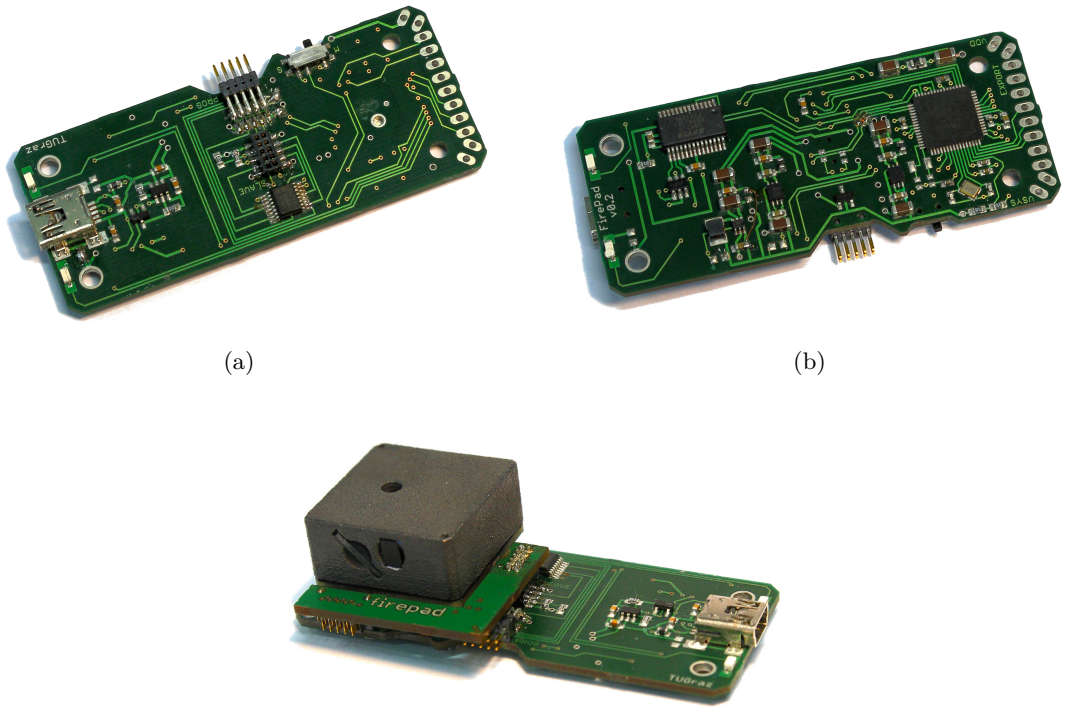

(a) (b)

(c)

Figure 3.22.: A top (a) and bottom (b) view of the mainboard In (c) one can see the one channel version of a prototype where just one cell connects to the board.

respect to the mainboard. In fig. 3.22(c) one can see a measurement cell connecting via a small auxiliary board to the mainboard and a similarly bigger board can be used to connect more cells.

3.5.1. Schematic and Layout

The mainboard has many features which include an USB-interface, power supplies, an I2C-bus for the cells, on-board programming plus debugging and some additional miscellaneous features.

USB-interface: The design of the USB-interface was done with the help of application notes from *FTDI*[4], which manufactures the USB-controller (FT232RL). The USB power lines are decoupled with an ordinary π-filter and all data and power lines are ESD-protected.

Power supplies: All different power supplies are sourced by the filtered USB-supply. The chosen voltage regulators provide low-noise and stabilised 3.3V supply and an additional π-filter decouples high frequency components of the following circuits. Every power supply is completely separated from each other to prevent coupling. The mostly digital load noise from the mainboard as well as the rather huge sinusoidal loading from the LEDs should not impair the measurement results. The power supply for the cells can be completely shut off by the mainboard MCU to reduce current consumption during non-measurement time. Thus, if no LED is needed for excitement all cells can be completely shut-down.

Communication: The MCU communicates with the PC via the FT232RL. Depending on the configuration it can use the low-energy UART or normal USART on this communication channel - if not needed the other pins are just configured as input. The RX-line also triggers an external interrupt on the MCU-port to allow a wake-up on UART. An I2C-interface connects the slaves with the mainboard MCU. For debug purposes the I2C and UART lines could be short-circuited and one measurement cell could directly communicate with the PC.

On-board programming and debugging: The mainboard MCU can be programmed while powered either via USB or the programming connector. To allow the same hardware to be used to program and debug a measurement cell an analog switch decides where to connect the program/debug-interface. If just one measurement cell is plugged into the slave connector the cell can be programmed or debugged on the same board where it is going to be used later on.

Miscellaneous: 8 Pins of the backbone MCU are connected to a standard connector to increase flexibility for future applications. A LED bar indicates the device status (on, off, low-power, etc.).

[4]Future Technology Devices International Limited, Unit 1, 2 Seaward Place, Centurion Business Park, Glasgow, G41 1HH, United Kingdom, http://www.ftdichip.com/

3.5.2. Software:

The mainboard controller just represents a communication extension for the measurement cells (I2C to USB bridge - defined as level 0 commands) and provides some minor additional functionality, e.g switching power supplies and visualizing the device state via the LEDs (marked as level 1 commands). Therefore most of the resources of the MCU are not used yet and the software is really simple and will not be discussed, however, there are intentions to upgrade it and add data-logging as well as stand-alone features to it.

The communication protocol of the mainboard was designed to communicate with the logging software provided by the company *Pyro Science*. This allowed a fast integration of the prototype in the labs as already installed software could be used to read out the values - just two days after the first prototype was finished it was used to determine lifetime of new luminescence sensors at the institute in combination with this software! A detailed scope of the possible commands can be looked up in the appendix D.

4. Results

4.1. Validation of the luminescence model

The model derived in 3.3 was validated with a measurement series. In order to see phase shifts due to non-linear effects of the luminophore the excitation light was focused on thin light fibres coated with an oxygen sensor on the tip.

The measurement setup consisted of:

- A Fiber-Optic Oxygen Meter from *Pyro Science* which offered various available excitation light intensity settings.
- Microsensors (light fibres) with coated fibre tips. The coating had to be done manually, thus, the coating layer thickness and diameter was expected to vary.
- 2 different sensors: PtTPTBF and PdTPTBF were used as phosphorescent dyes, which can be quenched by oxygen. 0.83 % luminophores were immobilised in a PVC matrix with 20 % softeners. Both types of luminophores show a similar behaviour and structure, however, their decay time varies tremendously. Unfortunately the sensors showed significant bleaching and their properties (e.g. decay time) varied a lot after coating.
- The coated microsensors were tested in a nitrogen atmosphere and in air to investigate the sensor with and without quencher.
- Before each measurement the device was calibrated with a microsensor coated with a fluorescent dye with a very short lifetime and matching emission spectrum. The noted phase shifts for different settings were subtracted from the measurements with the actual sensors.
- The excitation frequency used for PtTPTBF was 4 kHz and for PdTPTBF was 500 Hz.

The simulation was initialised with the parameters of the sensors taken from [8]. The actual decay time used for the simulation was assumed to be close to the measured decay time with the smallest light intensity (1 %). With the same assumption the quenching constant K_D was calculated. Most parameters could be determined very accurately, however, others had to be roughly estimated. Therefore the output of the simulation should deliver similar results, however, no accurate results were expected. Furthermore the results of the simulation should exceed the phase deviations of the measurements, as only the most affected layer (closest to the light source) was modelled and no diffusion was taken into account. A complete list of the simulation parameters can be found in the appendix C.

4.1.1. Sensor without quencher

The microsensors were placed in a vessel with a nitrogen atmosphere and for each sensor the excitation light was increased from 1% to 100% and the measured phase difference between main and reference was noted. The results shown in fig. 4.1 clearly show a drift to lower values, i.e. a negative phase shift, as it was expected in 3.3.3. The phase values for different PtTPTBF sensors are shown in fig. 4.1(a) with a theoretical phase shift of $\approx 56\,^{\circ}$. The PdTPTBF sensors in fig. 4.1(b) should have a phase shift of $\approx 45^{\circ}$. The slower dye showed a much higher shift with increasing light intensities as it has a much smaller k_r^T (compare with eqn. 3.23).

The simulation for both sensors shows that the same model can predict a negative phase shift for both cases, however, the prediction exceeds the measurements.

4.1.2. Sensor with quencher

After the sensors got characterised without any quencher the same sensors were placed in air and the phase deviations with increasing light intensities were measured again. The theoretical phase shift should be much smaller and as the quencher helps to deactivate the luminophores a much smaller phase error was expected.

The phase values for PtTPTBF sensors are shown in plot 4.2(a) with a theoretical phase shift of $\approx 32\,^{\circ}$. The PdTPTBF sensors 4.2(b) should have a phase shift of $\approx 12.6\,^{\circ}$. A quite unknown parameter is the rate of singlet-oxygen decay k_o for polymers and it was roughly estimated to be in the range of $(18 - 30)\,\mu$s as mentioned in [35]. This value has a big effect on the simulation results. With shorter oxygen lifetimes both simulations again exceedingly predict the phase deviations, but are also smaller compared to the results without a quencher.

The simulation shows in fig. 4.3 which percentages of PtTPTBF and quenchers are in the excited state depending on the light intensity. For the highest intensity almost 65 % of the luminophores and 90 % of the quenchers are excited. Thus only a small amount of oxygen is in the ground state, which explains the heavy effect on the phase simulations in fig. 4.2.

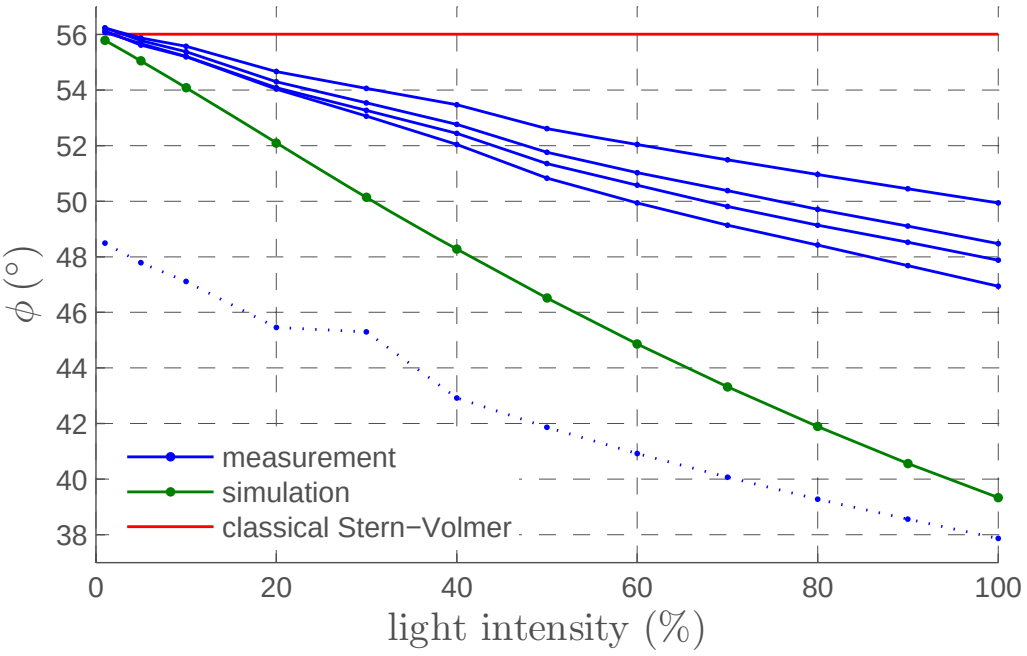

(a)

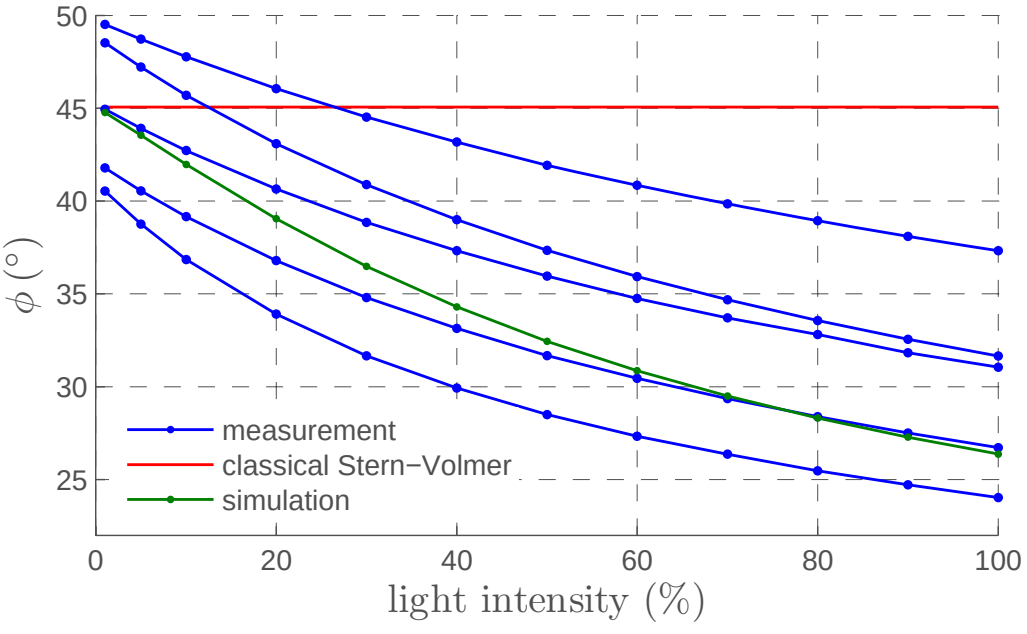

(b)

Figure 4.1.: Measured and simulated phase deviations from the theoretical value for the phase shift of two different sensor types in a nitrogen atmosphere.

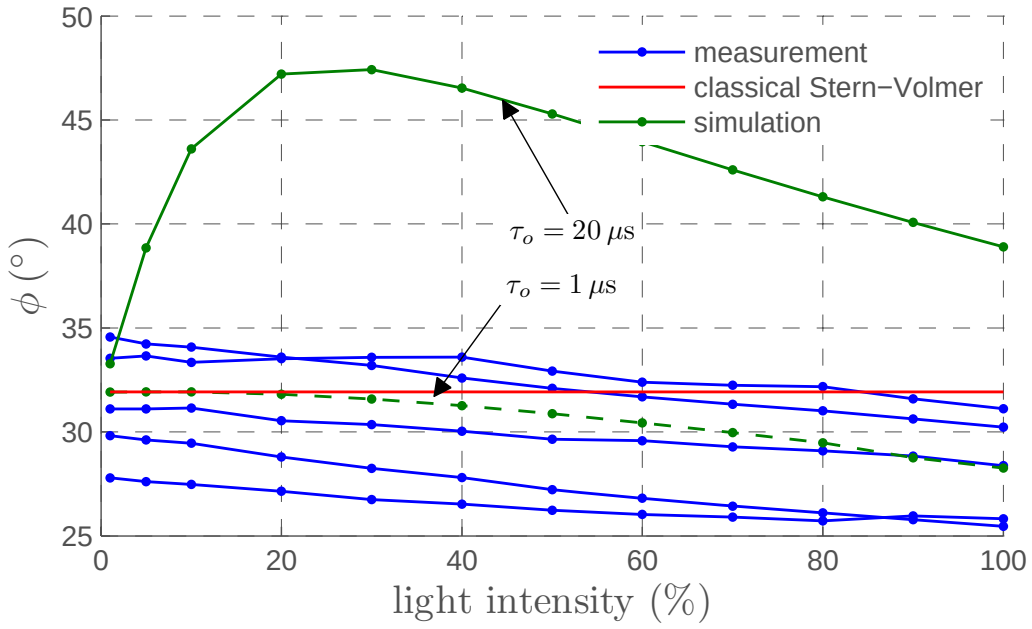

(a)

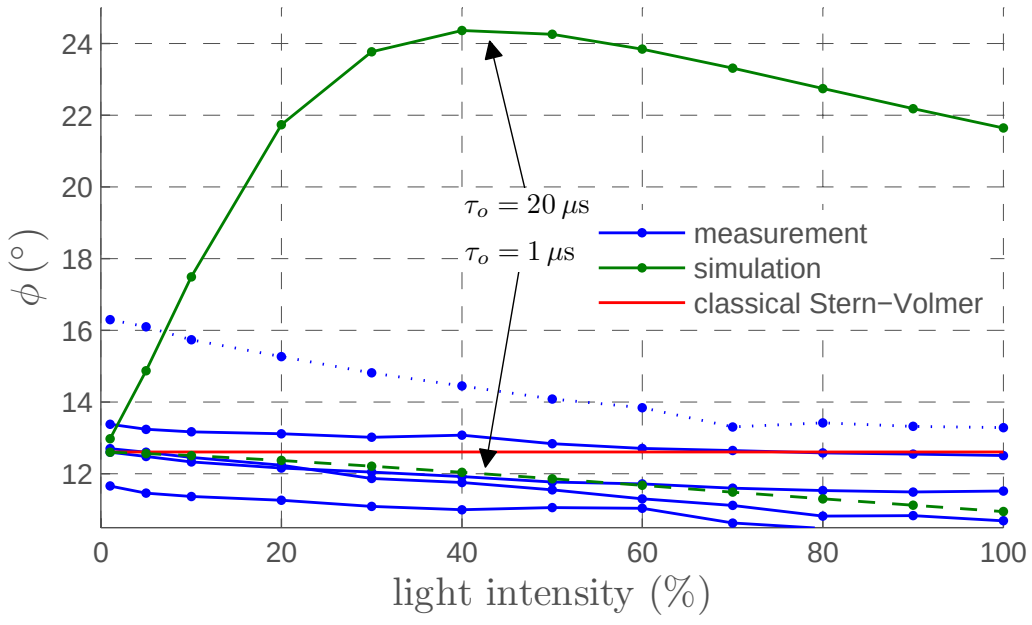

(b)

Figure 4.2.: Measured and simulated phase deviations from the theoretical value for the phase shift of two different sensor types in air.

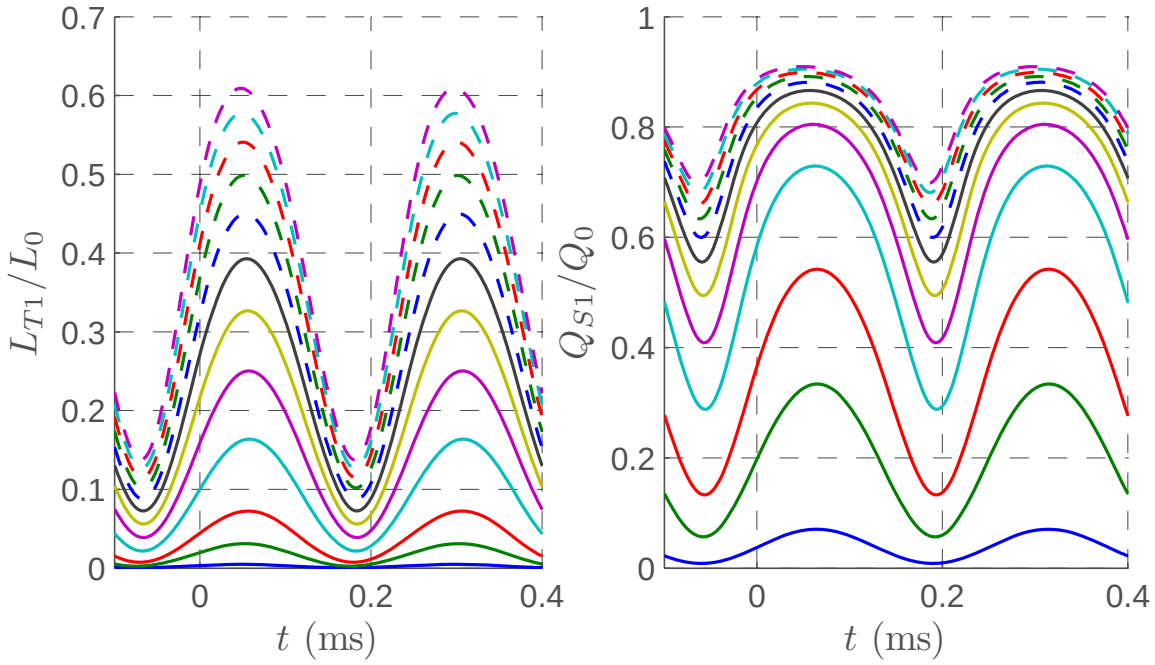

Figure 4.3.: The concentration of PtTPTBF and oxygen in the excited state referred to the actual luminophore and quencher concentration for different light intensities ($1, 5, 10, 20, 30, 40, 50, 60, 70, 80, 90, 100\,\%$ from bottom to top) with an assumed lifetime of singlet-oxygen of $20\,\mu$s.

4.2. Realised prototype designs

Two different prototype designs were finished with the assembly of mainboards and measurement cells with two different connection grids. In fig. 4.4(a) a one channel phase fluorometer was realised with one measurement cell connecting to the mainboard. A mainboard plus four measurement cells were connected to form a 4-channel phase fluorometer in fig. 4.4(b). Both prototype cases were printed using a 3D-printer and their top was covered with a thin glass plate. The outline of the one channel design is $78 \times 44 \times 26\,\text{mm}$ and of the 4 channel one is $80 \times 80 \times 26\,\text{mm}$, which is slightly higher compared to the precursor model in fig. 1.4 as a result of the new optic concept and modular assembly.

(a) (b)

(c)

Figure 4.4.: The final prototypes realised in this work including a one channel (a) and a 4 channel (b) version. (c) The 4-channel version shown in a standard setup in the lab with different luminescence sensors on the read-out spots.

The realisation of both designs should show how easy it is to rearrange the number and position of measurement cells to a completely new measurement device that fits the design specifications given by the user. The measurement of oxygen by using the specified phosphorescent sensors is user-friendly and comfortable in combination with the logging software provided by *Pyro Science* as shown in fig. 4.4(c).

4.3. Prototype testing

In order to get comparable results many of the properties of the newly created 4-channel phase fluorometer were tested against the precursor model. The measured results in the following paragraphs are summarised in tab. 4.1 and should also reflect the simulation results presented in 3.1.3 and 3.1.4.

Table 4.1.: Characteristics of the phase fluorometer

PARAMTER	CONDITION	MIN	TYP	MAX	UNIT
Possible number of channels of the phase fluorometer		1	—	64	
Excitation modulation frequency f_m		250	—	5000	Hz
Sensor measurement time T_m	$f_m = 4\,\text{kHz}$	1	—	2500	ms
Main LED current[1] I_{main}		4.5	—	90	mA
PD current amplification[1] R_{amp}		680	—	6800	kΩ
Phase deviation over I_{main} range	$f_m = 5\,\text{kHz}$	—	—	1	°
Phase deviation over R_{amp} range	$f_m = 5\,\text{kHz}$	—	—	0.3	°
Phase deviation after calibration[2]	$f_m = 5\,\text{kHz}$	—	0.02	—	°
Electric crosstalk		—	—	40	pA
Optic crosstalk[3]		5.5	6	8.2	pA/mA
Phase deviation due to XT[4]		—	0.05	0.57	°
Phase noise std. deviation[4]	$T_m = 100\,\text{ms}$, $f_m = 5\,\text{kHz}$	—	0.0025	—	°
Phase resolution[4]	$T_m = 100\,\text{ms}$, $f_m = 5\,\text{kHz}$	—	0.01	—	°
pO_2 resolution[5]	$T_m = 100\,\text{ms}$, $f_m = 5\,\text{kHz}$	0.033	—	0.11	hPa
Phase drift	$5 - 60\,°\text{C}$, $f_m = 5\,\text{kHz}$	0.05	0.1	0.5	°

[1] can be set to values from min to max in 8 steps
[2] phase correction values are added for every I_{main} and R_{amp} setting
[3] input referred as PD photo-current normalized to I_{main}
[4] for 0.5 V signal amplitude after amplification
[5] using an oxygen sensor with $K_D = 0.011\,\text{hPa}^{-1}$

4.3.1. Transfer function

In fig. 4.5 bode plots for the new and old design are shown. The new design matches very well with the simulation results (see fig. 3.7 in addition with fig. 3.5(a)). The offset in between the channels for the new design can be due to a slight mismatch of the reference voltage for the PDs and the internal reference for the ADC, but the curvature is the same. The channels of the old design cannot have such a mismatch as the reference voltage for the PDs was taken from the ADC directly, however, they all have a different curvature, which can be due to component variations in the different channels. The overall phase shift in the new design is decreased, which should improve temperature characteristics (see 3.2.3).

4.3.2. Crosstalk

The crosstalk was tested by placing no sensor on the read-out spots of the device. In fig. 4.6(a) the amplitude and phase of the crosstalk signal for various amplification settings over the excitation light intensity can be seen. For very low light intensities an electric crosstalk is inherent with a phase shift of almost 180 degrees. With increasing light intensities the optic crosstalk takes over, shifting the phase towards 25 degrees (which can be expected at a excitation frequency of 5 kHz, see fig. 4.5(a)). The performance of the new design can be compared to performance of the precursor in fig. 4.6(b). The bode plot of the crosstalk in fig. 4.7 shows that the new design is dominated by optical crosstalk, which is almost frequency-independent, whereas the old design shows a significant capacitive coupling.

The maximum crosstalk for the worst-case setting stays below 5 mV, i.e. XT $< 1\,\%$ for 0.5 V signal amplitude and could yield to $\approx 0.57\,^\circ$ phase error. For better cases (lower amplification settings) crosstalk related errors can go down to $^5/_{100}\,^\circ$ and below. These errors are systematic ones and can be calibrated as well.

4.3.3. Noise

The measurement cell uses two channels (reference and main) to calculate the actual phase shift, therefore both channels will introduce noise to the final result. The reference channel was optimised for low noise, thus is always operated at an amplification of 1 and a LED intensity, which yields to approx. 0.5 V signal amplitude. Consequently the noise performance mostly depends on the main channel. This was tested by gradually reducing the excitation intensity while the AGC ensured approx. 0.5 V input signal amplitude. In fig. 4.8(a) the distributions of the phase noise under these testing conditions are shown and it can be seen that the standard deviation of the phase for the measured SNR (≈ 70 dB) is ≈ 0.0025 deg, i.e. a resolution of $^1/_{100}\,^\circ$ is achievable. This is way better than predicted by eqn. 3.11, but explained by the simulation results in fig. 3.14. Both devices show a better performance for smaller amplification settings, i.e. higher detected light intensities and both devices perform similarly over the selected amplification range. The old design outperforms the new one in terms of noise when low light intensities should be detected.

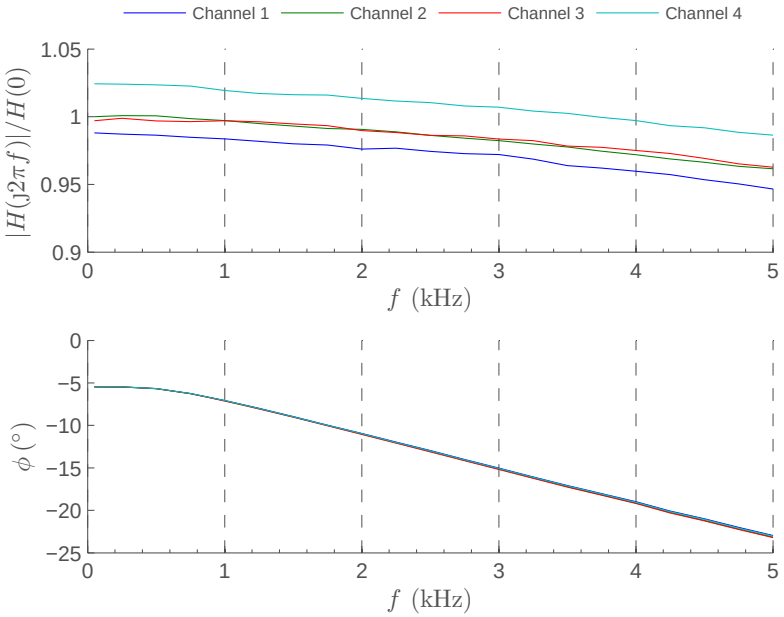

(a) New design

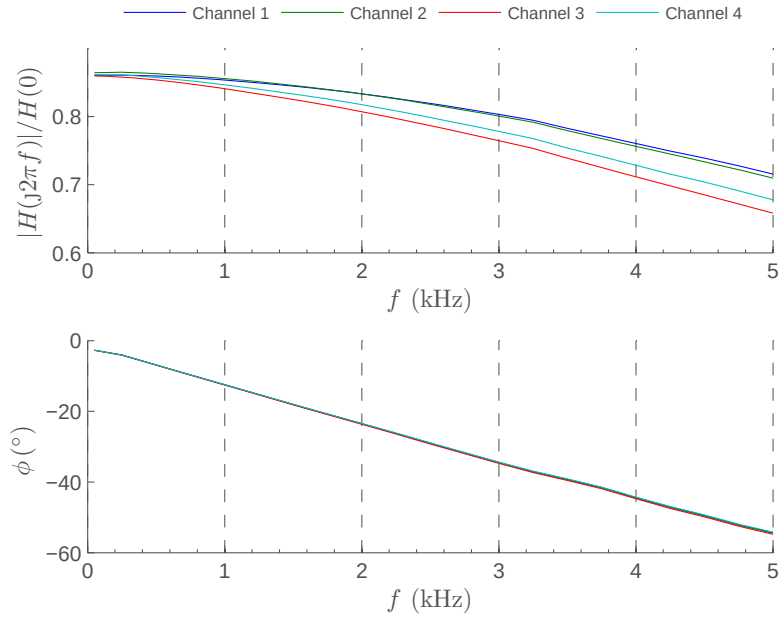

(b) Old design

Figure 4.5.: The transfer functions for all channels of the whole signal chain without a luminophore. The curve was measured using the reference LEDs.

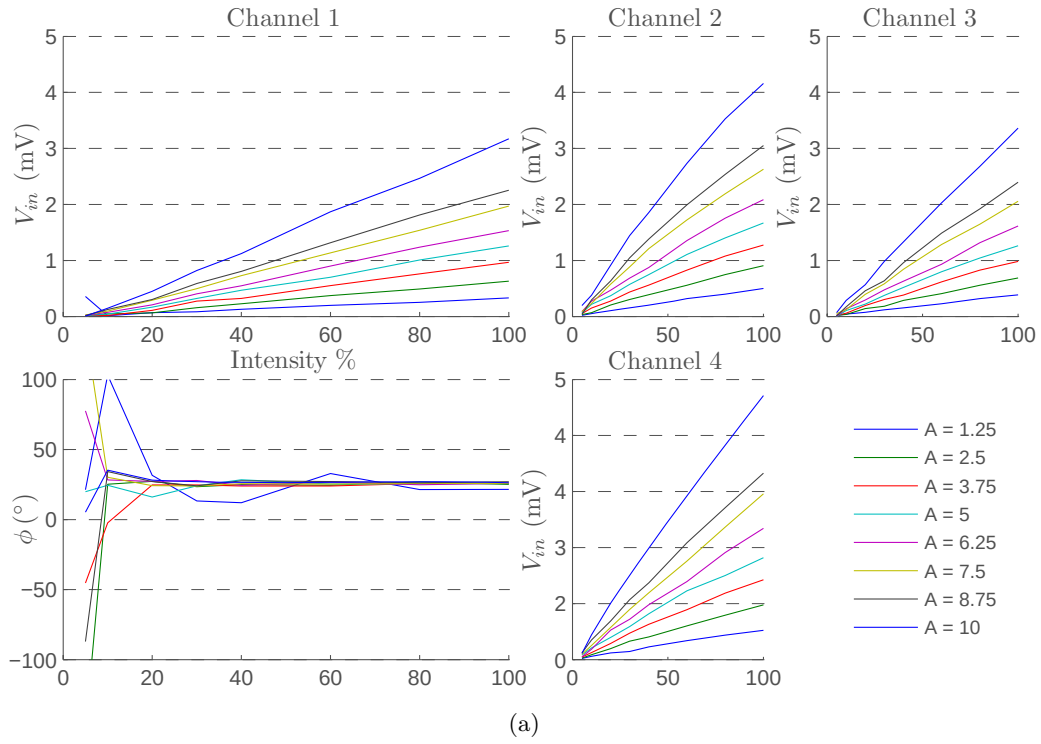

(a)

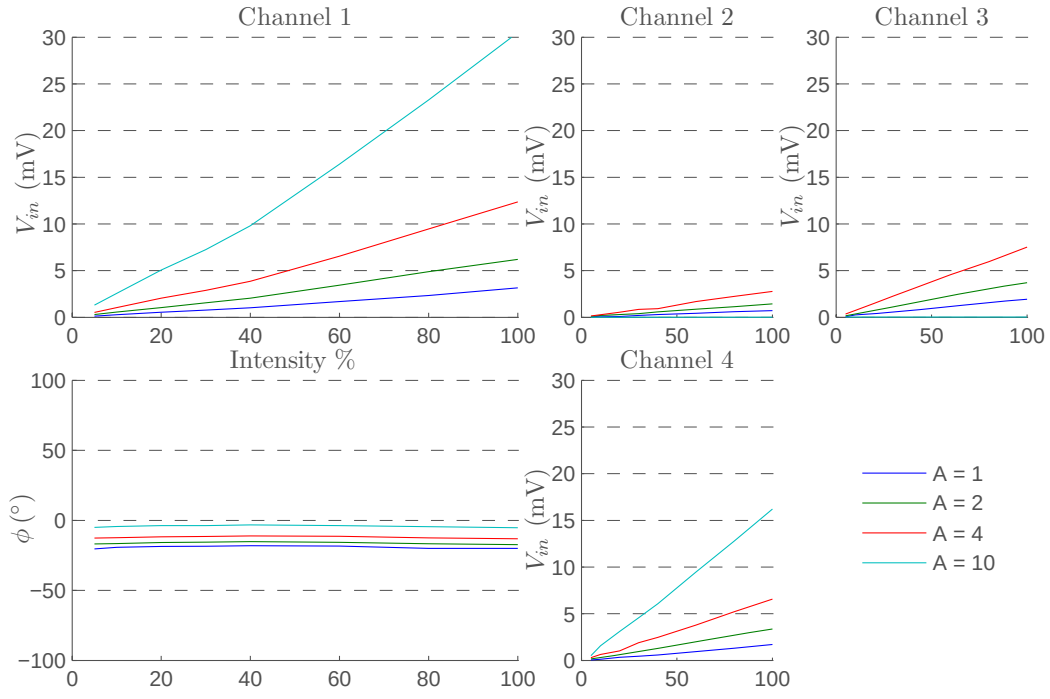

(b)

Figure 4.6.: Crosstalk amplitude and phase (only channel 1) for different amplification settings (A) and light intensities of the new (a) and the old design (b). All measurements were taken - without a sensor applied - with an excitation frequency of 5 kHz.

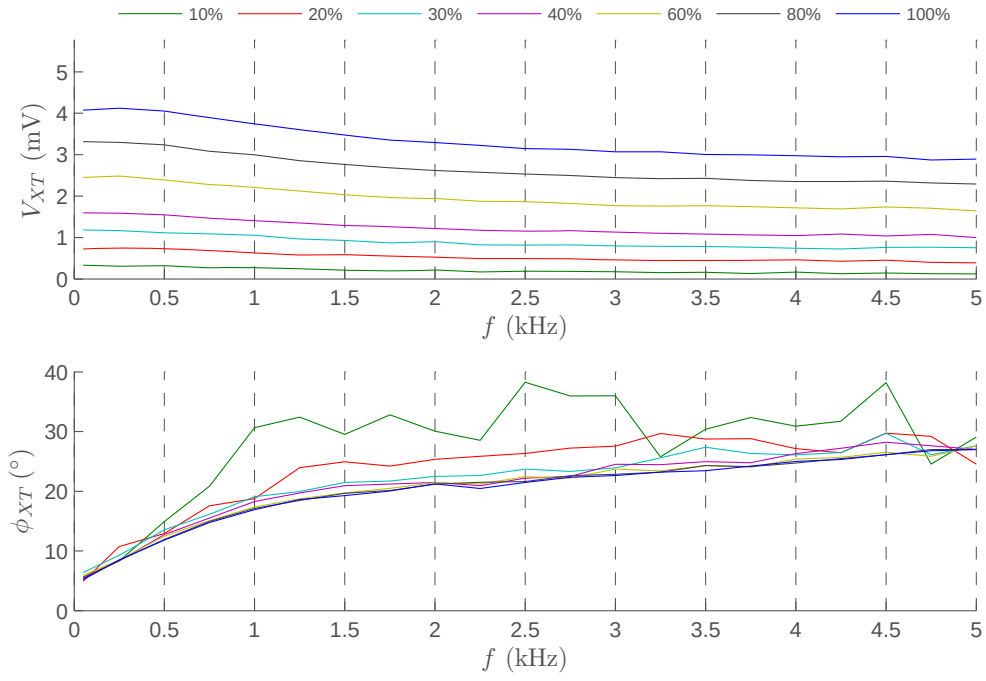

(a)

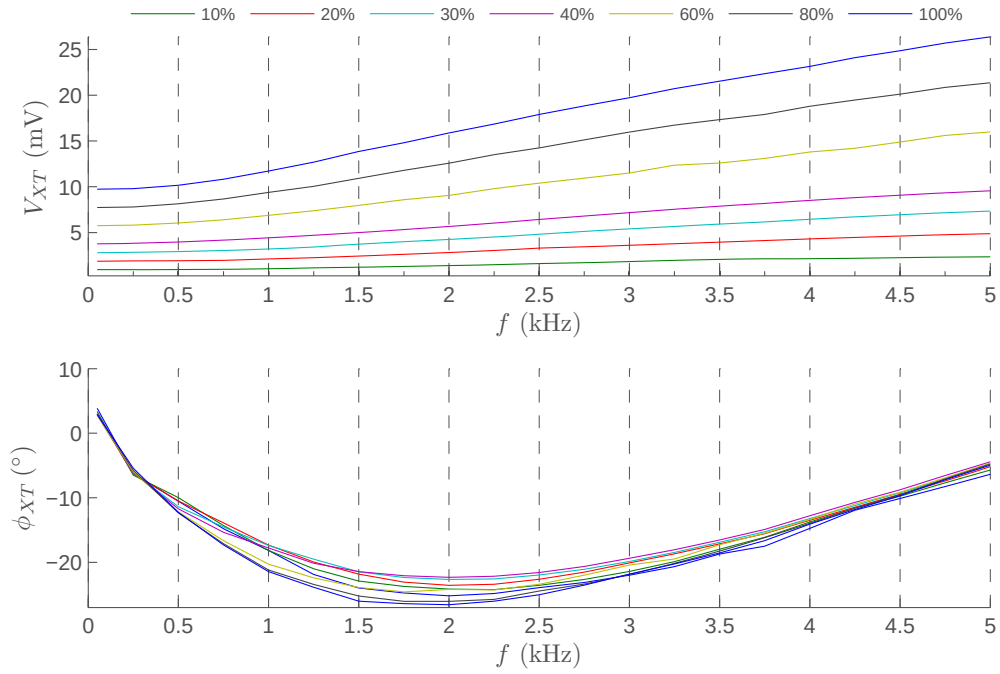

(b)

Figure 4.7.: The transfer function of the crosstalk at different light intensities for channel 1. Amplification was set to $\approx 5\,\mathrm{M}\Omega$ for both devices.

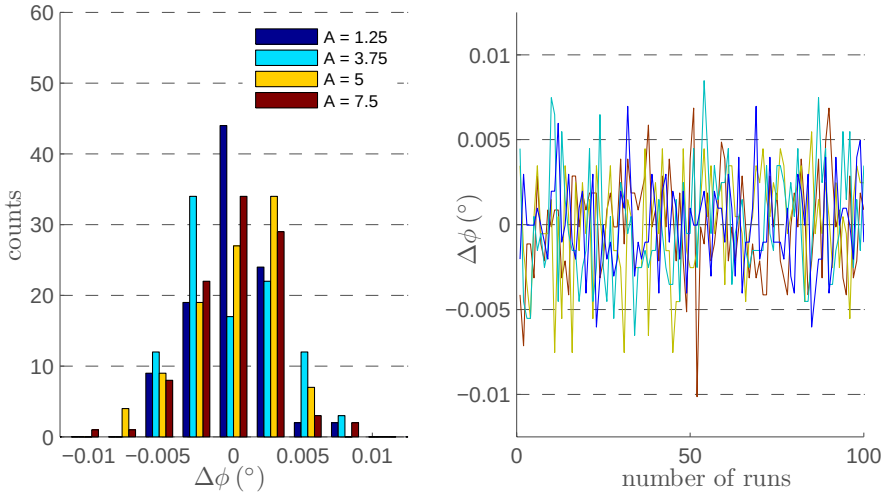

(a)

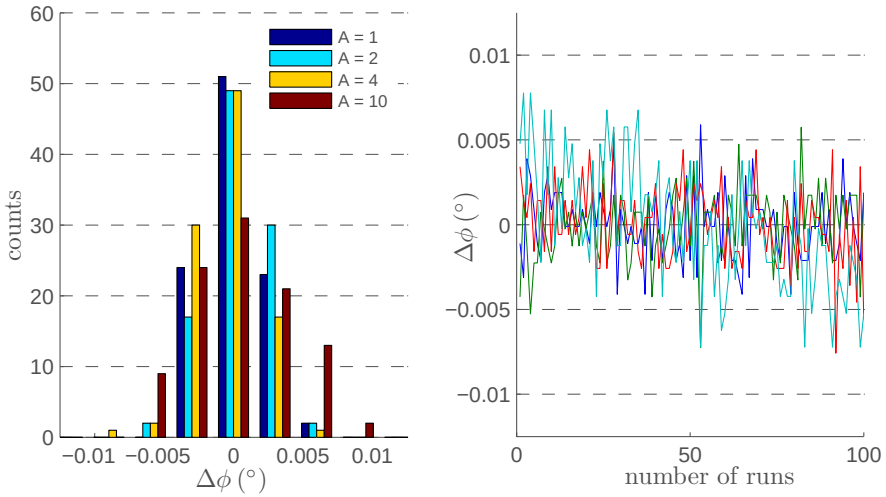

(b)

Figure 4.8.: The phase noise distribution of the prototype (a) with different amplification settings (1,3,4 and 6). The input signal amplitude was kept at $\approx 0.5\,\mathrm{V}$, $f_s = 320\,\mathrm{kHz}$, $f_{in} = 5\,\mathrm{kHz}$ and $N = 64 \cdot 100$. The precursor phase noise distribution was measured (b) with similar settings.

4.3.4. Errors and drifts

The performance of the device is affected by ambient conditions, such as temperature and light. However, also internal settings of the device (such as amplification and LED intensity settings) will influence the measured phase. These unwanted phase errors can be calibrated at room temperature and stored in the MCU of the measurement cell.

Phase deviations for different settings

The prototype was designed to reduce phase shifts due to amplification or intensity changes and fig. 4.9 shows the residuals. In order to compensate for these errors the prototype was calibrated with a fluorescent dye having a very short lifetime, which should yield a phase shift of zero degrees. These phase offsets were stored in the MCU for every light intensity and amplification setting. The measured phase is corrected by these offsets and this will result in a much better absolute accuracy, which is around $\pm 2/100\,^\circ$ for well calibrated channels (e.g. 1,4 in fig. 4.10).

Temperature-dependent phase drifts

The 4-channel phase fluorometer was put into a cryostat enclosed in a waterproof bag with a fluorescent (zero-phase) dye placed on the read-out spots. The temperature in the cryostat was changed in 5 degree steps every 45 min from 5 °C to 60 °C. 25 min after the temperature was set the prototype performance was tested.

With increasing temperature the amplitude of the input signals decreased and it can be seen for both, the excitation and reference channel in fig. 4.11 and fig. 4.12. This can be explained because of increasing thermal (non-radiative) deactivation in the LEDs and the fluorescent dye described in 2.1.3. The temperature influences the measurements over a big frequency range with no obvious trend towards higher or lower frequencies as seen in fig. 4.13 and fig. 4.14. After calibration at room temperature, one can see the expected phase error of the prototype for different temperatures in fig. 4.15. Actually the reference channel should compensate most of these drifts, however, the errors heavily depend on the excitation light intensity, whereas in every channel the least affected setting was with highest intensities, allowing measurements with phase errors lower than $\pm 1/10\,^\circ$ over the full temperature range.

Phase errors due to ambient light

The 4-channel fluorometer was tested under various ambient light conditions to see if it shows any effect on the phase measurement and under which conditions the ambient light exceeds the measurement input range. The ambient light reduction circuit as described in 3.1.4 was not implemented in software before these measurements were taken, therefore is left out of discussion. Measurements were taken with the sensor specified in 1.2.1 spotted on an open vessel and the measured phase angle was $19.76\,^\circ$ in a dark room (air-saturated). The settings for these measurements were 100% excitation light intensity and an amplification of $A = 3.75$.

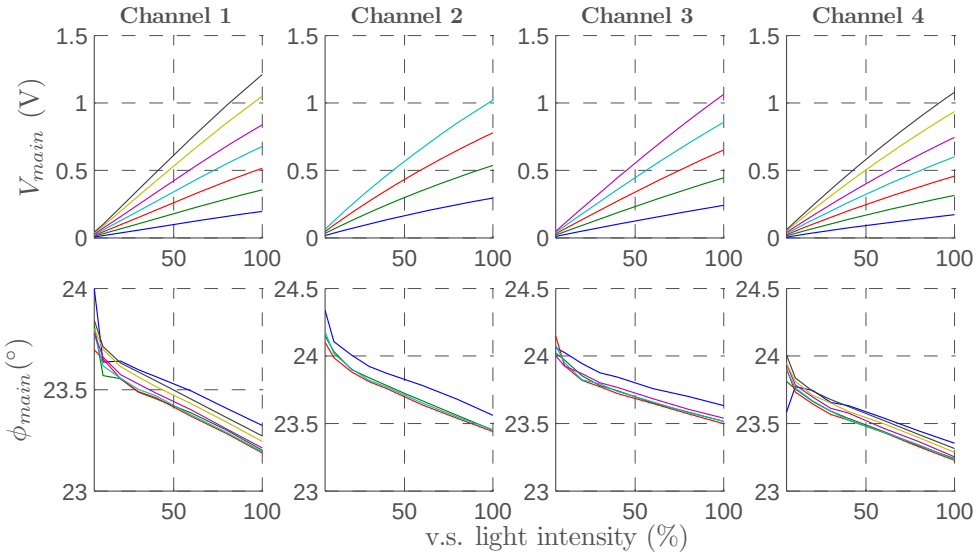

(a)

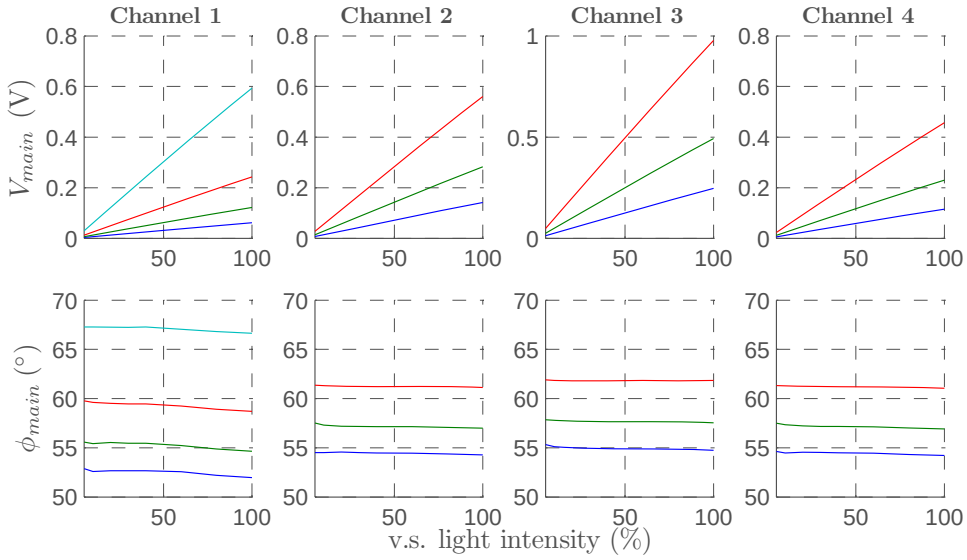

(b)

Figure 4.9.: Both new (a) and old (b) design changes the phase with different amplification settings (represented by different colours) and excitation light intensities. The values were determined at 5 kHz excitation frequency and amplification settings causing signal overshoot were removed.

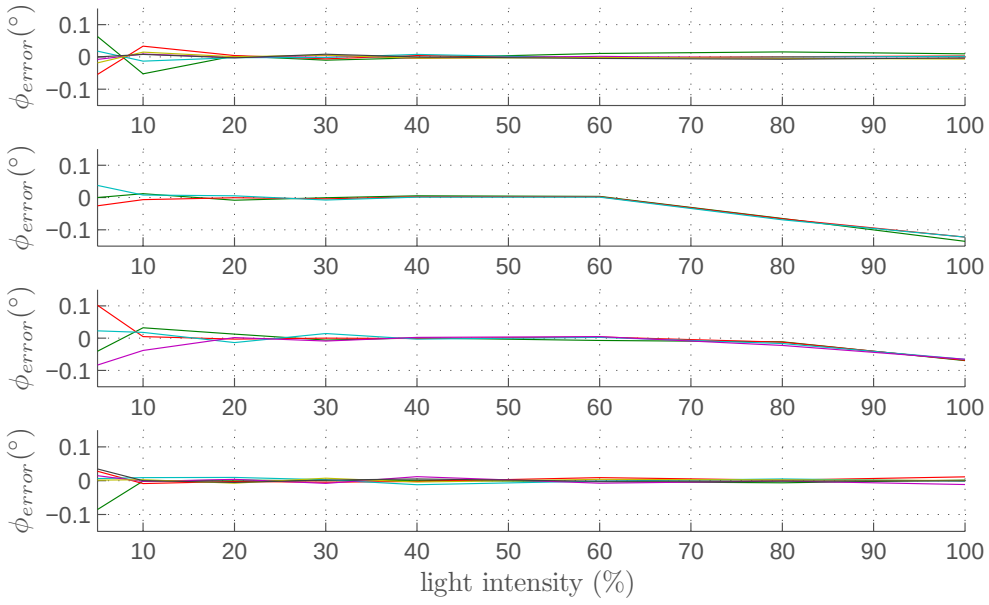

(a)

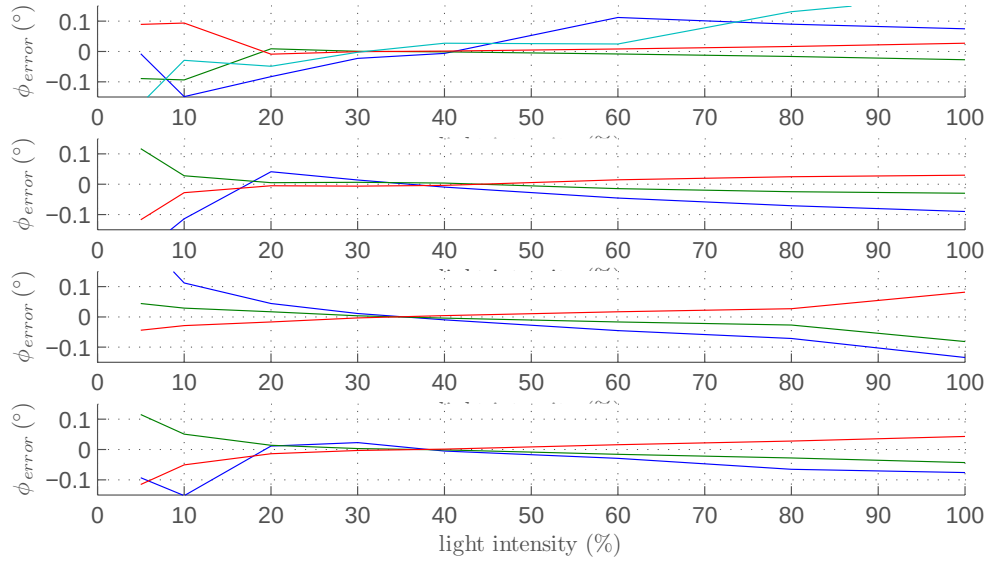

(b)

Figure 4.10.: The phase error for the new (a) and old (b) design for each channel (1-4 from top to bottom) at a frequency of 5 kHz for different light and amplification settings.

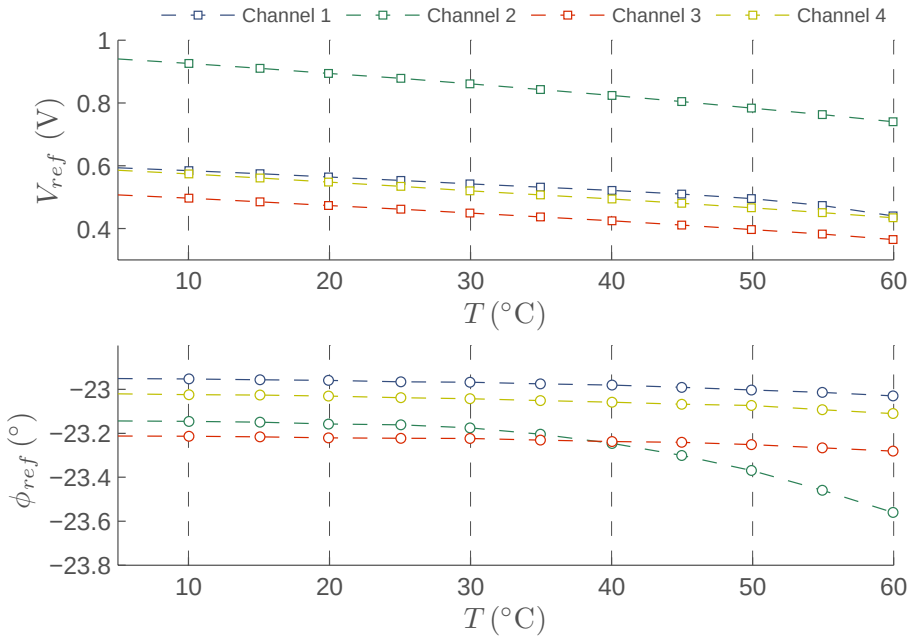

Figure 4.11.: The amplitude and phase of four reference channels at 5 kHz excitation frequency. Channels 1,3 and 4 show a very similar performance, Channel 2, however, has a much higher signal output, which badly effects the phase.

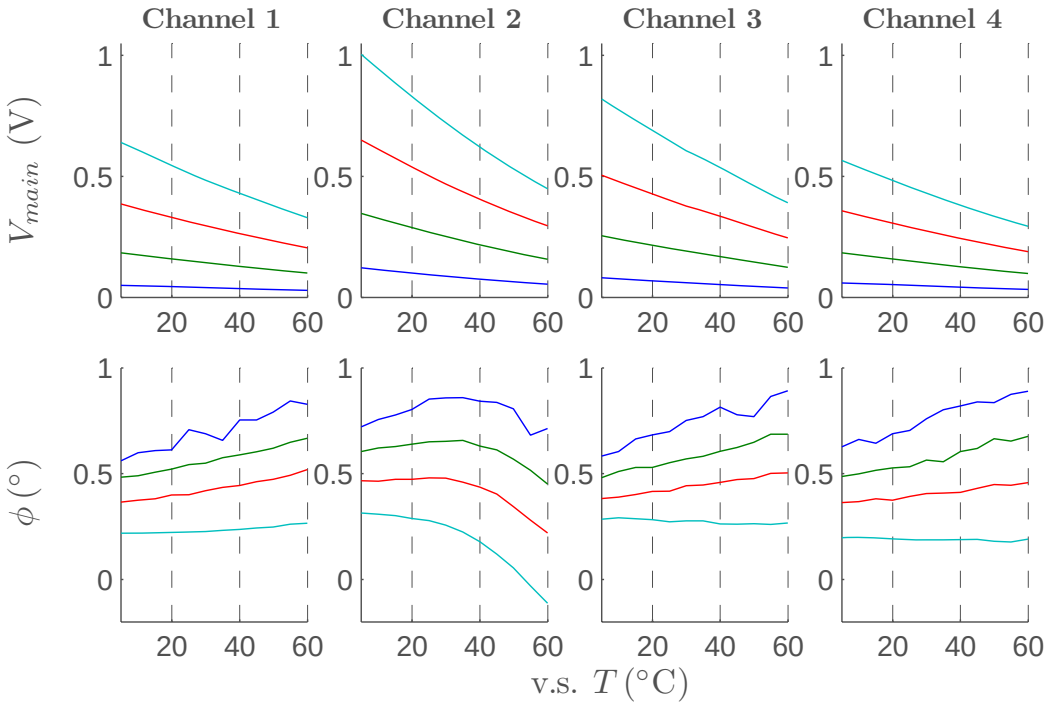

Figure 4.12.: The absolute amplitude of the emission light and the phase difference (main - reference) of all channels at 5 kHz for different excitation light intensities ((10, 30, 60, 100) %).

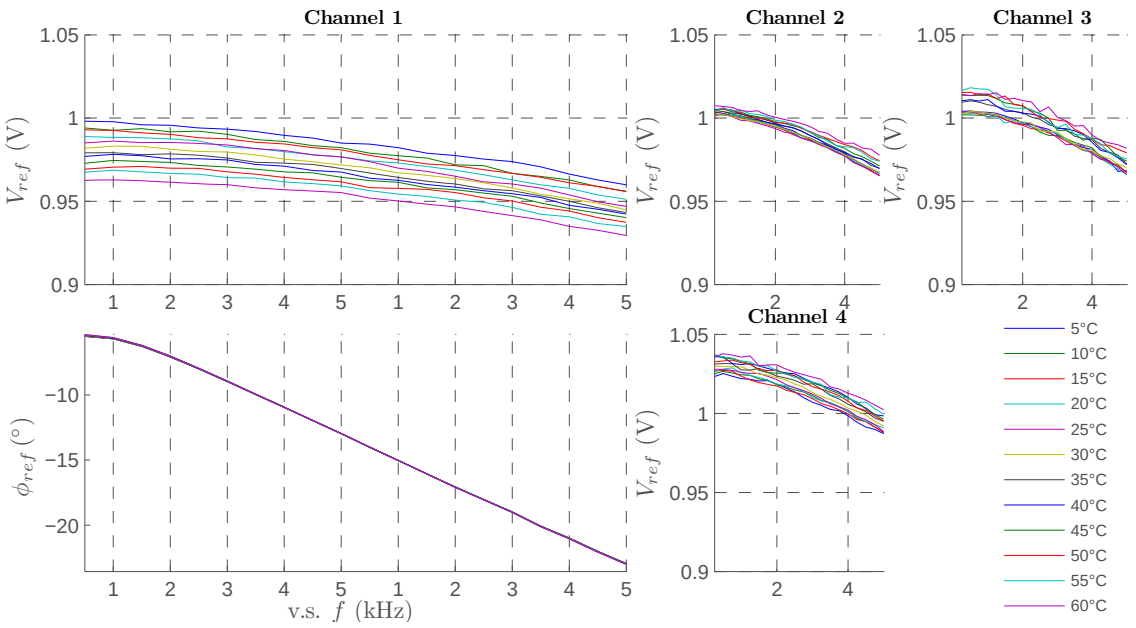

Figure 4.13.: The transfer function of four reference channels (phase only for channel 1) retrieved at different temperatures.

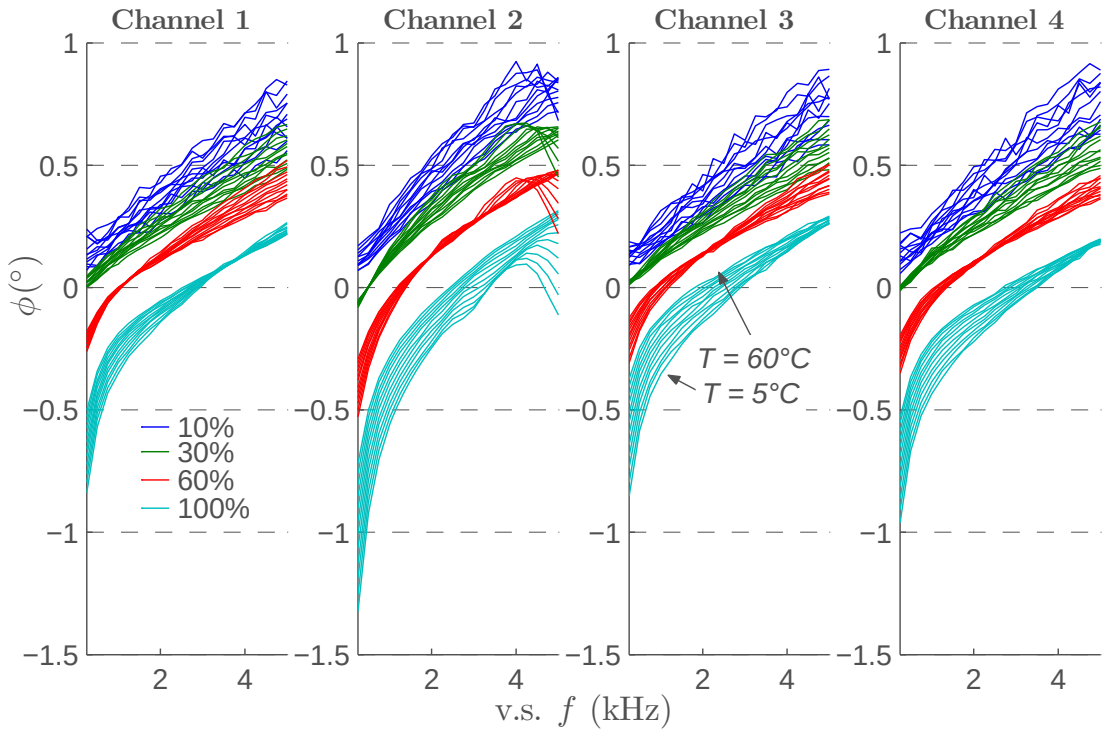

Figure 4.14.: The measured phase difference between reference and excitation channel over the excitation frequency for different excitation light intensities. The width of same coloured bands shows the affect of temperature on the phase at different frequencies.

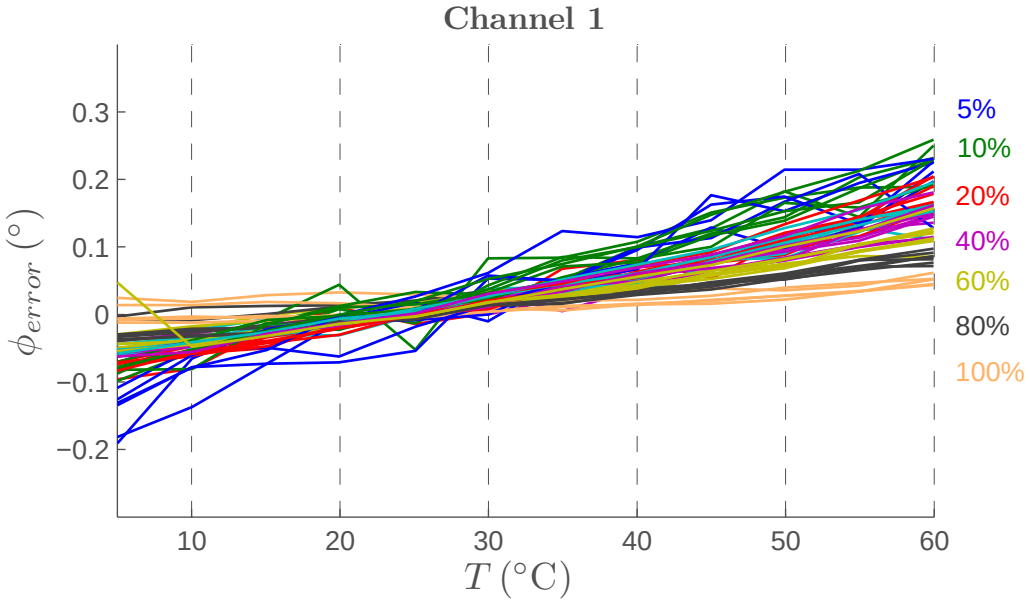

(a)

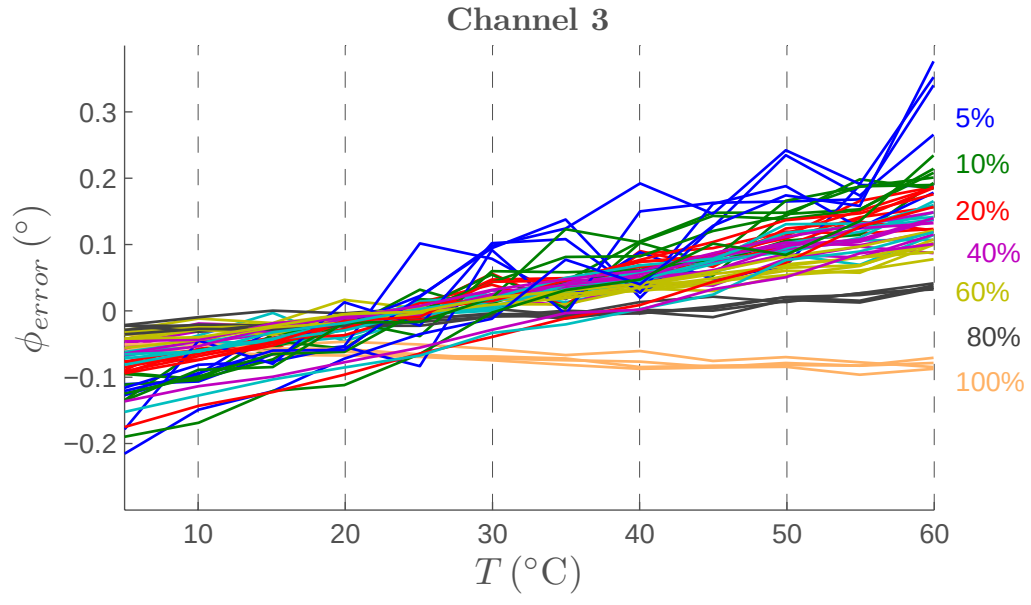

(b)

Figure 4.15.: This graph represents the expected phase error for different temperatures and amplification settings at different excitation light intensities for a calibrated channel at 25 °C. Same colours belong to same intensities and varying amplification settings are represented by same coloured lines. Amplifications which resulted in overshot signal were removed.

Table 4.2.: The influence of ambient light (AL) on the phase.

Possible application	**AL (mV)**	ϕ_{error} (°)	**Comments**
Dark room with halogen lamp	≈ 600	1/100	lamp distance 30 cm with 45° incident light angle
Dark room with halogen lamp	≈ 1300	8/100	lamp distance 20 cm with 45° incident light angle
Dark room with halogen lamp	≈ 1200	7/100	lamp distance 100 cm from straight above
Dark room with neon lamp	≈ 40	$< 1/100$	ceiling light
Bright lab	≈ 50	$< 1/100$	ceiling neon light
Bright lab	≈ 230	$< 1/100$	right next to a window, sunny day
Fume blast in the lab	≈ 26	$< 1/100$	fume blast light off
Fume blast in the lab	≈ 83	$< 1/100$	fume blast light on
Outside with direct sunlight	> 2500	$\ggg$	
Outside in the shadow	≈ 2100	$\ggg$	sunny day, diffuse shadow
Outside in the shadow	≈ 600	1/100	sunny day, hard shadow

Although the room was completely dark an offset of $\approx 3mV$ could be measured. At these settings the sensor emission light generated about 500 mV signal amplitude.

Starting with these values different typical application possibilities as listed in tab. 4.2 were tested. It can be seen that for normal lab operation the prototype works just fine with almost neglectable phase errors caused by ambient light. However, if the device is going to be used outdoors it should be shaded properly.

5. Conclusion

5.1. Non-linearities in luminescence

The results shown in 2.2 dramatically illustrate the large error possibility due to measurements with high light intensities. This will happen more likely as high intensities easily occur in microsensor applications [36] and better sensors with very high extinction coefficients [8] are developed. Without considering a quencher in the system the phase errors are strictly negative (compare to fig. 4.1), which would allow to compensate for those errors by measuring at two light intensities and interpolate the correct value. However, with quenching both effects partially cancel out each other and an interpolation seems very difficult. The non-linearities caused by high light intensities without any quencher are overcome with time domain measurements, as they only consider the falling slope of the signal which is not affected and the lifetime can be described properly with the linear model.

As could be seen in fig. 4.2 the oxygen relaxation rate k_o heavily influences the simulation results, whereas the higher rate better fits the measurements, although a much lower value was proposed by [35]. As mentioned in the model in 3.3 the simulation was just run for one mono-layer of the sensor with taking no diffusion into considerations. However, if triplet-oxygen would diffuse into this mono-layer from the surroundings it could easily compensate for the missing oxygen in the singlet-state. The diffusion would act similarly as a lower lifetime (i.e. a higher k_o) in the model and explain the measurement results better. More research in the relaxation of singlet-oxygen, the corresponding diffusion processes and adoptions to the model for diffusion is needed to establish a better understanding of oxygen quenchable luminescence.

As the luminophore steps out of the linear model the Beer-Lambert law cannot be applied any more as it assumes a constant luminophore concentration in the ground state over the layer thickness. Actually the sensor could get transparent with increasing light intensities if no excitation from the T_1-state to higher triplet-states occurs and the ground state gets depopulated. This sounds similar to establishing the first precondition of building a LASER and in fact a laser pump works according to the same principles.

The huge deviations in the measurement data was due to badly manufactured sensors, which were still not stabilised as the measurements were recorded. It is necessary to repeat the validation of the model with better specified and stable sensors. An experiment with different luminophore concentrations immobilised in the sensor matrix could be used to verify if there is a dependency of non-linearities as described by eqn. 3.26. To clarify the influence of oxygen diffusion in this system it would be helpful to prepare sensors with diffusion barriers for oxygen.

Strategies to avoid non-linearities

1. Measure with the smallest light intensities possible and try to capture as much of the emission light as possible for a qualitatively good signal. Super-bright luminophores will generate more emission light, however, will run much easier out of the linear boundaries of the model, thus the excitation light may have to be reduced in the same way the emission light would increase.
2. Luminophores with short decay times (e.g. fluorophores) are very linear and will not show any distortion over a wide range of light intensities. Instrumentation for these short decay times, however, is much more complicated as the modulation frequencies have to be selected higher and keeping the phase resolution high will cost a lot effort.
3. Sensors with low-concentrated luminophores will show less deviations caused by the depopulation of quenchers, however, to maintain emission signal levels thicker sensors have to be used, which will decrease the response time caused by the thicker diffusion layer.
4. Sensor matrices should be used with a short lifetime for singlet-oxygen. Another possibility would be an induced deactivation of singlet-oxygen by another molecule which has a fast reactivation.

5.2. Prototype performance interpretation

The prototype performance was matching really well with most of the simulations done in 3.1. The small variances in the transfer function in fig. 4.5(a) can be caused by mismatched reference voltages used for the ADC and the instrumentation circuit and could be improved by differential sampling. The noticeable phase shift deviation towards $-5\,^\circ$ at very low frequencies is unwanted and may be a reason of aliased higher frequency components caused by the DAC (fig. 2.27) as a fixed oversampling ratio is used in signal generation. The AAF was designed for an excitation frequency in the range of kHz and doesn't attenuate the signal distortions at low frequencies, which get aliased into the frequency bin of the excitation frequency. Therefore the oversampling should be increased at lower frequencies.

The crosstalk was expected to be reduced with the new design which could be shown in fig. 4.6, however, the optical setup still generates most of the crosstalk. It is assumed that further improvements could be made by replacing the light fibre in the read-out hole with lenses in order to introduce optical gain for the sensor and to better suppress out of focus ambient light.

The noise performance slightly suffered from the design changes. The standard deviation of the phase noise is approx. by a factor of 2 higher than the old design (see fig. 4.8), however, this was expected and opened the door for many other features, such as the two stage design with relaxed specificatons for the individual amplifiers. A further decrease in phase noise is expected if a better ADC (reducing jitter and increasing the ENOB) is selected. The simulation of the sampling process in 3.2 shows that even with the dithered input signal the quantization generates harmonic distortions and therefore the resolution is too small.

The two stage design reduces the phase changes introduced by different amplifications as it can be seen in fig. 4.9. With the new design changes in light intensities affect the phase much more than a change in the amplification setting, whereas in the old design it was the other way around. Thus it is much easier to calibrate for different amplifications than for intensities. Furthermore fig. 4.15 shows that the phase error for different amplification settings over temperature is almost neglectable, but it largely depends on the light intensities . High light intensities seem to be less affecting the drift as the thermal heating of the LED pn-junction with high currents could make it almost independent of the ambient temperature and therefore reduce the phase drifts. If the reference LED intensities would be changed accordingly to the main LED or if just directly the light of the main LED could be used as reference, the temperature effects might cancel out. However, the individual sources of these drifts still need to be clearly identified.

By looking at the transfer function for the phase error caused by temperature it can be seen that there are settings (e.g. 60 % light intensity at approx. 2 kHz modulation frequency) which almost show no temperature dependency and would be suitable for outdoor measurements with big temperature variations.

The device is suitable to work under different ambient light levels as listed in tab. 4.2, however, direct and diffuse sunlight must be avoided. If the ambient light correction circuit improves the capability of suppressing those offsets, however, still has to be tested. A better optic design (using bandpass-filters instead of long-pass filters in front of the photodiode) could also expand the application possibilities, but for the everyday conditions in the laboratories the prototype works good enough.

5.3. New phase fluorometer designs: An outlook

The small size of the scaled-down measurement cells, which are basically a phase fluorometer on their own, opens the door for many applications and it just needs to be enclosed within a slim case and connected to a cable, which connects to the mainboard. Therefore the mainboard would be similarly to a hub where many cells could be plugged in. However, as a standard I2C-bus doesn't really include plug-and-play features a better I2C-protocol would have to be developed with dynamic address allocation for the cells.

Another idea is to make these small cells capable of working stand-alone by including a small battery that provides enough power. The software of one cell can be dramatically extended with data-logging features and higher level commands, such as measurement cycles. The logged data could either be transmitted by wire (I2C-bus, USB) or wireless (Bluetooth, NFC). The advantage of near-field-communication (NFC) would be that no further power would be consumed as part of the communication process and during read-out the battery could be even recharged inductively! This makes a completely proof design of the case possible and make the device appropriate for measurements in really harsh and remote environments.

5.4. Closing words

The presented concepts for a phase fluorometer in this work show that the size of such a device can be dramatically miniaturised, but at the same time the reliability and robustness can be increased. Many more possibilities for increasing the performance came up after interpreting the results of this prototype and are focus for ongoing research. Big open capabilities can be found in the integration of these systems in order to further reduce the amount of analog systems and integrate them in miniaturised mixed-signal devices. This process of miniaturization by simultaneously increasing functionality was seen in the mobile phone market and may be seen in the opto-chemical sensor market as well.

6. Bibliography

[1] R. Narayanaswamy and O. S. Wolfbeis, *Optical sensors: industrial, environmental and diagnostic applications*. Springer, 2004.

[2] I. Klimant, V. Meyer, and M. Kühl, "Fiber-optic oxygen microsensors, a new tool in aquatic biology," *Limonology And Oceanography*, vol. 40, no. 6, pp. 1159–1165, 1995.

[3] D. Papkovsky, "New oxygen sensors and their application to biosensing," *Sensors and Actuators B: Chemical*, vol. 29, pp. 213–218, Oct. 1995.

[4] C. McDonagh, C. Kolle, a.K. McEvoy, D. Dowling, a.a. Cafolla, S. Cullen, and B. MacCraith, "Phase fluorometric dissolved oxygen sensor," *Sensors and Actuators B: Chemical*, vol. 74, pp. 124–130, Apr. 2001.

[5] I. Klimant, M. Kuhl, R. Glud, and G. Holst, "Optical measurement of oxygen and temperature in microscale: strategies and biological applications," *Sensors and Actuators B: Chemical*, vol. 38, pp. 29–37, Jan. 1997.

[6] Z. Chen-Esterlit, S. Peteu, H. Clark, W. McDonald, and R. Kopelman, "A comparative study of optical fluorescent nanosensors ("PEBBLEs") and fiber optic microsensors for oxygen sensing," *Bouvé Faculty Publications*, 1999.

[7] K. Koren, G. Mistlberger, S. M. Borisov, and I. Klimant, "Ferromagnetic and permanent magnetic spheres as platform for single- and dual-analyte optical sensors," *Procedia Engineering*, vol. 5, pp. 997–1000, 2010.

[8] S. M. Borisov, G. Nuss, W. Haas, R. Saf, M. Schmuck, and I. Klimant, "New NIR-emitting complexes of platinum (II) and palladium (II) with fluorinated benzoporphyrins," *Photochemistry and Photobiology*, vol. 201, pp. 128–135, 2009.

[9] W. Trettnak, "Miniaturized luminescence lifetime-based oxygen sensor instrumentation utilizing a phase modulation technique," *Sensors and Actuators B: Chemical*, vol. 36, pp. 506–512, Oct. 1996.

[10] C. Stehning and G. Holst, "DSP-based measuring system for temperaturecompensated fiber optical oxygen sensors," in *Proceedings of SPIE*, vol. 4578, pp. 259–270, Citeseer, 2001.

[11] D. Xiao, Y. Mo, and M. Choi, "A hand-held optical sensor for dissolved oxygen measurement," *Measurement Science and Technology*, vol. 14, pp. 862–867, June 2003.

[12] A. N. Cartwright, V. P. Chodavarapu, S. J. Kim, R. M. Bukowski, A. H. Titus, and F. V. Bright, "CMOS Microsystems for Phase Fluorometric Biochemical Monitoring," *2007 International Symposium on Signals, Systems and Electronics*, pp. 37–40, July 2007.

[13] V. Chodavarapu, D. Shubin, R. Bukowski, A. Titus, A. Cartwright, and F. Bright, "CMOS-based phase fluorometric oxygen sensor system," *Circuits and Systems I: Regular Papers, IEEE Transactions on*, vol. 54, pp. 111–118, Jan. 2007.

[14] B. Valeur, *Molecular Fluorescence: Principles and Applications*. Wiley-VCH Verlag GmbH, 2001.

[15] J. R. Lakowicz, *Principles of Fluorescence Spectroscopy*, vol. 13. Springer, third ed., 2008.

[16] P. Gründler, *Chemische Sensoren: Eine Einführung für Naturwissenschaftler und Ingenieure*. 2004.

[17] S. O. Kasap, *Optoelectronics and Photonics: Principles and Practices*. Prentice Hall, 2001.

[18] W. Kester, *Mixed-Signal and DSP design techniques*. Prentice Hall, 2000.

[19] E. R. Carraway, J. N. Demas, B. a. DeGraff, and J. R. Bacon, "Photophysics and photochemistry of oxygen sensors based on luminescent transition-metal complexes," *Analytical Chemistry*, vol. 63, pp. 337–342, Feb. 1991.

[20] M. Valledor, J. Campo, F. Ferrero, J. Viera, M. Gonzalez, C. Blanco, I. Sanchez-Barragan, J. Costa-Fernandez, and A. Sanz-Medel, "Ratiometric Methods For Optical Fiber Instrumentation Based On Luminescence Sensors," in *Instrumentation and Measurement Technology Conference Proceedings, 2008. IMTC 2008. IEEE*, pp. 1960–1963, IEEE, 2008.

[21] M. Horn and N. Dourdoumas, *Regelungstechnik: rechnerunterstützter Entwurf zeitkontinuierlicher und zeitdiskreter Regelkreise*. Pearson Studium, 2004.

[22] V. Ogurtsov, "Selection of modulation frequency of excitation for luminescence lifetime-based oxygen sensors," *Sensors and Actuators B: Chemical*, vol. 51, pp. 377–381, Aug. 1998.

[23] S. Borisov, G. Nuss, and I. Klimant, "Red light-excitable oxygen sensing materials based on platinum (II) and palladium (II) benzoporphyrins," *Analytical chemistry*, vol. 80, no. 24, pp. 9435–9442, 2008.

[24] U. Tietze and C. Schenk, *Halbleiter-Schaltungstechnik*. Springer, 12 ed., 2002.

[25] "Photodiode Technical Information," tech. rep., Hamamatsu.

[26] J. Williams, "Power Gain Stages for Monolithic Amplifiers," Tech. Rep. March, Linear Technology, 1986.

[27] J. G. Graeme, "Feedback Plots Define OP Amp AC Performance," Tech. Rep. 602, Burr Brown, 1991.

[28] "Photodiode Monitoring With OP Amps," Tech. Rep. 602, BURR-BROWN, 1995.

[29] S. Tilden, "Standard for terminology and test methods for analog-to-digital converters: a case study of utilization of IEEE-STD-1241," *Computer Standards & Interfaces*, vol. 22, pp. 103–112, June 2000.

[30] M. Stitt and W. Meinel, "OPT201 photodiode-amplifier rejects ambient light," Tech. Rep. 602, Burr-Brown, 1993.

[31] J. R. Lakowicz, R. Jayaweera, N. Joshi, and I. Gryczynski, "Correction for contaminant fluorescence in frequency-domain fluorometry.," *Analytical biochemistry*, vol. 160, pp. 471–9, Feb. 1987.

[32] F. Hua and K. Pooi Yuen, "Exact phase noise model and its application to linear minimum variance estimation of frequency and phase of a noisy sinusoid," *2008 IEEE 19th International Symposium on Personal, Indoor and Mobile Radio Communications*, pp. 1–5, Sept. 2008.

[33] V. Kuhlmann, A. Sinton, M. Dewe, and C. Arnold, "Effects of Sampling Rate and ADC Width on the Accuracy of Amplitude and Phase Measurements in Power-Quality Monitoring," *IEEE Transactions on Power Delivery*, vol. 22, pp. 758–764, Apr. 2007.

[34] M. Wagdy and S. Awad, "Effect of sampling jitter on some sine wave measurements," *IEEE Transactions on Instrumentation and Measurement*, vol. 39, no. 1, pp. 86–89, 1990.

[35] K. Schiller and F. W. Müller, "Singlet oxygen lifetime in polymer films," *Polymer International*, vol. 25, no. 1, pp. 19–22, 1991.

[36] O. Kohls and T. Scheper, "Setup of a fiber optical oxygen multisensor-system and its applications in biotechnology," *Sensors And Actuators*, 2000.

[37] D. R. Brandrup, J.; Immergut, Edmund H.; Grulke, Eric A.; Abe, Akihiro; Bloch, *The polymer handbook*. 1999.

A. List of Figures

B. List of Tables

C. Simulation parameters

Light source

Table C.1.: LED and light fibre parameters

◦ light fibre focusing diameter[1]	$D_f = 100\,\mu\text{m}$
◦ light intensity ratio coupling into the fibre and exciting the luminophore	$r_c = 1/10$
◦ peak wavelength of LED	$\lambda_{LED} = 622\,\text{nm}$
◦ reference current of LED	$I_0 = 50\,\text{mA}$
◦ luminous intensity[2] at I_0	$\Phi_0 = 6\,\text{lm}$

[1] estimated
[2] corrected with the relative spectral responsivity of the human eye defined by the CIE (Commission Internationale de l'Éclairage)

Luminophores

Table C.2.: PtTPTBPF parameters

◦ quantum yield[1]	$\Phi_P = 0.6$
◦ excitation wavelength[1]	$\lambda_{ex} = 615\,\text{nm}$
◦ extinction coefficient[1]	$\varepsilon = 146,000\,\text{l} \cdot \text{M}^{-1}\text{cm}^{-1}$
◦ T_1 lifetime[2]	$\tau_0 = 59\,\mu\text{s}$
◦ molar mass	$m_m = 1,080\,\text{g/mol}$
◦ rate constant for internal conversion[3]	$k_{ic} = 1 \cdot 10^9\,\text{s}^{-1}$

[1] taken from [8]
[2] determined from the measurement results at low light intensities
[3] estimated

Table C.3.: PdTPTBPF parameters

◦ quantum yield[1]	$\Phi_P = 0.23$
◦ excitation wavelength[1]	$\lambda_{ex} = 629\,\text{nm}$
◦ extinction coefficient[1]	$\varepsilon = 115,000\,\text{l} \cdot \text{M}^{-1} \cdot \text{cm}^{-1}$
◦ T_1 lifetime[2]	$\tau_0 = 319\,\mu\text{s}$
◦ molar mass	$m_m = 991\,\text{g/mol}$
◦ rate constant for internal conversion[3]	$K_{ic} = 1 \cdot 10^9\,\text{s}^{-1}$

[1] taken from [8]
[2] determined from the measurement results at low light intensities
[3] estimated

Polymer

Table C.4.: PVC with softeners parameters

◦ immobilised luminophore concentration	$c_{dye} = 0.83\,\%$
◦ percent of softeners	$p_{soft} = 20\,\%$
◦ density[1]	$\rho_{PVC} = 1,300\,\mathrm{g/l}$
◦ solubility for oxygen[1]	$\alpha_{PVC} = 0.29 \cdot 10^{-6}\,\mathrm{Pa}^{-1}$
◦ quenching constant for PtTPTBPF[2]	$K_D^{Pt} = 0.069\,\mathrm{kPa}^{-1}$
◦ quenching constant for PdTPTBPF[2]	$K_D^{Pd} = 0.174\,\mathrm{kPa}^{-1}$

[1] taken from [37]
[2] determined from the measurement results at low light intensities

D. Communication Protocol

The communication interface for the prototype was developed in co-operation with *Pyro Science*, thus the prototype can be seamlessly integrated with the PC-software for the commercial product Fiber-Optic Oxygen Meter (Firesting O_2). All commands can be processed by the mainboard of the prototype and passes on commands for the individual cells on the I2C-bus.

Firesting Protocol 2.13

06.04.2011

Serial Port Settings

19200 baud, 8 data bit, 1 stop bit, no parity, no handshake

General Definitions

ABC The characters of the commands (bold characters) are sent in ASCII code. The first parameter can follow immediately, or can be separated by any number of spaces.

X (italic letter) represent signed integer parameter written as a decimal ASCII-String. Several parameters are separated by one or more spaces.

<CR> corresponds to ASCII code 13 (hexadecimal: 0x0D).

Level 0 Commands (measurement electronics)

Level 0 commands always consist of 3 letters followed by the addressed channel number *C*. The total command length must not be longer than 32 characters, whereby the length of the answer is principally not limited (e.g. for command RMR).

CONFIDENTIAL

Read firmware version

Command: **VER** *C* <CR>
Answer: **VER** *C R* <CR>

Returns firmware revision *R*. For example *R*=231 designates firmware revision 2.31

Read Register

Command: **REA** *C T R* <CR>
Answer: **REA** *C T R Y* <CR>

Returns the value *Y* (signed integer) from the register number *R* belonging to the register type *T*.

Read Multiple Registers

Command: **RMR** *C T R N* <CR>
Answer: **RMR** *C T R N* $Y_1 \ldots Y_n$ <CR>

Returns the values $Y_1 \ldots Y_n$ (signed integer) from *N* consecutive registers starting from register number *R* belonging to the register type *T*.

Write Register

Command: **WRT** *C T R Y* <CR>
Answer: **WRT** *C T R Y* <CR>

Writes the value *Y* (signed integer) to the register number *R* belonging to the register type *T*.

Save Register Settings Permanently

Command: **SVS** *C* <CR>
Answer: **SVS** *C* <CR>

Saves the registers of type 0,1, and 99 into the internal flash memory, ensuring that the register values are kept when the power is cycled. However, registers of type 99 (system registers) are only saved, if the magic number was written to SYS_MAGIC_NUMBER. Remark for Firesting O2: The flash hardware is officially specified for max. 10000 flash cycles, so this command should not be used too often.

Measure Temperature

Command: **TMP** *C* <CR>
Answer: **TMP** *C* <CR>

Initiates a temperature measurement. Both the externally connected temperature sensor (PT100) as well as the internal chip temperature of the microcontroller are measured. The results are stored in the

corresponding "result" registers. The user can access the results then by reading the result registers (commands REA or RMR).

Measure Oxygen

Command: **MSR** *C* <CR>
Answer: **MSR** *C* <CR>

Intitiates a complete oxygen measurement. The measurement consist of a measurement with the main LED with a duration of SET_PERIOD / 2, followed by a measurement with the reference LED with duration SET_PERIOD / 2. The total measurement time is SET_PERIOD. The other measurement parameters are defined by the corresponding "settings" registers. The resulting raw data of the measurement are stored in the "raw data" registers. Then, based on the settings in the "calibration" registers the oxygen values are automatically calculated and stored in the corresponding "result" registers. The user can access the results then by reading the "result" registers (commands REA or RMR).

Measure only with Main LED (advanced command!)

Command: **SMA** *C* <CR>
Answer: **SMA** *C* <CR>

Corresponds mostly to the MSR command. The only difference is, that the reference LED is **not** measured. Therefore, the total measurement time is only SET_PERIOD / 2. For the calculation of the oxygen values the last measurement of the reference LED stored in the "raw data" registers is used. The user has to ensure that the reference and the main LED measurements are performed with the same parameters.

Measure only with Reference LED (advanced command!)

Command: **SRF** *C* <CR>
Answer: **SRF** *C* <CR>

Corresponds mostly to the MSR command. The only difference is, that the main LED is **not** measured. Therefore, the total measurement time is only SET_PERIOD / 2. For the calculation of the oxygen values the last measurement of the main LED stored in the "raw data" registers is used. The user has to ensure that the reference and the main LED measurements are performed with the same parameters.

Recalculate Oxygen Values (advanced command!)

Command: **RCO** *C* <CR>
Answer: **RCO** *C* <CR>

Based on the values in the "raw data" registers and the "calibration" registers, this command recalculates the values in the "result" registers. This command might be for example useful for implementing filter functions on the raw data by the external application software. E.g. the absolute phase measured with the reference LED (RAW_REF_PHI) could be amended with a strong running average. The proceeding would be as follows: (1) measure oxygen with command MSR, (2) read out RAW_REF_PHI and calculate running, (3) average by external application software, (4) write the averaged value back to RAW_REF_PHI, (5) recalculate oxygen values with the command RCO.

Calibrate Sensor at 0% Air Saturation

Command: **CLO** *C R P* <CR>
Answer: **CLO** *C R P* <CR>
Initiates a calibration sequence of repeated oxygen measurements (as for command MSR described). *R* (01..255) designates the repitition number. *P* defines the resting time inbetween the single oxygen measurments in multiples of 100ms (00..255 corresponding to 0..25.5 sec.). The 0% calibration data are calculated as the average from the consecutive measurements, and stored in the "calibration" registers.

Calibrate Sensor at 100% Air Saturation

Command: **CHI** *C R P* <CR>
Answer: **CHI** *C R P* <CR>

Performs calibration at 100% air saturation corresponding to the command CLO.

Level 0 Registers

Settings (register type 0) all signed integer 32bit

reg#	Name	Description	Definition	Range	Default
0	SET_TEMP *	actual temperature	T [°C] x 1000		20000
1	SET_PRESSURE	actual air press.	P [mbar]		1013
2	SET_SALINITY	actual salinity	S [g/l] x 1000		0
3	SET_PERIOD	total oxygen measuring time	t [ms]	1..20000	200
4	SET_LED_INT	LED intensity level (7 = max.)	0=min. 7=max.	0 - 7	2
5	SET_PD_AMP	PD amplification level (7 = max.)	0=min. 7=max.	0 - 7	6
6	SET_TEMP_PERIOD	temperature measuring time	t [ms]	1..20000	100
7	SET_FIBER_TYPE	specifies fiber type	0 = 200µm fiber 1 = 400µm fiber 2 = 1mm fiber		0

* if SET_TEMP is set to -300000 (=-300C), then RSL_EXT_TEMP is used instead for temperature compensation when the results registers are calculated. If then also RSL_EXT_TEMP = -300000 (i.e. no sensor detected), then CAL_TEMP is used for temperature compensation.

Calibration (register type 1) all signed integer 32bit

reg#	Name	Description	Definition	Range	Default
0	CAL_DPHI0	dphi at 0% air sat.	dphi[°] x 1000	0-90000	52000
1	CAL_DPHI100	dphi at 100% air sat.	dphi[°] x 1000	0-90000	20000
2	CAL_TEMP	calibration temp.	T [°C] x 1000		20000
3	CAL_PRESSURE	calibration air press.	P [mbar]		1013
4	CAL_HUMIDITY	calibration rel. humidity	H[%]		50
5	CAL_F_VALUE	f-value	f x 1000	1 - 1000	950
6	CAL_M_VALUE	m-value	m x 1000	1 - 1000	100
7	CAL_FREQ	frequency	F [Hz]		4000
8	CAL_DTAU0DT	tt= dtau0/dT	tt [s K^{-1}] x 10^{10}		-150
9	CAL_DKSVDT	kt= dKsv/dT	kt[$mbar^{-1}K^{-1}$] x 10^{6}		120

Raw Data (register type 2) all signed integer 32bit

reg#	Name	Description	Definition	Range
0	RAW_MAIN_AMPLITUDE	Amplitude for main LED (peak2peak = 2*AC)	Amp[mV] x 1000	
1	RAW_MAIN_BKGND	Background for main LED (= DC - AC)	Bkgnd[mV] x 1000	
2	RAW_MAIN_PHI	phi of main LED	phi[°] x 1000	
3	RAW_REF_AMPLITUDE	Amplitude for ref. LED (peak2peak = 2*AC)	Amp[mV] x 1000	
4	RAW_REF_BKGND	Background for ref. LED (= DC - AC)	Bkgnd[mV] x 1000	
5	RAW_REF_PHI	phi of ref. LED	phi[°] x 1000	

Results (register type 3) all signed integer 32bit

reg#	Name	Description	Definition	Range
0	RSL_STATUS	bit0=1: measurement in progress bit1=1: sensor signal too low bit2=1: sensor signal or background light too high bit3=1: reference signal too low bit4=1: reference signal too high bit5=1: no external temperature sensor detected bit6 : init flag (=0 after power up, can be set by the user to 1 as a control flag in order to detect power cycling)		
1	RSL_DPHI	dphi	dphi[°] x 1000	
2	RSL_UMOLAR	oxygen in µmol/l	oxy[µmol/l] x 1000	
3	RSL_MBAR	oxygen in mbar	oxy[mbar] x 1000	
4	RSL_ASAT	oxygen in %air sat.	oxy[%air sat.] x 1000	
5	RSL_EXT_TEMP	external temperatur from PT100 (no sensor detected = -300000)	T [°C] x 1000	
6	RSL_INT_TEMP	internal chip temperature	T [°C] x 1000	
7	RSL_SIGNAL_INTENSITY	identical to RAW_MAIN_AMPLITUDE	Intensity[mV] x 1000	
8	RSL_AMBIENT_LIGHT	ambient light measured with all LEDs off	AmbLight[mV]x1000	

Level 1 Commands (communication electronics)

Level 1 commands always consist of 5 characters, whereby the 1st character is always "#", i.e. ASCII code 43 (hexadecimal 0x23).

Read Firmware version

Command: **#VERS** <CR>
Answer: **#VERS** *D N R* <CR>

Returns firmware revision= *R* / 100 of the level 1 microcontroller. For example *R*=231 designates firmware revision *R*= 2.31. *D* denotes the device ID number (Firesting O2: *D*=0, Firepad: *D*=1). *N* indicates the available number of channels (level 0).

Flash Logo

Command: **#LOGO** <CR>
Answer: **#LOGO** <CR>

Flashes the „Firesting O2“-Logo on the Firesting-Device 10 times. The answer is sent after the flashing is finished (duration about 1-2 sec.). During the flashing no measurements should be performed.

Power Down Measurement Electronics

Command: **#PDWN** <CR>
Answer: **#PDWN** <CR>

Enter sleep mode. Powers down the measurement electronics (level 0). Therefore, level 0 commands are disabled! Level 1 is still enabled.

Power Up Measurement Electronics

Command: **#PWUP** <CR>
Answer: **#PWUP** <CR>

Wake up from sleep mode. Powers up the measurement electronics (level 0). Enables level 0 commands.

Enter Deep Sleep Mode

Command: **#STOP** <CR>
Answer: **#STOP** <CR>

Powers down the measurement electronics (level 0) and sets the communication electronics (level 1) into a power-saving deep sleep mode. The device is waked up again by sending a single byte (any value) to the USB/UART-interface. This single byte is lost and will not be interpreted as a command.

Set Baud Rate

Command: **#BAUD** *R*<CR>
Answer: **#BAUD** *R*<CR>

Changes the baud rate to *R* baud (allowed range 1200 - 115200). The answer is sent with the old baud rate. This setting is only valid until the next power cylcling or until the next #STOP command. The default baud rate after power up is always 19200 baud.

Internal I2C protocol

Communication between the host controller and measurement cells via I2C with a clock frequency of 100kHz. All level0 commands are passed on to the measurement cell with channel number **C#**, the channel number defines the I2C-address:

I2C-address = (C#+4) x 2
(e.g. C = 1, I2C-address = 0x0A)

Maximum number of allowed channels: 64 => I2C-address: 0x88
A device that is not yet defined to a specific channel is configured with channel number 65 (I2C-address 0x8A). This allows the user to gradually extend a firepad and specify one-by-one cell with its channel number.

E.g. you have a 4-channel firepad and want to replace channel 3:

- Define channel 3 with channel number 65 by changing the I2C-address in the system register to 0x8A
- Save this settings permanently
- Remove this channel from the firepad
- Insert a new measurement channel into the firepad
- Look for the new measurement channel (e.g. VER 65 <CR>), it should respond
- Redefine this channel to be channel number 3 (change I2C-address to 0x0E).
- Save the settings permanently

I2C protocol frame:

S – start condition
P – stop condition
A – address (8bit) plus read/write bit (e.g. 0x0A => write to C#1, 0x0B => read from C#1)
D – data (8bit) sent by host
D – data (8bit) sent by cell

S A D D D ... P (writing)
S A D D D ... P (reading)

All level0 commands received are transferred into the data section of the protocol as following:

- The first 3 characters are replaced by a single byte encoding the command, starting with 0x01 (VER) and ending with 0x0C (CHI)
- Channel number is removed from the command as it is translated into the i2c-address (e.g. in write mode 0x0A and read mode 0x0B)
- All parameters except Y are translated into one data bytes in the same order as they appear in the received string
- Y parameters are translated into 4 data bytes as they can hold values of 32bit integers and are represented in little-endian byte order, which means the least significant byte is transmitted first.

E.g. the command **RMR 1 1 0 2 <CR>**
Would be translated as **S 0x0A 0x03 0x01 0x00 0x04 P**

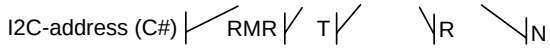

The answer is fetched by sending the i2c-address with the read bit set (e.g. 0x0B). For the following request would be the values of the calibration register at register number 0 (52000 = 0x0000CB20) and register number 1 (20000 = 0x00004E20).

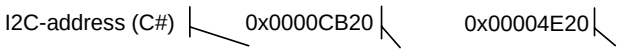

Looks like this: **S 0x0B 0x20 0xCB 0x00 0x00 0x20 0x4E 0x00 0x00 P**
And translated as **RMR 1 1 0 2 52000 20000 <CR>**

So the measurement cell just sends the answer to the last request, which the host collects and fills up the answer string with it.